RUPRECHT-KARLS-UNIVERSITÄT HEIDELBERG

Jens Appmeier

Immersed Quantum Systems: A Sodium Bose-Einstein Condensate for Polaron Studies

Dissertation

HD-KIP-10-24

KIRCHHOFF-INSTITUT FÜR PHYSIK

Dissertation
submitted to the
Combined Faculties for the Natural Sciences and for Mathematics
of the Ruperto-Carola University of Heidelberg, Germany
for the degree of
Doctor of Natural Sciences

Put forward by

Diplom-Physiker: Jens Appmeier
Born in: Leipzig, Germany

Oral examination: Juli 13, 2010

Immersed Quantum Systems: A Sodium Bose-Einstein Condensate for Polaron Studies

Referees: Prof. Dr. Markus K. Oberthaler
Prof. Dr. Selim Jochim

Zusammenfassung

In der vorliegenden Arbeit wird der Aufbau eines neuen Experiments zur Untersuchung ultrakalter bosonischer und fermionischer Quantengase beschrieben. Bose-Einstein Kondensation von ^{23}Na Atomen wird in zwei verschiedenen Magnetfallenkonfigurationen, der „plugged“ Quadrupolfalle und der Kleeblattfalle erreicht. Außerdem werden beide Fallentypen bezüglich ihrer Eignung für Gemischexperimente mit ^{23}Na und ^{6}Li verglichen. In einem solchen Gemisch sollte es möglich sein Polaronen zu untersuchen. Diese Quasiteilchen entstehen, sobald eine Komponente des Natrium-Lithium Gemisches nur noch in einer sehr geringen Konzentration vorliegt. Der Grenzfall eines einzelnen Teilchens in einem bosonischen Hintergrund wird theoretisch betrachtet und anhand einer numerischen Simulation untersucht.

Abstract

The subject of this work is the setup of an experiment to study immersed quantum systems using bosonic ^{23}Na and fermionic ^{6}Li. Bose-Einstein condensation of ^{23}Na has been achieved in two different magnetic trap configurations, namely the plugged quadrupole trap and the cloverleaf trap. Both are compared with respect to their suitability for a two-species experiment using this particular isotopes. In such a mixture, it should be possible to investigate polarons, which are quasiparticles, emerging when one of components of the mixture has only a very rare concentration. Furthermore, a theoretical study of the polaron will be discussed. A mean-field calculation has been carried out in order to simulate the impurity behavior in the presence of a large bosonic background gas.

Contents

1. Introduction **11**

I. BEC Impurity as a Polaron 15

2. Theory of Ultracold Atomic Gases **17**
2.1. BEC: Weakly Interacting Case 17
2.1.1. Basic Scattering Theory 17
2.1.2. Tuning Interactions: Feshbach Resonances 19
2.1.3. Mean-Field Approximation: Gross-Pitaevskii-Equation 21
2.1.4. Excitations of the Interacting BEC: Bogoliubov Transformation 23
2.2. Degenerate Fermions 24
2.3. Polaron Problem 25
2.3.1. Condensed Matter Treatment 26
2.3.2. Cold Atomic Gases Perspective 29

3. Numerical Methods **31**
3.1. Two-Component GPE 31
3.2. Effective Mass Determination 34
3.3. Validity Considerations 36

4. Mean Field Simulation: 2 Component GPE **37**
4.1. Single Impurity in a BEC Background 37
4.1.1. Impurity Localization 37
4.1.2. Density Plots 38
4.1.3. The Coupling Parameter 41
4.1.4. Central Density 43
4.1.5. Influence of the Impurity Potential 44
4.1.6. Effective Mass Computation 45
4.1.7. Which is the Better Impurity: Na or Li? 47
4.2. Many Impurity Case 48

II. Bose-Einstein Condensation of Sodium **51**

5. Trapping and Investigation of Cold, Neutral Atoms **53**
5.1. Optical Dipole Traps . . . 53
5.2. Magnetic Trapping . . . 54
5.2.1. Plugged Quadrupole Trap . . . 56
5.2.2. Cloverleaf Trap . . . 58
5.2.3. Special Requirements in a Two Species Design . . . 61
5.3. Imaging . . . 63
5.4. Deducing the Temperature . . . 65

6. Experimental Setup **67**
6.1. Vacuum System . . . 67
6.2. Sodium Laser System . . . 70
6.3. Magneto-Optical Trap . . . 72
6.4. Spin Polarizing and Purification . . . 74
6.5. BEC in the Plugged Quadrupole Trap . . . 77
6.6. NaLi Unplugged: BEC in Cloverleaf Trap . . . 77
6.7. Dipole Trap . . . 80

7. Conclusion and Outlook **85**

A. Sodium and Lithium Line Data **89**

B. Cloverleaf Design **93**

C. Interlock **97**
C.1. Service Water Circuit . . . 97
C.2. Clean Water Circuit . . . 99

Bibliography **108**

1. Introduction

> Theorie und Experiment
> gehören zusammen, eines ohne
> das andere bleibt unfruchtbar.
>
> *(Max Planck)*

The development of quantum mechanics in 1925 released a great discourse how these new ideas of describing the physics at very small scales modifies our understanding of nature. The outcome of an experiment is open to different interpretations, which is in contradiction to the ideas of the classical understanding of physics. Several interpretations have been developed to gain information about "what's going on there...", the most popular of which is the Copenhagen interpretation, formulated by N. Bohr and W. Heisenberg. Its key feature is the probabilistic interpretation of the wavefunction, describing the state of a particle. A measurement of the state of the particle, for instance its position, causes the wavefunction to collapse to the value of this observable defined by the measurement itself. The question about the position of the particle before the measurement is thus meaningless.

This interpretation of the wavefunction – being the probability amplitudes of the particle – puts aside the discussion about the nature of light and matter, dating back to the 1600s to the competing theories of light by C. Huygens and I. Newton. With the Copenhagen interpretation at hand, the wave-particle duality is a central concept of quantum mechanics. Light and matter can both be described as particles or waves. Young's double-slit experiment has been performed for both matter and light successfully.

The success of quantum mechanics started a new era in physics, leading to a deeper understanding of nature. New phases of matter, apart from solids, fluids and gases were predicted, namely the Bose-Einstein condensate and the degenerate Fermi gas. Each of these are specific to the two fundamental classes of particles, bosons and fermions. The distinction between both becomes important only on the quantum scale, i.e. when the gas of particles can no longer be described by the classical Maxwell-Boltzmann distribution. The reason for this deviation from the classical picture is that the finiteness of the available, discrete energy states of the particles becomes important – quantum mechanics comes into play.

Prominent examples of those two quantum phases is the Bose-Einstein condensation of Cooper pairs, responsible for type I superconductivity or the conduction electrons in solids that are already degenerate at room temperature. But these states also occur at large scale, for instance the neutron stars are thought to consist mostly of

Fermi-degenerate neutrons.

The availability of these states of matter in dilute, cold atomic gases since the mid 1990s [1, 2], triggered a whole range of experiments, addressing fundamental physical questions, which were not accessible in experiments before.

The reason for the success of the cold atomic gases experiments is, that they offer very clean systems[1] with a wide experimental control over the systems parameters like atom number, density, temperature and trapping geometry. Furthermore the scattering properties of the atoms can be manipulated via the use of Feshbach resonances, a degree of freedom that is not accessible in other systems, e.g. solids. This freedom of tuning parameters allows to study a wide range of physical questions, e.g. some condensed matter phenomena with an extended range of tunable parameters, one of which is the polaron problem, addressed in this thesis.

Some achievements of cold atoms gases are the first experimental studies of quantum effects like matterwave interference [3] or the tunneling processes [4] on a macroscopic scale. Using optical lattices in the experiments, has lead to the observation of the superfluid to Mott-insulator transition [5], which can not be studied in solids. This phase transition is not driven by temperature as a classical phase transition, but rather by quantum fluctuations, which still occur at $T = 0$.

Also degenerate Fermi gases have been studied extensively, revealing the transition from the Bardeen-Cooper-Schrieffer (BCS) state of Cooper pairs to the formation of compound molecules [6] and their Bose-Einstein condensation [7, 8, 9]. Feshbach resonances that allow to tune the interaction, have been found in single component Bose gases [10] and in mixtures of two different species [11, 12]. Effects of fermionic atoms on bosonic atoms in a 3D optical lattice have been studied [13, 14]. Experiments succeeded to involve different spin states of an ultracold atom gas as an additional free parameter of the system [15].

The aim of the experiment presented here is to study immersed quantum systems, where a species with a small concentration (impurities) is interacting with a degenerate background gas. A similar system is known from condensed matter physics. If an electron in the conduction band is moving through the ionic crystal lattice it can interact with the lattice excitations (phonons), thereby forming a quasiparticle—the polaron.

In the crystal lattice, the electron-phonon interaction mediates a weak coupling between electrons near the Fermi edge. Cooper showed that even an arbitrarily weak attractive interaction in these systems will lead to the occurrence of weakly bound pairs (the Cooper-pairs), responsible for type I superconductivity [16].

However, type II superconductors are not explained by the BCS theory. Here the critical temperature for superconductivity is close to the Debye temperature T_{D}. Even at these temperatures, the electron-phonon interaction should still be large enough, such that every electron forms a polaron. In this limit the polaron-polaron inter-

[1] The techniques used to achieve Bose-Einstein condensation of dilute atomic gases are highly isotope selective, such that any kind of depletion of the system with a different species or isotope requires a high experimental effort. This is in contradiction to condensed matter systems where a very high effort is necessary to produce samples with a negligible concentration of dopants.

action needs to be taken into account. If this interaction appears to be attractive, the Coulomb potential of both electrons forming the polarons is screened and a two-polaron pair occurs—the bipolaron. This quasi-particle is of bosonic nature and their superfluidity can explain type II superconductivity [17]. However up to now this process is neither fully understood nor confirmed by experiments due to the lack of materials showing a strong electron-phonon coupling.

As already mentioned, we intent to study immersed systems using ultracold atomic systems, providing the possibility to tune the interaction between background and impurity atoms. We plan to immerse fermionic ^{6}Li atoms into a bosonic background gas of ^{23}Na atoms. The concentration of the impurities should be low enough to ensure that the background gas completely determines the thermodynamic properties of the system. As this system is cooled into quantum degeneracy, the impurity atoms can interact with a coherent background gas, revealing its own dispersion relation. This system can be mapped onto the Fröhlich Hamiltonian [18], describing the behavior of an electron in the presence of an ionic crystal lattice that forms a polaron.

In our system the impurity atom corresponds to the electron. The interaction of the impurity atoms with the Bogoliubov modes of the background BEC is similar to the electron's interaction with the phononic lattice excitations of the crystal. Both give rise to a dispersion relation. The dispersion relation of the crystal lattice consists of an optical and an acoustical part, the latter being similar to the Bogoliubov spectrum of a BEC at low excitation momenta.

We plan to map out this analogy using an ultracold gas experiment and aim to be able to study the strong coupling limit of the polarons, where the strong electron phonon interaction in the condensed matter case localizes the polaron to a single lattice ion. A regime so far not accessible in experiments.

Contents of this Thesis

In the first part of this thesis, the polaron problem described above will be discussed in the context of ultracold atomic gases. Chapter 2 will recall the necessary theoretical framework of the ultracold gases and discuss a many-body approach to the problem of a single impurity atom immersed in a background BEC. These results will be compared to a mean-field simulation of the immersed impurity in chapter 4. The numerical methods of this calculation will be explained in chapter 3.

In the second part of this thesis, the experimental setup build to study degenerate Bose and Fermi gases will be explained. Chapter 5 discusses the concepts used to cool atomic samples into the nK regime and how information of the ultracold atomic system is extracted. In chapter 6, the status of the setup will be presented and the cooling steps that lead to the Bose-Einstein condensate of ^{23}Na in a plugged quadrupole trap and a cloverleaf trap configuration will be explained.

Part I.

BEC Impurity as a Polaron

The first part of this thesis deals with the theoretical background of ultracold atom experiments and an introduction to the polaron problem. The aim of the experiment is to study polaronic systems. In such systems one deals with a large background component – here a Bose-Einstein condensate of sodium atoms – and some well controlled impurities. Such a system has its counterparts in condensed matter physics, where the behavior of polarons – electrons moving through an ionic crystal lattice thereby interacting with the lattice phonons – is of special interest.
A mean-field study of the polaron problem from the ultracold atom perspective is presented and the results are compared to a condensed matter approach of the problem.

2. Theory of Ultracold Atomic Gases

In this chapter, a short introduction to the relevant theory parts of ultracold samples shall be presented. This chapter is not meant to provide a complete introduction into the field. This can be found in a variety of very good review articles e.g. [19, 20, 21] for bosons and [22, 23] for fermions. Instead the most relevant quantities shall be recalled. The first section starts with an overview of weakly interacting Bose-Einstein condensates and the scattering properties of atomic samples at low temperatures. After that the Gross-Pitaevskii equation (GPE) will be introduced, as well as the Thomas-Fermi approximation. After a short excursion to Bogoliubov theory some remarks concerning fermions will be made. The last section will concentrate on the link between ultracold atomic samples and the polaron problem in condensed matter.

2.1. BEC: Weakly Interacting Case

The non-interacting BEC is a standard textbook problem and can be found for instance in [24, 25]. However when studying atomic gases in experiments, the atoms do interact with a finite scattering length a typically ranging from a few Bohr radii $a_0 = 0.05$nm to a few nm. Some examples are ^{87}Rb with a scattering length of $100a_0$ or ^{23}Na with $63a_0$ are repulsively interacting. Examples for attractive interacting species are ^{85}Rb with $-443a_0$ or ^{7}Li with $-25a_0$. These scattering lengths are all in the low energy limit and the reason why the higher order collisions can be neglected will be presented in the following.

2.1.1. Basic Scattering Theory

When considering the elastic collision of two low energy particles the asymptotic solution to the following Schrödinger equation needs to be found [26]:

$$\left(-\frac{\hbar^2}{2m_\mathrm{r}}\nabla^2 + V(r) - E\right)\psi(r) = 0 \tag{2.1}$$

Here m_r denotes the reduced mass, r the center of mass coordinate, k the wavevector of the relative motion and $E = \hbar^2k^2/2m_\mathrm{r}$ the relative kinetic energy. For distances much larger than the interparticle spacing the solution to this problem can be written as a plain wave (undisturbed part) and a spherical wave (from the scattering event):

$$\psi(r) = e^{ikz} + f(\theta)\frac{e^{ikr}}{r} \tag{2.2}$$

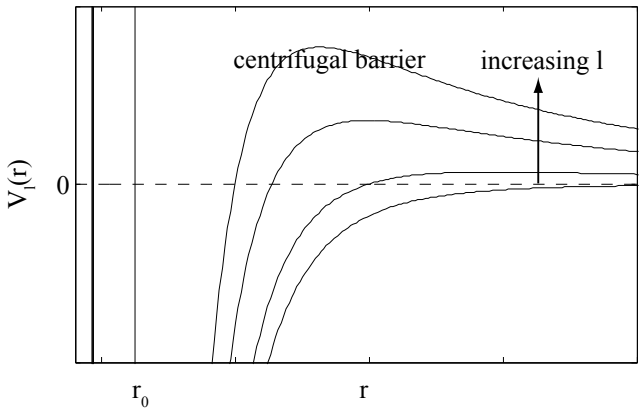

Figure 2.1.: *Atomic potential including the centrifugal barrier for increasing l. For low energy collisions only the $l = 0$ potential is of relevance since two colliding atoms do not have enough energy to overcome the centrifugal barrier.*

The term $f(\theta)$ is refered to as scattering amplitude and is related to the differential cross-section by $d\sigma/d\omega = |f(\theta)|^2$. Due to the cylindrical symmetry of the problem the equations may be expanded in terms of Legendre polynomials $P_l(\cos\theta)$. The potential and the wave function in this description read:

$$V_l(r) \quad = V(r) + \tfrac{\hbar^2 l(l+1)}{2m_r r^2} \tag{2.3}$$

$$\psi(r) \quad = \sum_{l=0}^{\infty} P_l(\cos\theta) R_{kl}(r) \tag{2.4}$$

where the last term of the potential denotes the centrifugal barrier –see fig. 2.1 – and the R_{kl} satisfy the radial Schrödinger equation. For ultracold temperatures of the atomic samples, we are dealing with in the lab, only the $l = 0$ term is of relevance. This is due to the fact that the particles do not have enough energy to overcome the centrifugal barrier in the $l > 0$ states such that these do not contribute to the scattering amplitude. At very large distances the radial solution of the Schrödinger equation may be written as

$$R_{kl}(r) \overset{r\to\infty}{\sim} \sin(kr - l\frac{\pi}{2} + \delta_l) \tag{2.5}$$

thereby introducing the phase shift δ_l between the incoming and the outgoing wave. In the case of $V(r) = 0$, i.e. for no interaction the phase shift of the scattered wave δ_l is equal to zero and the incoming and outgoing waves are equal. The whole effect of the scattering potential is described by that phase shift. For collisions at ultracold temperatures, i.e. low momenta $k \ll 1/r_0$, where r_0 resembles the range of the scattering potential it is useful to define the scattering lengths a_l as follows:

$$a_l(k) = \frac{-\tan\delta_l}{k}. \tag{2.6}$$

Using the radial Schrödinger equation, one can show that the phase shifts of the scattered wave for low momenta are proportional to k^{2l+1}. In the limit of $k \to 0$, the $l = 0$ term dominates and the whole scattering process is characterized by the s-wave scattering length $a_\mathrm{s} \equiv a_{l=0}$.

In this limit the elastic cross section takes the simple form:

$$\sigma(k) = \frac{4\pi a^2}{1 + a^2k^2}. \tag{2.7}$$

Up to now the discussion was about classical particles only. When dealing with indistinguishable particles however, the situation changes. The cross section for bosonic atoms includes another factor of 2 since a direct scattering leads to the same result as an momentum exchange scattering of two atoms. Therefore both contributions have to be added. For fermions however the same argument is true, but only scattering amplitudes with odd l are allowed for symmetry reasons.[1] As the energy of the atomic sample is decreased higher order collisions die out since the atoms cannot overcome the centrifugal barrier anymore. If the energy is low enough such that even the $l = 1$ (p-wave) contributions can be neglected, the scattering cross section for two identical fermions vanishes.

2.1.2. Tuning Interactions: Feshbach Resonances

Although we are dealing with s-wave scattering only, the elastic cross section of the atoms can be varied over a wide range and therewith changing the scattering properties of the ultracold sample. For instance the cross section (2.7) can take values from $\sigma = 4\pi a^2$ in the limit $ka \ll 1$ up to the so-called unitarity value of $\sigma = 4\pi/k^2$ in the limit $ka \gg 1$. In order to reach those regimes one needs a handle on the scattering length a which is provided by Feshbach resonances [27]. This powerful tool allowed for many nice experiments from their discovery [28, 10] in 1998. As an example in sodium or lithium systems, molecule formation of ^{6}Li [29, 30, 31], ^{23}Na [32] or interspecies resonances like ^{6}Li–^{23}Na [11] have been observed.

The basic idea of a Feshbach resonance is a coupling between two states in different potential curves of the colliding atoms, as shown in fig. 2.2. They enter in an unbound state with energy E above the dissociation energy (open channel). If the next bound state in this potential is slightly below the dissociation energy, the interaction will be repulsive ($a > 0$). In the opposite case where the next bound state of the open channel potential would be just above the threshold, the interaction will be attractive ($a < 0$). But also a second potential (closed channel) providing a bound state in close proximity to the dissociation energy of the open channel may exist. If those two energy states in both channels are close to degeneracy, even a small coupling between the states

[1] for bosons all the even l contributions add up, but in this context we only deal with $l = 0$

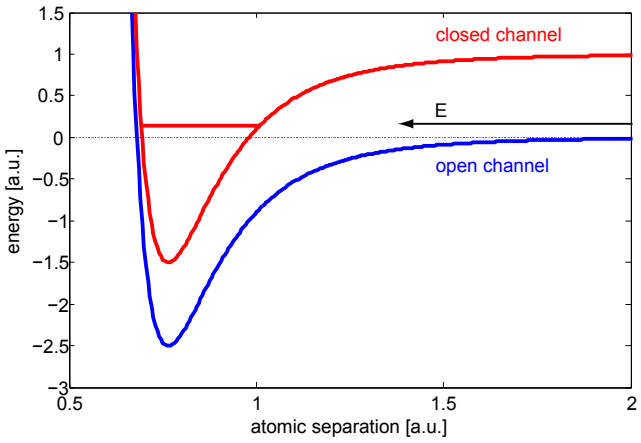

Figure 2.2.: *simple two-channel model of a Feshbach resonance. Open (closed) channel refer to the two incoming atoms to be in a unbound (bound) state of the potential. If the bound state of the closed channel is tuned into degeneracy with the atoms in the incoming open channel a scattering resonance occurs that changes the scattering properties of the incoming atoms.*

will give rise to a strong mixing of the open and closed channels. Again, depending of the location of the closed channel bound state with respect to the open channel dissociation energy the incoming atoms in the open channel will interact repulsively or attractively.

If the magnetic moments of the atoms in the open and closed channel are different, the corresponding potentials can be tuned with respect to each other using an external magnetic field. This tuning shifts the closed channel potential with respect to the open channel potential, thus varying the location of the bound state. The scattering length of the colliding atoms will change from attractive ($a < 0$) to repulsive ($a > 0$) as the closed channel bound state is tuned from slightly above the dissociation energy of the open channel to slightly below it. In the intermediate regime (i.e. the quasi-degenerate regime of the bound state with the incoming free atoms) the scattering length takes large values and the unitarity regime of eq. (2.7) can be reached.

In the case of a magnetically induced Feshbach resonance the s-wave scattering length a_s can be written as a function of the magnetic field B [33]:

$$a_\mathrm{s}(B) = a_\mathrm{bg}\left(1 - \frac{\Delta}{B - B_0}\right). \tag{2.8}$$

Here B_0 denotes the position of the resonance, Δ its width and a_bg the background scattering length.

The tunable coupling between the open channel and some bound state in the closed channel allowed to manipulate the scattering properties of the atoms. This tuning can also be done using an optical coupling [34] or a microwave coupling [35]. Moreover,

the Feshbach resonances can be manipualted using optical methods [36] or rf photons [37].

2.1.3. Mean-Field Approximation: Gross-Pitaevskii-Equation

In order to describe the weakly interacting Bose gases realized in experiments, interactions need to be included in the theory. Weakly interacting or dilute in this context means the scattering length is always much smaller than the interparticle spacing $n|a|^3 \ll 1$. The Hamiltonian of such a system in second quantization reads:

$$\begin{aligned}\hat{H} = \int d^3r \hat{\Psi}^\dagger(r) \left(-\frac{\hbar^2\nabla^2}{2m} + V_{\text{ext}}(r) \right) \hat{\Psi}(r) \\ + \frac{1}{2} \int d^3r d^3r' \hat{\Psi}^\dagger(r) \hat{\Psi}^\dagger(r') V(r-r') \hat{\Psi}(r') \hat{\Psi}(r),\end{aligned} \tag{2.9}$$

where the first term resembles the non-interacting Bose gas in an external potential $V_{\text{ext}}(r)$ and the second term the interaction due to the interatomic potential $V(r-r')$. The latter one can be approximated by the contact interaction potential

$$V(r-r') = g\delta(r) \tag{2.10}$$

with $g = 4\pi\hbar^2 a/m$ being the coupling constant. This assumption is justified, since we are interested in the low energy solutions of the problem where the deBroglie wavelength λ_{dB} is much larger than the fine details of the interaction potential. $\hat{\Psi}^\dagger(r)$ and $\hat{\Psi}(r)$ are the bosonic field operators creating and annihilating a particle at position r.

If the temperature is assumed to be close to zero (i.e. $T \ll T_{\text{c}}$) the occupation of excited states can be neglected and the field operators can be approximated by their expectation values

$$\hat{\Psi}(r,t) = \underbrace{\left\langle \hat{\Psi}(r,t) \right\rangle}_{\equiv\psi(r,t)} + \hat{\Psi}'(r,t) \tag{2.11}$$

thereby introducing the condensate wavefunction $\psi(r,t)$. $\hat{\Psi}'(r,t)$ is treated as a small pertubation and will be neglected in the following, since almost all the atoms are occupying the ground state $\psi(r,t) \sim \sqrt{N}$ of the potential. Using this definition in eq. (2.9) leads to the time dependent Gross-Pitaevskii equation (GPE) [38, 39]:

$$i\hbar\frac{\partial}{\partial t}\psi(r,t) = \left(-\frac{\hbar^2}{2m}\nabla^2 + V_{\text{ext}} + g|\psi(r,t)|^2 \right) \psi(r,t) \tag{2.12}$$

The time-independent GPE can be obtained by introducing the chemical potential $\mu = \partial E/\partial N$ via $\psi(r,t) = \psi(r)\exp(-i\mu t/\hbar)$.

$$\mu\psi(r) = \left(-\frac{\hbar^2}{2m}\nabla^2 + V_{\text{ext}} + g|\psi(r)|^2 \right) \psi(r) \tag{2.13}$$

Note that here the condensate wavefunction is normalized to the total number of particles N (i.e. $\int dr|\psi(r)|^2 = \int drn(r) = N$) which also fixes the value of the chemical potential, $n(r)$ is the particle density of the system. The fact that the time evolution of the ground state wavefunction is given by the chemical potential μ rather than the single particle energy E as in the normal Schrödinger equation is a consequence of the mean-field description of the interparticle interaction being proportional to $gn(r)$. $\psi(r)$ is thus the ground state wavefunction of all the atoms occupying this lowest state and not a single particle wavefunction.

Healing Length

In a box potential where the external potential in eq. (2.13) can be set to zero the wavefunction will be defined by the kinetic and interaction energy only. At the borders of the box potential the wavefunction must grow from 0 to some finite value. However the steeper this growth, the more kinetic energy is stored in the system, such that there will be a finite length scale ξ where the kinetic energy ($E_{\text{kin}} \sim \hbar^2/2m\xi^2$) is about the same value as the interaction energy ($E_{\text{int}} \sim 4\pi\hbar^2 an/m$). Setting these terms to be equal $E_{\text{kin}} = E_{int}$ leads to

$$\xi = \frac{1}{\sqrt{8\pi na}} \tag{2.14}$$

where ξ is called the healing length because it gives a measure over which distances the condensate wavefunction can "heal" disturbances due to the potential. In experiments with a typical particle density of $n = 10^{14}\text{cm}^{-3}$ and a scattering length of $a = 63a_0$, the healing length is in the range of 345 nm.

Thomas-Fermi Approximation

Most experiments work with atomic species with repulsive interaction ($a > 0$). Also the atom numbers are quite large and the confining potential is moderate. In this situation the kinetic energy of the condensate fraction is negligible compared to the interaction energy and the Thomas-Fermi (TF) approximation applies. It is applicable if $Na/a_{\text{ho}} \gg 1$, where $a_{\text{ho}} = \hbar/m\omega_{\text{ho}}$ is the harmonic oscillator length and defines the size of the ground state wavefunction in a harmonic potential[2]. The kinetic energy term of eq. (2.13) is neglected and the particle density of the condensate resembles the external potential:

$$n(r) = \begin{cases} \frac{\mu - V_{\text{ext}}(r)}{g} & \text{for} \quad \mu - V_{\text{ext}}(r) > 0 \\ 0 & \text{else} \end{cases} \tag{2.15}$$

Note that neglecting the kinetic energy compared to the interaction energy is in no contradiction to the claim of a weakly interacting gas. The GPE describes the $T = 0$

[2] with the geometic average of the trapping frequencies $\omega_{\text{ho}} = (\omega_{\text{x}}\omega_{\text{y}}\omega_{\text{z}})^{1/3}$

physics of the ground state of the BEC phase. Here the kinetic energy is always small and interactions are important, whereas weakly interacting implies $n|a|^3 \ll 1$.

The chemical potential is again fixed by the normalization condition and reads as follows.

$$\mu = \frac{\hbar\omega_{\mathrm{ho}}}{2}\left(\frac{15Na}{a_{\mathrm{ho}}}\right)^{2/5} \tag{2.16}$$

The width of the condensate is calculated by setting $\mu = V_{\mathrm{ext}}(R_i^{\mathrm{B}})$ and yields the Thomas-Fermi radii for bosons:

$$R_i^{\mathrm{B}} = \sqrt{\frac{2\mu}{m\omega_i^2}} = a_{\mathrm{ho}}\frac{\omega_{\mathrm{ho}}}{\omega_i}\left(\frac{15Na}{a_{\mathrm{ho}}}\right)^{1/5} \tag{2.17}$$

Using these expressions in eq. (2.15) yields the Thomas-Fermi density profile in a three dimensional harmonic trapping potential $V_{\mathrm{ext}}(r) = \frac{1}{2}m(\omega_x^2x^2 + \omega_y^2y^2 + \omega_z^2z^2)$:

$$n(r) = \frac{15}{8\pi}\frac{N}{R_x^{\mathrm{B}}R_y^{\mathrm{B}}R_z^{\mathrm{B}}}\left[1 - \left(\frac{x}{R_x^{\mathrm{B}}}\right)^2 - \left(\frac{y}{R_y^{\mathrm{B}}}\right)^2 - \left(\frac{z}{R_z^{\mathrm{B}}}\right)^2\right] \tag{2.18}$$

2.1.4. Excitations of the Interacting BEC: Bogoliubov Transformation

Up to this point only the ground state properties of the condensate fraction was of interest and all excitations have been neglected. In the following small excitations of the system will be allowed. These are assumed to be counterpropagating plain waves characterized by a frequency ω_i and complex amplitudes $u_i(r)$ and $v_i(r)$. The energy of the ith excitation is $\hbar\omega_i$. In order to calculate the energy spectrum of these excitations, we try to find solutions to eq. (2.9) of the form [39]

$$\psi(r,t) = \left[\psi(r) + \sum_i \left(u_i(r)e^{-i\omega_i t} + v_i^*(r)e^{i\omega_i t}\right)\right]e^{-i\mu t\hbar} \tag{2.19}$$

which describes small oscillations of the wavefunction around its ground state value. Note that in this representation we still use the classical wavefunction $\psi(r,t)$ rather than the quantized field operator $\hat{\Psi}(r,t)$. Since the pertubations are assumed to be small compared to $\psi(r) \sim \sqrt{n(r)}$, only the linear terms in the complex functions $u(r)$ and $v(r)$ are kept and the time-dependent GPE yields two coupled equations for those functions:

$$\hbar\omega_i u_i(r) = \left(-\frac{\hbar^2}{2m}\nabla^2 + V_{\mathrm{ext}}(r) - \mu + 2gn(r)\right)u_i(r) + gn(r)v_i(r) \tag{2.20a}$$

$$-\hbar\omega_i v_i(r) = \left(-\frac{\hbar^2}{2m}\nabla^2 + V_{\mathrm{ext}}(r) - \mu + 2gn(r)\right)v_i(r) + gn(r)u_i(r) \tag{2.20b}$$

By solving these, one can calculate the eigenenergies $\hbar\omega_i$ of the excitations and thus their spectrum. For instance in a uniform gas the spectrum reveals the Bogoliubov dispersion law [40]:

$$\hbar\omega = \sqrt{\frac{\hbar^2 q^2}{2m}\left(\frac{\hbar^2 q^2}{2m} + 2gn\right)} \tag{2.21}$$

where q is the wave vector of the excitation. For low momenta the spectrum is linear (phonon-like) with $\omega = cq$, where $c = \sqrt{gn/m}$ is the sound velocity in the gas. For large momenta $q > 1/\xi$ the dispersion law is quadratic in q and thus shows a free-particle like behavior $\omega = \hbar q^2/2m$.

The quantity $\int dr(|u_i|^2 - |v_i|^2) = \tilde{N}$ can be identified as the number of excitations $\tilde{N} = \sum_i \hat{\alpha}_i^\dagger \hat{\alpha}_i$ in the system when comparing to the quantized version of eq. (2.19):

$$\hat{\Psi}(r,t) = \left[\psi(r) + \sum_i \left(\tilde{u}_i(r)\hat{\alpha}_i e^{-i\omega_i t} + \tilde{v}_i^*(r)\hat{\alpha}_i^\dagger e^{i\omega_i t}\right)\right] e^{-i\mu t\hbar} \tag{2.22}$$

Here $\hat{\alpha}_i^\dagger$ and $\hat{\alpha}_i$ with i being the quasiparticle index create and annihilate a quasiparticle in the excitation spectrum. By requiring bosonic commutation relations for $\hat{\alpha}_i$ and $\hat{\alpha}_i^\dagger$ one finds the normalization condition for the $\tilde{u}_i(r)$ and $\tilde{v}_i(r)$:

$$|\tilde{u}_i(r)|^2 - |\tilde{v}_i(r)|^2 = 1 \tag{2.23}$$

With this transformation the Hamiltonian can be diagonalized in the Bogoliubov approximation and one finds the same energy spectrum as in eq. (2.21). Note that even at zero temperature the number of excitations is still finite, although very small.

The Bogoliubov transformation is valid as long as the occupation number of the quasiparticle states $\tilde{N} \ll N$ is small compared to the total atom number N. Otherwise the linearization of eq. (2.19) in the complex functions $u_i(r)$ and $v_i(r)$ would not be a good approximation anymore and higher order terms had to be included.

2.2. Degenerate Fermions

In the previous section the theoretical description of weakly interacting Bose gases has been recalled. The following section is dealing with fermions. In this case the Pauli exclusion principle requires an antisymmetric wavefunction under particle exchange which has dramatic consequences for the properties of the gas. In the bosonic case a macroscopic occupation of the ground state leads to Bose-Einstein condensation and a mean-field model could be developed to describe the behavior of this state. In the case of fermionic atoms, the Pauli exclusion principle however forbids an occupation number larger than 1 for every state, such that at low enough energies the fermions will pile up in a row filling the traps eigenstates from the ground state on up to the highest occupied state at the Fermi energy E_F. The mean occupation number of state i with the energy E_i follows from the Fermi-Dirac statistics:

$$\langle n_i \rangle = \frac{1}{\exp\left[\beta\left(E_i - \mu\right)\right] + 1} \overset{T \to 0}{=} \begin{cases} 1 & \text{for} \quad E_i < \mu \\ 0 & \text{for} \quad E_i > \mu \end{cases} \tag{2.24}$$

where $\beta = 1/k_{\mathrm{B}}T$ and k_{B} is the Boltzmann constant. $E_i = p^2/2m + V_{\mathrm{ext}}(r)$ is the energy of particle i in an external potential $V_{\mathrm{ext}}(r)$. Again, the chemical potential is fixed by the normalization condition

$$N_{\mathrm{s}} = \frac{1}{(2\pi\hbar)^3} \int d^3r d^3p \, \langle n_i \rangle \tag{2.25}$$

with N_{s} being the number of atoms in a specific spin state s. In the case of vanishing temperature the chemical potential is the energy of the last occupied state which will be denoted by the Fermi energy E_{F}. In this case and for large atom numbers in a harmonic confinement, the above normalization condition yields the Fermi energy as follows:

$$E_{\mathrm{F}} \equiv k_{\mathrm{B}} T_{\mathrm{F}} = \hbar\omega_{\mathrm{ho}} (6N)^{1/3}. \tag{2.26}$$

Here the Fermi temperature T_{F}, related to the Fermi energy has been introduced.

Thomas-Fermi Approximation for Fermions

Using the Fermi energy one can express the density distribution $n_{\mathrm{F}}(r)$ in coordinate space in a similar way as in the bosonic case. The $T = 0$ limit of eq. (2.24) is integrated over all momenta $|p| < \sqrt{2m(E_{\mathrm{F}} - V_{\mathrm{ext}}(r))}$:

$$n_{\mathrm{F}}(r) = \frac{8}{\pi} \frac{N}{R_x^{\mathrm{F}} R_y^{\mathrm{F}} R_z^{\mathrm{F}}} \left[1 - \left(\frac{x}{R_x^{\mathrm{F}}} \right)^2 - \left(\frac{y}{R_y^{\mathrm{F}}} \right)^2 - \left(\frac{z}{R_z^{\mathrm{F}}} \right)^2 \right]^{3/2} \tag{2.27}$$

where the $R_i^{\mathrm{F}} = a_{\mathrm{ho}} (48N)^{1/6} \omega_{\mathrm{ho}}/\omega_i$ denote the zero temperature widths of the density distribution. This derivation is valid as long as the Fermi energy is much larger than the level spacing $\hbar\omega_i$ of the trap. This density profile is sometimes also referred to as the Thomas-Fermi profile.

2.3. Polaron Problem

Up to know the description of a single component Bose gas at low temperatures and fermions in the mean-field limit has been discussed. But what happens if an impurity of a second species is added to the system? Such systems are already known from condensed matter physics where impurities always degrade the samples. An example is the electron, moving through an ionic crystal lattice. The crystal lattice has its own excitation spectrum revealing a dispersion relation and the electron interacts with these lattice oscillations. This system – electron plus accompanying lattice excitations

– can be described as a new quasiparticle—the polaron. A review of the theoretical concepts, describing this system can be found in [41].

A system of one impurity atom being placed into a background BEC should also show a similar behavior. The impurity can travel through the background gas where in contrary to the condensed matter system the mutual interaction strength can be chosen almost arbitrarily using Feshbach resonances.

2.3.1. Condensed Matter Treatment

As pointed out by Tempere *et. al.* [42] the ultracold atomic system can be mapped onto the Fröhlich polaron Hamiltonian [18]. In the following, the results shall be explained briefly along the lines of ref. [42].

The Fröhlich Hamiltonian of a slow[3] moving impurity (electron with bare mass m_e in the condensed matter system) trough an ionic crystal lattice reads as:

$$\hat{H}_{\text{polaron}} = \frac{\hat{p}^2}{2m_{\text{e}}} + \sum_{k\neq 0} \hbar\omega_k \hat{b}_k^\dagger \hat{b}_k + \sum_{k\neq 0} V_k e^{ikr} \left(\hat{b}_k + \hat{b}_{-k}^\dagger\right), \tag{2.28}$$

where the first term is the kinetic energy of the electron and the second term the excitation spectrum of the ionic crystal lattice, i.e. the phonons with energy $\hbar\omega_k$. The $\hat{b}_k^\dagger$ and $\hat{b}_k$ are the phonon creation and annihilation operators fulfilling the bosonic commutation relations.

$$\left[\hat{b}_k, \hat{b}_{k'}^\dagger\right] = \delta_{k,k'} \qquad \left[\hat{b}_k, \hat{b}_{k'}\right] = 0 \qquad \left[\hat{b}_k^\dagger, \hat{b}_{k'}^\dagger\right] = 0 \tag{2.29}$$

The last term of eq. (2.28) describes the electron-phonon interaction with V_k being the k component of the Fourier transform of this interaction potential. The interaction strength can be expressed by a single, dimensionless interaction parameter α which denotes the electron-phonon coupling [18].

If this coupling is weak, the electron can propagate through the crystal as a free particle. The weak coupling to the ionic lattice can be written as a contribution to the mass, such that the polaron mass will be the bare electron mass plus a small contribution due to the interaction with the lattice phonons. This effective mass description allows to use the same description for the electron movement as in the absence of electron-phonon interaction. The effective mass m^* of the moving polaron will be $m^* \simeq m(1 + \alpha/6)$ and polaron energy will be the energy of the free moving electron – with a modified mass – plus a small correction due to the interaction with a low energy (i.e. $k = 0$ in the dispersion relation) lattice phonon $E \simeq \hbar^2 k^2/2m^* - \alpha\hbar\omega_{k=0}$.

If the electron-phonon interaction is very large, the potential energy due to local lattice deformations can exceed the kinetic energy of the electron. The electron is

[3] slow in this context means: the ionic crystal lattice can adapt to the presence of the electron disturbing the lattice and retardation effects can be neglected

dressed with a phonon cloud [41] and gets localized to a single lattice ion. In this regime the effective mass of the polaron depends strongly on the coupling parameter $m^*/m \propto \alpha^4$. This localization of the electron and therewith also the localization of the polaron is predicted to show up in a sudden mass increase. If the electron is interacting with acoustic phonons, this increase is predicted to be a mass jump over several orders of magnitude [43].

In order to map this system onto an impurity atom moving through a background BEC, the Hamiltonian of this system has to be considered [42]:

$$H = \frac{p^2}{2m_\mathrm{I}} + \sum_k \epsilon_k \hat{a}_k^\dagger \hat{a}_k + \frac{1}{2}\sum_{k,k',q} V_\mathrm{BB}(q)\hat{a}_{k'-q}^\dagger \hat{a}_{k+q}^\dagger \hat{a}_k \hat{a}_{k'} + \sum_{k,q} V_\mathrm{IB}(q)\rho_\mathrm{I}(q)\hat{a}_{k'-q}^\dagger \hat{a}_{k'} \quad (2.30)$$

The $\hat{a}_k^\dagger$ and $\hat{a}_k$ are the boson creation and annihilation operators correspondingly to the $\hat{b}$ in eq. (2.28) and act on the background atoms with wavenumber k, mass m_B and energy $\epsilon_k = -\mu + \hbar^2 k^2/2m_\mathrm{B}$. Thus the second term in eq. (2.30) corresponds to the kinetic energy of the bosonic background atoms and the third term describes the intraspecies interaction of the background via the interaction potential V_BB. The first and fourth term describe the kinetic energy and the interspecies interaction of impurity to background via the interaction potential V_IB respectively and $\rho_I(q)$ denotes the Fourier transform of the impurity density. In the Bogoliubov approximation this Hamiltonian reduces to:

$$\begin{aligned} H = E_\mathrm{GP} + N_0 V_\mathrm{IB}(0) + \frac{p^2}{2m_\mathrm{I}} + \sum_{k\neq 0} E_k \hat{b}_k^\dagger \hat{b}_k \\ + \sum_{k\neq 0} \sqrt{\frac{\xi_k N_0}{E_k}} V_\mathrm{IB}(k)\rho_\mathrm{I}(k)\left(\hat{b}_k + \hat{b}_{-k}^\dagger\right) \end{aligned} \quad (2.31)$$

Similar to eq. (2.28) here the $\hat{b}_k^\dagger$ and $\hat{b}_k$ create and annihilate Bogoliubov excitations. Also these excitations follow the known dispersion relation similar to eq. (2.21):

$$E_k = \sqrt{\xi_k\left(\xi_k + 2N_0 V_\mathrm{BB}(k)\right)}, \quad (2.32)$$

which is linear for small k. $\xi_k = \hbar^2 k^2/2m_\mathrm{B}$ is the single particle energy of a background atom. E_GP is the energy related to the GPE of the background atoms only. The Hamiltonians (2.28) and (2.31) can be mapped onto each other by choosing

$$\hbar\omega_k = ck\sqrt{1 + \xi^2 k^2/2} \quad (2.33)$$

$$V_k = g_\mathrm{IB}\sqrt{N_0}\left(\frac{\xi^2 k^2}{\xi^2 k^2 + 2}\right)^{1/4} \quad (2.34)$$

$$(2.35)$$

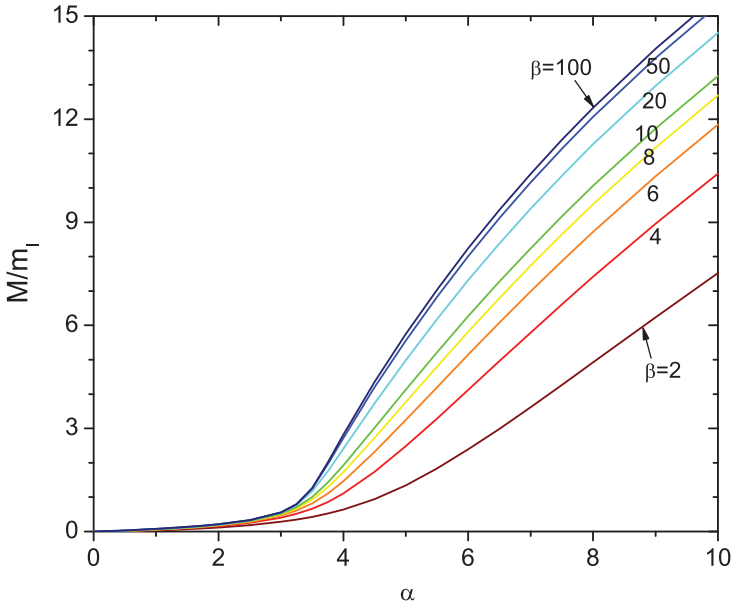

Figure 2.3.: *The variational mass parameter M of the impurity atom [42] as a function of the coupling parameter α. The different colors correspond to different temperatures $\beta = 1/k_B T$. The effective mass of the polaron is to a good approximation given by $m_{pol} = m_I + M$ where m_I is the mass of the bare impurity, such that M/m_I corresponds to the effective mass increase of the polaron. The plot is taken from [42].*

where $\xi = 1/\sqrt{8\pi a_{\mathrm{BB}} n_0}$ is the healing length of the condensate and c the speed of sound. The polaron coupling constant in this context reads:

$$\alpha = \frac{a_{\mathrm{IB}}^2}{a_{\mathrm{BB}}\xi}. \tag{2.36}$$

This quantity will also be used in the next chapters, where we tackle the polaron problem numerically.

Tempere *et al.* solve the Fröhlich Hamiltonian using a Feynman path integral approach that is valid at all coupling strengths α and calculate the effective mass of the impurity, fig. 2.3, as a function of α. At small coupling strengths α, where the impurity is coupled weakly to the background BEC, the effective mass increases linearly with α, consistent with a pertubative approach of the impurity-background coupling. When α is increased above the critical value of $\alpha_{\mathrm{crit}} \sim 3.5$, the behavior changes dramatically. The effective mass increases rapidly with increasing α, although no mass jump as in the case of acoustic polarons is observed. As the temperature is increased, the crossover from weak to strong coupling becomes less dramatic and smears out as $T \to T_{\mathrm{c}}$ of the background BEC. The strong increase of the effective mass is identified with a crossover from a quasifree to a self-trapped impurity.

2.3.2. Cold Atomic Gases Perspective

Cold atomic gases offer a variety of polaron-type model systems. Recently, experiments at MIT [44] and ENS [45] observed a polaronic behavior when studying an imbalanced, degenerate Fermi gas in the unitarity limit.

Unitarity in this context describes an interacting system, where the interparticle scattering length a exceeds the interparticle spacing $n^{-1/3} \propto k_{\mathrm{F}}^{-1}$ by far, such that the dimensionless interaction strength $1/k_{\mathrm{F}}a$ tends to zero. k_{F} refers to the Fermi wavevector which is defined as $k_{\mathrm{F}} = \sqrt{2mE_{\mathrm{F}}/\hbar}$. In these systems the scattering length a cannot be of relevance to describe the behavior of the system. The only relevant length scale is the interparticle distance $n^{1/3}$, the system is said to be universal [46].

Both groups at MIT and ENS study a two component Fermi gas of ^{6}Li, where one component – say $|\uparrow\rangle$ – has a majority concentration and only a few percent $|\downarrow\rangle$ atoms are immersed into the Fermi sea of $|\uparrow\rangle$ atoms. The MIT group measures the response of the strongly imbalanced mixture on rf photons, thus spectrally resolving the excitation spectrum of the system [44]. They observe a spectral response in the minority component, identified as a Fermi-polaron, at large interaction strengths. As the interaction strength is decreased, the Fermi-polaron response vanishes until the formation of molecules in both spectra is observed. The position of the polaron peak in their measured rf-spectrum corresponds to the polaron binding energy, which is below the molecular binding energy for their set of parameters. They observe a vanishing polaron signal, as soon as molecules are observed.

The ENS group investigates the oscillation modes of a Fermi spin mixture at unitarity. As the imbalance is increased (i.e. the relative number of minority atoms is reduced), they observe a second frequency in the oscillation of the minority component. This frequency is identified to be originating from Fermi-polarons with an effective mass of $m_{\mathrm{eff}}/m = 1.17(10)$ [45]. In another experiment at the ENS group, the equation of state of a universal Fermi gas is mapped out and the effective mass of the Fermi-polaron at unitarity is measured to be $m_{\mathrm{eff}}/m = 1.20(2)$ [47].

Recent theoretical work [48, 49, 50] allows to draw the following picture of the situation: Starting with a degenerate Fermi gas of $|\uparrow\rangle$ atoms and immersing one fermionic $|\downarrow\rangle$ impurity at small repulsive interparticle scattering lengths $a > 0$, the impurity atom will form a dimer with exactly one $|\uparrow\rangle$ atom. The dimer will be deeply bound and the bond length will be much smaller than the interparticle distance. The dimer can be viewed as a molecule of mass $2m$. Following the dimers binding energy into the unitarity limit ($a \to \infty$), reveals a vanishing binding energy hitting the free particle threshold at $1/k_F a = 0$. Nevertheless , this simple picture of a two-body bound state is only true in the limit of small a such that $1/k_{\mathrm{F}}a \gg 1$. As the scattering length increases, the bound state is a many-body effect, including particle-hole excitations of the $|\uparrow\rangle$ Fermi sea of low order [51].

As the interaction parameter approaches $1/k_{\mathrm{F}}a \simeq 0.9$, the bound dimer state is no longer the ground state of the system, but a $|\downarrow\rangle$ atom, dressed with a localized cloud of $|\uparrow\rangle$ atoms—the Fermi-polaron. Accounting a system of a single $|\downarrow\rangle$ fermion in a sea of $|\uparrow\rangle$ atoms and allowing only single particle-hole excitations in the system,

describes the ground state of the Fermi-polaron sufficiently. The transition from the Fermi-polaron to a bound state being the ground state of the system is a 1st order phase transition.

As a reminder, these measurements have been performed using a fermionic impurity immersed into a Fermi sea of background atoms. A reason for the upper bound of the polaron mass to $m_{\text{eff}}/m = 1.20(2)$ [47] might be, that the mass increase is due to single particle-hole excitations of the Fermi sea. Although measured at unitarity, the higher order particle-hole excitations do not contribute to the polaron energy [51] and there is also no other energy scale present that could influence the polaron. Furthermore, the increased interspecies scattering length between the $|\downarrow\rangle$ particle and the $|\uparrow\rangle$ Fermi sea leading to single particle-hole excitations also determines the interaction between the formed particle-hole pair and the Fermi sea.

In contradiction, in a system of bosonic background the effective mass of the impurity atom is not bound to such a low value but seems rather to be unbound [42]. Here the impurity is interacting with the Bogoliubov modes of the background, having a bosonic character. Up to the authors knowledge, there are no published results involving an impurity atom in a bosonic gas of background atoms with tunable interaction. This system will be studied in the following chapters using a rather simple mean-field approach to the BEC-impurity problem. The results will be presented in chapter 4 and will be compared to the many body approach of *Tempere et. al.*.

3. Numerical Methods

In this chapter the reader will be introduced to a mean-field description of two interacting atomic species, since this will be relevant to understand the polaron concept in the ultracold atom context. A two-component GPE will be solved numerically in a spherically-symmetric potential and a measure of the effective mass of the impurity atoms will be presented. The next chapter will present the numerical solutions of the two-component GPE obtained, using the methods presented here. The system of interest should contain a large background BEC in a moderate trap ($\equiv$ ionic crystal lattice), such that the wavefunction in the center is almost flat and the single (or few) impurities can be localized in a region of almost constant background density using a tight confinement.

3.1. Two-Component GPE

Considering a system of two bosonic atomic species (denoted by the indices 1 and 2 respectively) in an external potential $V_{\mathrm{ext},i}(r)$ the GPE (2.13) can be written as follows.

$$\mu_i\psi_i(r) = \left[-\frac{\hbar^2}{2m_i}\nabla_i^2 + V_{\mathrm{ext},i}(r) + (N_i-1)g_{ii}|\psi_i(r)|^2 + N_j g_{ij}|\psi_j(r)|^2\right]\psi_i(r). \quad (3.1)$$

In this notation μ_i is the chemical potential, $g_{ii} = 4\pi\hbar^2 a_{ii}/m_i$ the intraparticle interaction and $g_{ij} = 2\pi\hbar^2 a_{ij}/m_{ij}$ the coupling constant between the different species i and j. $m_{ij} = m_i m_j/(m_i+m_j)$ denotes the reduced mass. The wavefunction $\psi_i(r)$ is normalized to 1 such that $\int |\psi_i(r)|^2 dr = 1$.

In general, solving this equation in three dimensions for any given potential shape is a hard computational task. The particle density needs to be discretized on a grid with N_{grid} points with spacing dr as shown in fig. 3.1. dr needs to be small enough such that the density $n(k \times dr)$, where $k = [1, N_{\mathrm{grid}}]$, changes considerably little, such that the discretized wavefunction is a good approximation of the continuous one. An imaginary time propagation algorithm [52] works if the number of grid points N_{grid} is not too large. If a very localized impurity should be considered, a fine grid is required. But nevertheless the grid must be large enough to capture the large dimensions of the background BEC, which increases the number of grid points to a very large value. A three-dimensional algorithm without introducing any symmetry in order to reduce the grid size, will be thus very memory space consuming and cannot be calculated.

The question that should be discussed is how the presence of the background BEC influences the properties of the impurities and vice versa. The impurity density will be

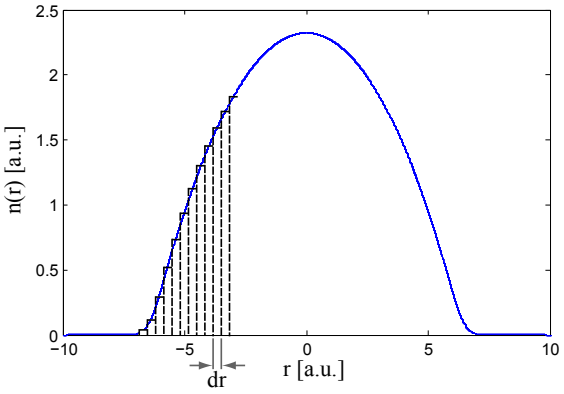

Figure 3.1.: *Particle density discretized of a grid with spacing dr. The number of such discrete steps is* N_{grid}.

peaked in the center of the background gas, and requires a fine grid. For this reason some simplifying assumptions concerning the trapping geometry will be made.

Spherically Symmetric GPE

The trapping potential is in the following assumed to be a spherically symmetric harmonic oscillator. Suppose that $\Phi(r) = r\psi(r)$, $a_m = m_2/m_1$ is the mass ratio and $a_\omega = \omega_2/\omega_1$ is the ratio of trapping frequencies for the different species. The harmonic oscillator length $a_{\mathrm{ho}} = \sqrt{\hbar/m_1\omega_1}$ for species 1 serves as a natural scaling factor. In this case the two-component GPE (3.1) reads:

$$\begin{aligned}\mu_1\Phi_1(r) = \frac{\hbar^2}{m_1}\Bigg[&-\frac{1}{2}\frac{\partial^2}{\partial r^2} + \frac{1}{2}\frac{r^2}{a_{\mathrm{ho}}^4} + 4\pi(N_1-1)a_{11}\frac{|\Phi_1(r)|^2}{r^2} \\ &+2\pi N_2 a_{12}\frac{1+a_m}{a_m}\frac{|\Phi_2(r)|^2}{r^2}\Bigg]\Phi_1(r)\end{aligned} \tag{3.2a}$$

$$\begin{aligned}\mu_2\Phi_2(r) = \frac{\hbar^2}{m_1}\Bigg[&-\frac{1}{2a_m}\frac{\partial^2}{\partial r^2} + \frac{1}{2}a_m a_\omega^2\frac{r^2}{a_{\mathrm{ho}}^4} + 2\pi N_1 a_{12}\frac{1+a_m}{a_m}\frac{|\Phi_1(r)|^2}{r^2} \\ &+4\pi(N_2-1)\frac{a_{22}}{a_m}\frac{|\Phi_2|^2}{r^2}\Bigg]\Phi_2(r)\end{aligned} \tag{3.2b}$$

In order to solve this set of differential equations numerically, a computation grid has to be introduced and thus the solution is discretized on this grid. In first approximation the 2$^{\mathrm{nd}}$ derivertive takes the following form with dr being the gridspacing and k the grid index ranging from 1 to N_{grid}.

$$\frac{\partial^2\Phi}{\partial r^2} \to \frac{\Phi^{k-1} - 2\Phi^k + \Phi^{k+1}}{(dr)^2} \tag{3.3}$$

Matrix Diagonalization and Eigenfunction Search

When rewriting equations (3.2) on a discrete grid, the problem of solving these differential equations reduces to a diagonalisation of a tridiagonal matrix for each species. Both matrices are coupled via the mutual interaction of impurity and background atoms. This can be done very efficiently using *Matlab's* sparse matrix notation. The principle diagonal of these matrices contains the kinetic energy $\tilde{E}^k_{\mathrm{kin},i} = \hbar^2/m_i/(dr)^2$ and the effective potential $V^k_{\mathrm{eff},i}$, consisting of the harmonic oscillator potential, the intraspecies interaction term and the interspecies interaction.

$$V^k_{\mathrm{eff},1} = \frac{\hbar^2}{m_1}\left(\underbrace{\frac{1}{2}\frac{(kdr)^2}{a^4_{\mathrm{ho}}}}_{\text{harm. osc.}} + \underbrace{4\pi a_{11}(N_1-1)\frac{|\Phi^k_1|^2}{(kdr)^2}}_{\text{intraspecies interaction}} + \underbrace{\frac{1+a_m}{a_m}2\pi N_2 a_{12}\frac{|\Phi^k_2|^2}{(kdr)^2}}_{\text{interspecies interaction}}\right) \tag{3.4}$$

The secondary diagonals are filled with the couplings:

$$\delta_1 = -\frac{\hbar^2}{2m_1}\frac{1}{(dr)^2} \tag{3.5}$$

and in an analog way for species 2. The matrix to be diagonalized is a $N_{\mathrm{grid}} \times N_{\mathrm{grid}}$ matrix with the following structure:

$$M_1 = \begin{pmatrix} V^1_{\mathrm{eff},1} + \tilde{E}^1_{\mathrm{kin},1} & \delta_1 & 0 & \cdots \\ \delta_1 & V^2_{\mathrm{eff},1} + \tilde{E}^2_{\mathrm{kin},1} & \delta_1 & \\ 0 & \delta_1 & V^3_{\mathrm{eff},1} + \tilde{E}^3_{\mathrm{kin},1} & \\ \vdots & & & \ddots \end{pmatrix} \tag{3.6}$$

Solving the coupled GPE (3.1) has now been reduced to solving the following eigenvalue problem:

$$\mu_i \begin{pmatrix} \Phi^1_i \\ \vdots \\ \Phi^k_i \\ \vdots \\ \Phi^{N_{\mathrm{grid}}}_i \end{pmatrix} = M_i \begin{pmatrix} \Phi^1_i \\ \vdots \\ \Phi^k_i \\ \vdots \\ \Phi^{N_{\mathrm{grid}}}_i \end{pmatrix} \tag{3.7}$$

The smallest eigenvalue of species i is the chemical potential μ_i if the corresponding eigenvector Φ_i resembles the ground state wavefunction.

The basic idea of the numerical code is very simple. The starting point is determined by a qualified guess, which in this case is a normalized gaussian. Then the effective potential for both species is calculated, the resulting tridiagonal matrix is diagonalized and the eigenvector $\Phi_{i,\,\mathrm{new}}$ corresponding to the smallest eigenvalue is determined. The wavefunction for the next iteration step is computed by

$\Phi_i = \sqrt{(1-\epsilon)|\Phi_{i,\,\mathrm{old}}|^2 + \epsilon|\Phi_{i,\,\mathrm{new}}|^2}$ following the ideas of Pu and Bigelow [53]. ϵ is a number between 0 and 1 and ensures the convergence of the code. This computation loop stops when the change of the smallest eigenvalue—the chemical potential μ_i—is sufficiently small. After each loop the calculated wavefunctions are normalized such that $4\pi \sum_k dr|\Phi^k|^2 = 1$. In order to test the code some examples presented by Pu and Bigelow [53] and Kalas and Blume [54] have been calculated with this code and good agreement was found.

The eigenvector Φ_i associated with the smallest eigenvalue μ_i describes the ground state of the condensate of species i. Note that in this calculation method the second-smallest eigenvalue does not necessarily correspond to the first excited state of the system, since the phase of the eigenvectors is by construction always flat. The energy of the ground state can be increased just by modifying the phase while keeping the density profile constant[1]. These states cannot be found using this code, since there is no phase information in the formalism.

3.2. Effective Mass Determination

From the properties of the ground state wavefunction for every atomic species, one can gain insight into several properties. First of all the peak density of species i is given by $n_{0,i} = \max(N_i|\Phi_i|^2)$. By inserting the ground state wavefunction into eq. (3.4), the effective potential for each species can be calculated. This also provides a handle on the effective mass of the minority component due to the interaction with the background BEC.

The effective potential can be fitted quadratically in first order where the curvature c is determined by $c = m_{\mathrm{eff}}\omega_i^2/2$. But up to which distance from the center do we fit the effective potential to determine the effective mass of the impurity? If the fitting is done over the full grid size, basically to external potential is fitted and this procedure will regain the bare mass of the impurity. The mutual interaction changes the effective potential mainly in the center, where the impurity is localized. The root-mean-square (rms) size σ

$$\sigma = \sqrt{\langle r^2\rangle - \langle r\rangle^2} \tag{3.8}$$

of the impurity seems to be an appropriate length scale there. But as can be seen from fig. 3.2 (b), already at this scale the effective potential is highly non-harmonic. If the fitting radius is reduced further, the effective potential is highly overestimated at the wings of the impurity wavefunction which leads to an overestimation of the mass. On the other hand if the fitting radius is increased, the details of the potential get washed out and the mass is underestimated. These effects can be nicely seen in fig. 3.2 (a), where the effective mass m_{eff} of 1 ^{6}Li atom in the vicinity of 5×10^5 ^{23}Na atoms is plotted. The blue (red) shaded area is the effective mass when fitting to the impurity

[1] this state would not be the ground state any longer, since ground state refers to the state with the lowest possible energy

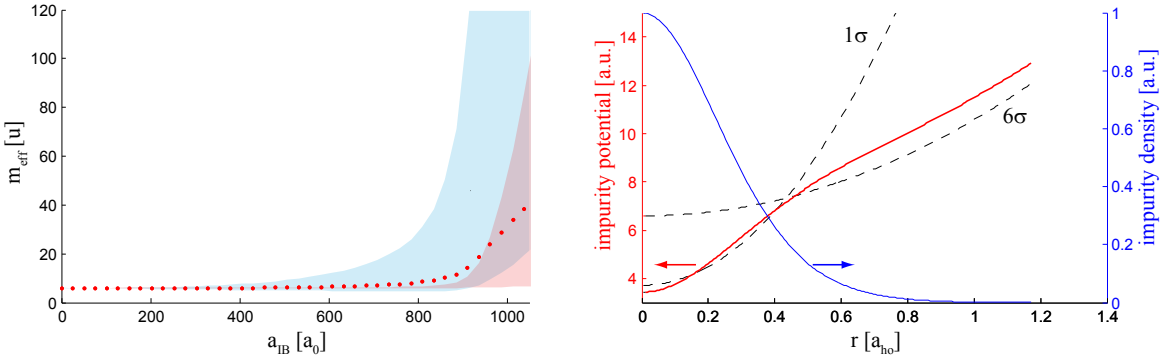

(a) **(b)**

Figure 3.2.: *(a): Effective mass determination using different methods. The dots (red) correspond to the effective mass using the rms width of the impurity wavefunction as a measure. The blue (red) shaded area is the effective mass when fitting the resulting impurity (background) potential up to a distance of 1σ to 6σ. (b): The effective impurity potential (red solid line) is shown and the quadratic fits to this potential (black dashed lines) up to 1σ and 6σ. For comparison, the impurity density (blue solid) linetrapped in the effective potential is plotted. The intraparticle scattering length of the background components is $63a_0$.*

(background) potential. The fit is performed up to a distance of 1σ up to 6σ of the impurity density. The large uncertainty region is due to the mentioned difficulties when choosing the fitting region. This is the main drawback of this method.

A parameter that is very sensitive to slight changes of the potential in the center regions however is the rms width σ of the impurity wavefunction. If the effective potential is assumed to be quadratic in first order, the ground state density will be that of a harmonic oscillator:

$$n(r) = N\left(\frac{m\omega}{\pi\hbar}\right)^{3/2}\exp\left[-\frac{m\omega r^2}{\hbar}\right] \tag{3.9}$$

$$\Rightarrow \quad m = \frac{3\hbar}{2\omega}\frac{1}{\langle r^2\rangle - \langle r\rangle^2} \tag{3.10}$$

Using eq. (3.10) the effective mass of the impurity atoms can be calculated using the trapping frequency of the applied external potential and the width of the impurity wavefunction as input parameters. The strength of this method is that it does no longer rely on an exact estimation of the interaction radius that determines the effective mass. Further, the approximation that the impurity density is a gaussian profile leads only to small errors, compared to the previous mentioned fitting method. In the following, we will therefore use the effective mass computed with this method.

3.3. Validity Considerations

Now that we have developed a method to solve eq. (3.2) numerically to calculate the ground state of a two-component BEC experiment in a spherical symmetric trap and having a method at hand to determine the effective mass of the impurities, we need to remember the validity of this method.

First of all, the background component needs to have a large atom number and not too high trapping frequencies in order to allow a mean-field description. For the impurities the same argument is true, however when dealing with 1 impurity atom only, the description stays valid since there is no intraspecies interaction. In this situation even the statistics of the impurity atom is irrelevant – may it be of bosonic or fermionic nature. The trapping frequency of the impurity component should be small enough, such that the intraspecies interaction can modify the potential sufficiently. In contrast to this, the trapping frequencies must be high enough to ensure that the potential modified by the interaction does not favor the impurities to be trapped in a region of space where no background atoms are present.

Since we are working with many impurity atoms in the experiment, the question rises if these are necessarily degenerate. Assuming a bosonic impurity, the scaling of the critical temperature T_c is the following:

$$\frac{T_\mathrm{c}^\mathrm{B}}{T_\mathrm{c}^\mathrm{I}} = \frac{\omega_\mathrm{ho}^\mathrm{B}}{\omega_\mathrm{ho}^\mathrm{I}} \left(\frac{N^\mathrm{B}}{N^\mathrm{I}} \right)^{1/3} \tag{3.11}$$

where the superscript B indicates the background species and I the impurity species. This means, if the background is a BEC at $T_\mathrm{c}/2$, the impurities are also degenerate if the trapping frequency is by more than a factor of 5 larger than the one for the background component – assuming 3 orders of magnitude more background atoms than impurity ones. On the other hand to ensure a localization of the impurity atoms inside the background BEC, the trapping frequency difference is almost always larger than this factor of 5. This is the reason why the impurity is not just a bunch of atoms but rather an impurity BEC.

If fermionic impurities are considered, the scaling of the critical temperature changes slightly – see eq. (2.26). At equal trapping frequencies and atom numbers, the Fermi temperature is by a factor of $6^{1/3}/0.94 \approx 2$ larger than the critical temperature for BEC. This means that under the same conditions as in the boson - boson case, the trapping frequency for the fermions must be at least a factor of 2.5 larger than the one for the bosonic background. Here the same conclusion holds: many fermions immersed in a bosonic background are not just a bunch of atoms but rather an immersed degenerate Fermi gas.

Recapitulatory, this chapter gave an introduction to the numerical methods, used to solve the problem of an impurity immersed in a bosonic background gas of atoms. The problem was restricted to the spherically symmetric case and the resulting two-component GPE was discretized on the calculation grid. A method to calculate the effective mass of the impurity has been developed.

4. Mean Field Simulation: 2 Component GPE

In the previous chapter the numerical methods have been presented, used to simulate a system with a background BEC with repulsive interaction, trapped in an external potential. A tightly confining trap immerses impurity atoms, which can be bosonic or fermionic. The impurity atom number is assumed to be small compared to that of the background and the trapping parameters are such that the impurity is always localized in the center of this three dimensional spherically symmetric trap.

In the following, the results of this numerical simulation will be presented. The first section will concentrate on a single impurity only, since this allows for a direct comparison to the calculations done using Feynman path integral methods valid for all coupling strengths by Tempere et. al. [42]. This ansatz is beyond the mean field calculations presented here and it will be interesting to see both the similarities and the differences. The second part of this chapter will deal with the situation that many impurities are immersed in a background BEC – a situation that will be more relevant for the experimental realization.

4.1. Single Impurity in a BEC Background

Here we will assume a background BEC of ^{23}Na atoms in a spherical symmetric trap with a trapping frequency of $\omega_{\mathrm{bg}} = 2\pi \times 100\mathrm{Hz}$. As the impurity component fermionic ^{6}Li will be used. The atom number of the background component will be varied in order to obtain results for different background densities and thus also change the ratio of a_{ho}/ξ, which will determine the validity of the calculation, where ξ is the healing length. The trapping frequency of the impurity atom will be chosen such that the impurity is always localized within the background BEC and the interparticle scattering length a_{IB} will serve as a free parameter of the calculation. Note that we will restrict ourselves to the case of repulsive interaction in the following. We will also use the harmonic oscillator length of the background component a_{ho} as a natural length unit. The peak densities will be expressed in atoms/cm^3 and mass units in u unless otherwise stated.

4.1.1. Impurity Localization

In order to study a polaron-type system using ultracold samples, the impurity atom needs to be localized in the BEC background using an external potential. If this po-

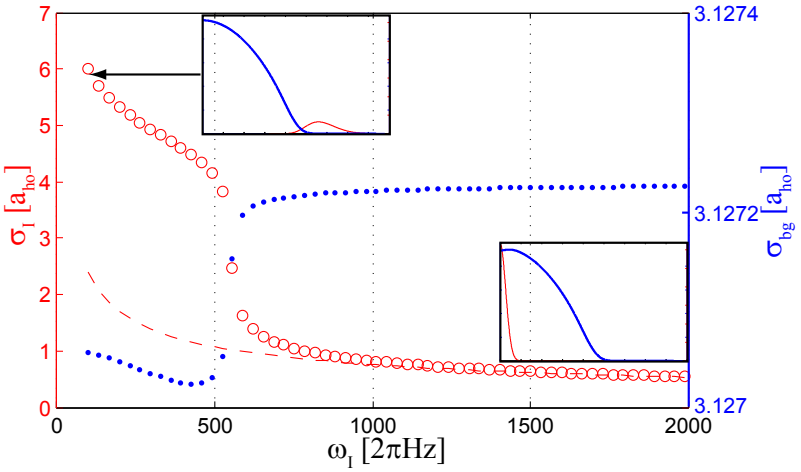

Figure 4.1.: *Real space plot of the localization of the impurity atom (standard deviation of the impurity cloud in red circles) in the background BEC (blue dots) as the impurity trapping frequency ω_I is increased. The width of a bare impurity is shown with the red dashed line for comparison. Note the different scales of the axis. The insets depict the density distribution of the background (blue) and the impurity component (red) at very shallow and at very tight impurity confinement respectively. Calculation parameters are: $N_{bg} = 10^5$, $a_{BB} = 63a_0$, $m_{bg} = 23u$, $\omega_{bg} = 2\pi \times 100Hz$, $N_I = 1$, $a_{IB} = 200a_0$, $m_I = 6u$.*

tential is too shallow, the impurity wavefunction will be separated from the BEC. Fig. 4.1 shows the transition from this phase separated impurity case (at small trapping frequencies) to a localized state within the background gas. The interspecies scattering length $a_{\mathrm{IB}} = 200a_0$ is kept at constant value and only the trapping frequency ω_{I} of the external impurity potential is varied. As can be seen from the plot the width of the impurity wavefunction drops dramatically when reaching higher trapping frequencies, even below the width of the background gas. This corresponds to a localized impurity within the background gas. Another observation is that the width of the background gas stays almost constant (note the different scales for impurity and background components!). However the width of the background wavefunction is a global measure and does not tell something about the local behavior of the background gas on the length scale of the localized impurity wavefunction.

4.1.2. Density Plots

Knowing that a too shallow impurity potential will not localize the impurity atom inside the background BEC we choose $\omega_{\mathrm{I}} = 2\pi \times 2000\mathrm{Hz}$ in the following. The question arising is, how does the presence of the impurity atom affect to the local density of

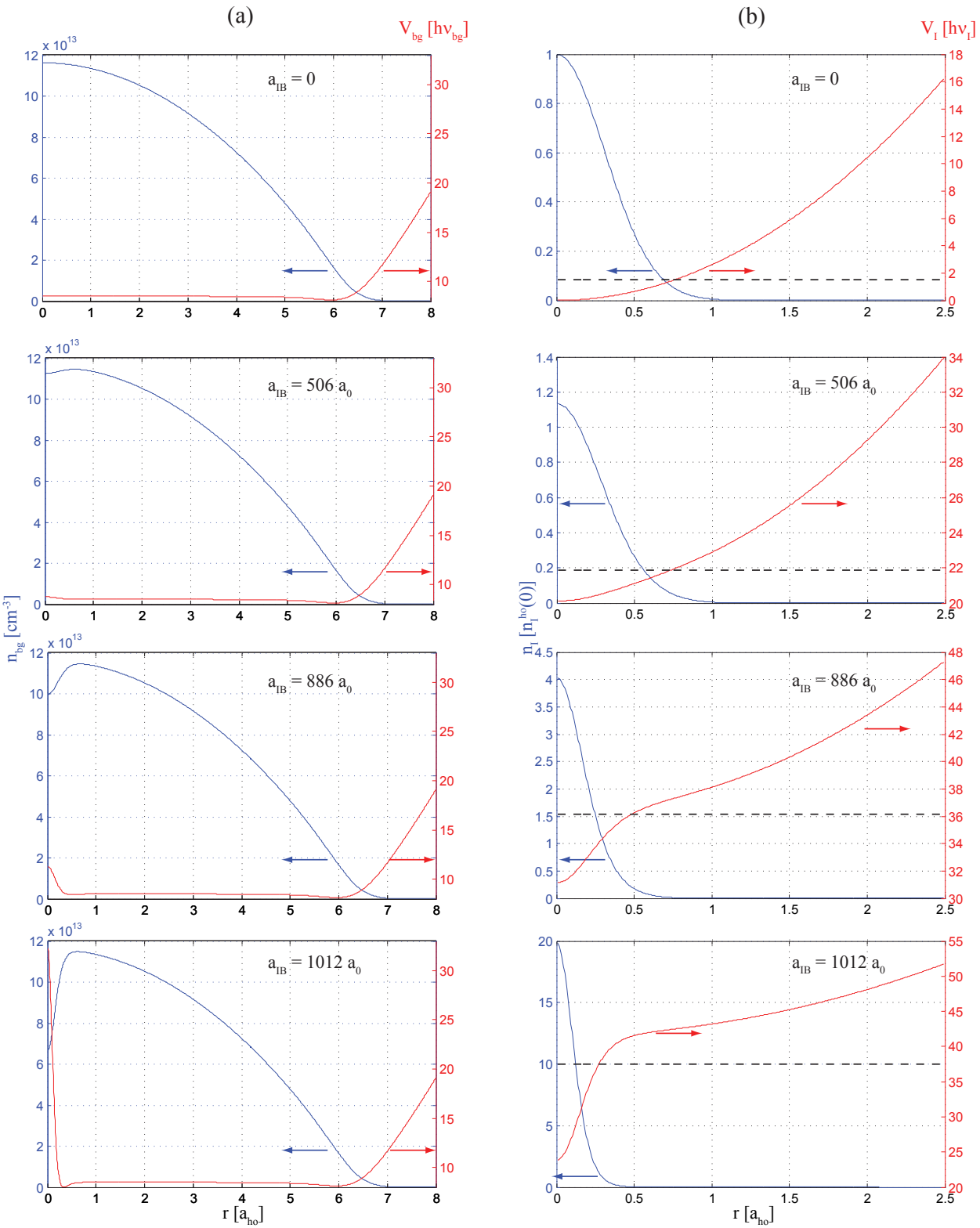

Figure 4.2.: *Density (blue) and effective potential (red) plots of the background BEC (a) and the impurity atom (b) for the denoted interspecies scattering lengths a_{IB}. The background densities are given in atoms/cm^{-3}, the impurity density in units of the peak density of the harmonic oscillator ground state and the effective potentials in $\hbar\omega_I$. The dashed line indicates the chemical potential of the impurity. Calculation parameters are: $N_{bg} = 5 \times 10^5$, $a_{BB} = 63a_0$, $m_{bg} = 23u$, $\omega_{bg} = 2\pi \times 100Hz$, $N_I = 1$, $m_I = 6u$, $\omega_I = 2\pi \times 2000Hz$.*

the background gas? Since only one impurity atom is assumed, no change in the background component is expected as long as the scattering lengths are not tuned away from their background value.

In fig. 4.2 the background (a) and impurity (b) densities as well as the resulting effective potentials according to eq. (3.4) are shown. From the upper to the lower panels the interspecies scattering length a_{IB} is increased as denoted.

For zero interspecies scattering length both – impurity and background atoms – are independent and the background density is characterized by a Thomas-Fermi (TF) profile. This can be seen from the fact that the effective potential is flat in the region where the atoms are. The atoms arrange such that the external potential is balanced by the repulsive intraspecies interaction. Due to a decreasing background density at the outer wings, the TF approximation is no longer fulfilled and the effective potential deviates from the TF prediction which can be seen at the non-flat behavior around $r = 6a_{\mathrm{ho}}$ in fig. 4.2 (a). While increasing the interspecies scattering length this behavior changes only slightly. If a_{IB} is increased further (third plot and fourth plot), the impurity starts to burrow a hole in the background density. In this region the Thomas-Fermi approximation is no longer valid as can be seen from the non-flat effective potential. By increasing a_{IB} further this dip in the background density gets even deeper until no background atoms are present anymore in the vicinity of the impurity atom.

On the right plots of fig. 4.2 the impurity density and effective potential is shown corresponding to the same situation as in (a). The impurity density starts from a harmonic oscillator form at $a_{\mathrm{IB}} = 0$. As a_{IB} is increased the effective impurity potential starts to form a dimple in the center. Note that these calculations are self-consistently solved, thus the dimple gets more and more pronounced and the standard deviation of the impurity wavefunction decreases. In the limit of very large interspecies scattering lengths the impurity is totally bound by its effective potential created by the interaction with the background BEC and no longer by the underlying external potential. This suggests that the sharpening of the impurity density is pronounced as soon as this dimple in the effective potential supports a bound state by its own. The dashed line in fig. 4.2 (b) depicts the chemical potential of the impurity atom. As can be seen from the plots, the chemical potential is below the shallow external confinement for large a_{IB}, but inside the emerging dimple potential. A bound state can be supported by the emerging dimple potential and the impurity is trapped therein and no longer by the external potential.

In order to investigate this behavior further, the depth of this dimple potential (inset of fig. 4.3) and the chemical potential of the impurity atom, plotted versus the interparticle scattering length a_{IB} is shown in fig. 4.3. At small scattering lengths the dimple is not present and emerges only slowly as a_{IB} increases. Also the chemical potential increases linear with the scattering length. This behavior is consistent with a first order pertubation theory, where $E \propto a_{\mathrm{IB}} n_{\mathrm{bg}}(0)$ is expected for the energy of the system. As a_{IB} approaches large values the slope of the chemical potential is kinked—the impurity atom perceives another potential. At this kink the dimple depth increases rapidly. The impurity potential is now very sensitive to slight changes in the

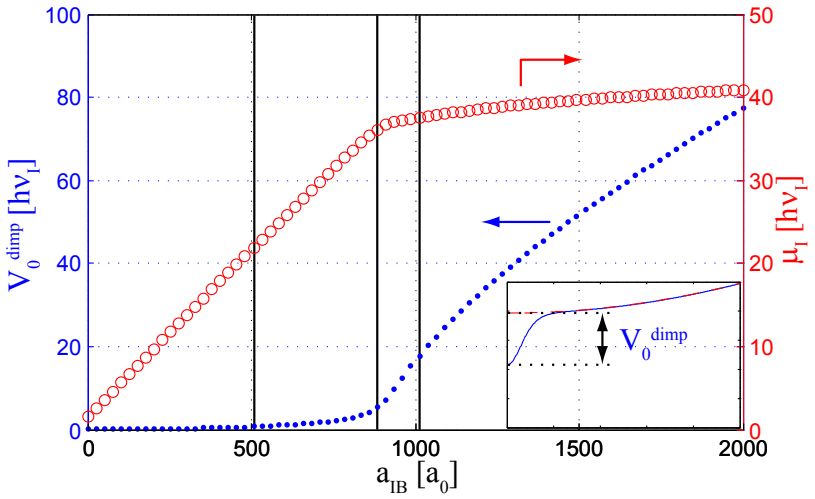

Figure 4.3.: *(a): Depth of the emerging dimple (blue dots) in the impurity potential V_0^{dimp} and (b) the chemical potential (red circles) of the impurity atom μ_I. The vertical lines mark the points were the density profiles are shown in fig. 4.2. The inset depicts the dimple depth V_0^{dimp} being the deviation of the impurity potential due to the interparticle interaction compared to the $a_{IB} = 0$ case. Calculation parameters are: $N_{bg} = 5 \times 10^5$, $a_{BB} = 63a_0$, $m_{bg} = 23u$, $\omega_{bg} = 2\pi \times 100Hz$, $N_I = 1$, $m_I = 6u$, $\omega_I = 2\pi \times 2000Hz$.*

interparticle scattering length and mainly consists of the self-burrowed potential in the background atoms. The clearly different slope of the chemical potential can be interpreted such that no longer the external potential confines the atom but rather the self-consistent potential arising from the interaction with the background atoms. In this potential the effective mass of the impurity will be different from the bare mass as will be shown later in this chapter.

4.1.3. The Coupling Parameter

In order to compare numerical results using different peak densities of the background gas, we recall the polaron coupling parameter eq. (2.36), mapped to cold atomic gas systems:

$$\alpha = \frac{a_{\mathrm{IB}}^2}{a_{\mathrm{BB}}\xi} \tag{4.1}$$

Assuming a peak density of the background ^{23}Na atoms of $1 \times 10^{14}\mathrm{cm}^{-3}$ and taking the scattering lengths at zero magnetic field $a_{\text{Na-Na}} = 63a_0$ and $a_{\text{Li-Na}} = 14a_0$, the coupling constant is on the order of $\alpha = 4 \times 10^{-4}$.

	entrance channels $\|\alpha,\beta\rangle$	B_0 [G]	ΔB [G]	a_{bg} $[a_0]$	Reference
^{6}Li-^{23}Na	$\|1,1\rangle$	0		14	[55]
	$\|1,1\rangle$	795.6	2.1	13	[55, 11]
	$\|1,1\rangle$	1185.7	8.7	12.67	[55]
^{23}Na-^{23}Na	$\|3,3\rangle$	0		53	[56]
	$\|8,8\rangle$	0		63	[56]
	$\|1,1\rangle$	907	1	63	[10]
	$\|3,3\rangle$	1195	-4	63	[57]

Table 4.1.: *Interspecies and intraspecies Feshbach resonances of the ^{6}Li-^{23}Na mixture which might be of interest for the experimental tackling of the polaron problem. The numbering of the entrance channels of the atoms is determined by the increasing order of energy at large magnetic fields, where the hyperfine states are dressed by the magnetic field. For ^{6}Li $\alpha = 1 \dots 6$ and for ^{23}Na $\alpha = 1 \dots 8$ in increasing order of energy, see appendix A.*

In order to vary the coupling strength of the polaron, there are two possibilities: (i) vary the interspecies scattering length a_{IB}, which goes quadratically into the coupling strength. (ii) decrease the intraspecies scattering length of the background component a_{BB}. For both scenarios Feshbach ressonances are available and listed together with the zero magnetic field parameters in table 4.1. The initial states of the collisions are labeled by the initial Zeeman states of the atom. For a Breit-Rabi diagram of the states with the labeling the reader is referred to the appendix A.

Ultimately, the limiting factor in both scenarios to increase α is the magnetic field stability in the experiment. A detailed analysis can be found in [58]. Due to the width of the ^{23}Na-^{23}Na resonance, the minimum achievable background scattering length is on the order of $a_{\mathrm{BB}} \approx 0.3a_0$ at a magnetic field stability of $\delta B/B = 10^{-5}$ which limits the coupling constant on the order of $\alpha \approx 10^{-2}$. On the other hand, using the relatively broad ^{6}Li-^{23}Na resonance at 1186G, the interspecies scattering length can be tuned to $a_{\mathrm{IB}} \approx 1000a_0$ which translates to $\alpha \approx 2.3$. As will be shown in the following this coupling will be sufficient to reach the strong coupling limit, which favors this resonance to be used in the experiment.

But how do we know from the numerical results that the impurity atom is in the strong coupling regime?

In condensed matter theory, strong coupling refers to an electron localized to one lattice ion. In this regime, the polaron can be viewed as an electron with a phonon cloud attached to it. To translate this picture into the ultracold atom framework, the Bogoliubov excitations are attached to the immersed impurity atom. Due to the strong coupling of the impurity atom to the background gas and therewith to its Bogoliubov excitations, the background density is strongly disturbed at the position

of the impurity. The emerging dimple is analogue to a wavepacket in optics, where the wavepacket forms by coherently adding many plane waves with different wavevectors k as shown in fig. 4.4.

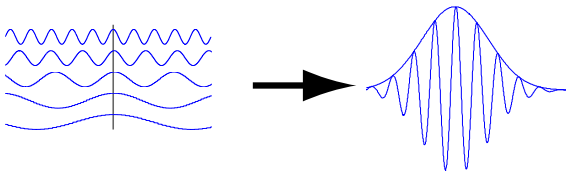

Figure 4.4.: *Emerging wavepacket when coherently adding up plane waves.*

4.1.4. Central Density

From this mapping, one would expect a strong, localized disturbance of the background component as soon as the impurity is coupled strongly to the background—α is in the strong coupling regime. Therefore we refer to strong coupling once the dimple depth – as shown in fig. 4.3 – of the effective impurity potential changes dramatically while varying the coupling parameter.

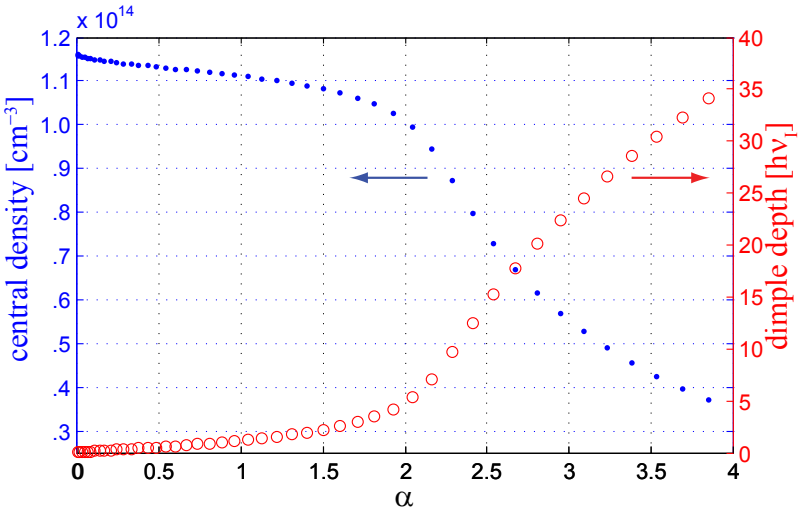

Figure 4.5.: *(a): central density of the background BEC vs. coupling parameter α. (b): emerging depth of the dimple in the impurity potential. Calculation parameters are:* $N_{bg} = 5 \times 10^5$, $a_{BB} = 63a_0$, $m_{bg} = 23u$, $\omega_{bg} = 2\pi \times 100Hz$, $N_I = 1$, $m_I = 6u$, $\omega_I = 2\pi \times 2000Hz$.

This behavior can nicely be seen in fig. 4.5, where the central density of the background component and the depth of the emerging dimple in the effective impurity

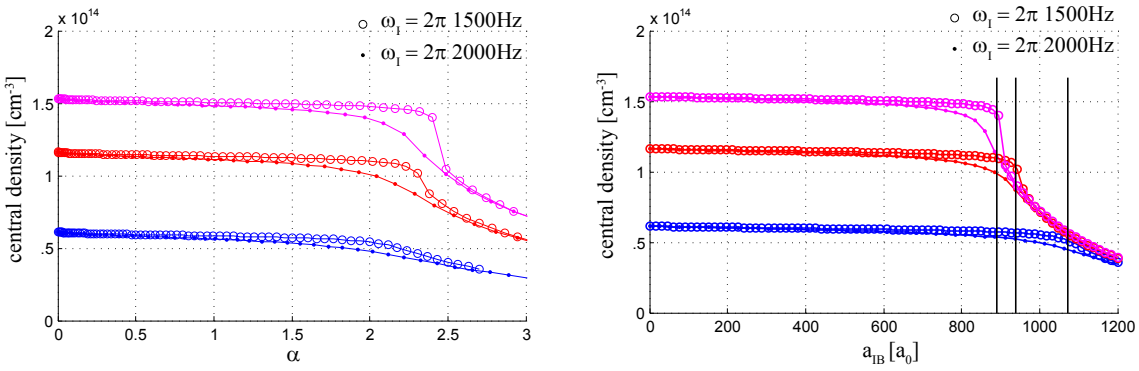

(a) **(b)**

Figure 4.6.: *Central density of the background BEC vs. (a): coupling parameter α and (b): interspecies scattering length a_{IB} for different external impurity potentials as indicated. Vertical lines indicate the interspecies scattering length a_{IB} where the impurity enters the strong coupling regime for different background densities n_B. Calculation parameters are: $a_{BB} = 63a_0$, $m_{bg} = 23u$, $\omega_{bg} = 2\pi \times 100Hz$, $N_I = 1$, $m_I = 6u$. The atom number of the background BEC has been varied to obtain results for different densities.*

potential is plotted versus α. The system is in the strong coupling regime as α exceeds a critical value of $\alpha_{\text{crit}} \approx 2.0 - 2.5$.

4.1.5. Influence of the Impurity Potential

The differences to the results obtained by Tempere *et. al.* [42] are that they used a homogenous background and no external impurity potential. In contrast we need to assume a non-vanishing external impurity and background potential during the calculations to obtain results to experimentally observable scenarios. Hence the question arises, to what extend this trapping potential influences the behavior of the impurity atom.

To study this question further, the central density of the BEC was calculated for two different external impurity potentials as can be seen from fig. 4.6. The different colors correspond to different atom numbers of the background BEC and consequently to different background densities.

There are different features apparent from the plot: (i) A tight external trapping potential of the impurity atom smoothens the crossing from the impurity being trapped mainly due to the external potential, to a trapping due to a self-buried impurity potential induced by the interaction with the background BEC.

(ii) As soon as the impurity is self-trapped by its interaction, the external impurity potential has no influence anymore on the central density. This could already have been guessed by the chemical potential as plotted in fig. 4.3. As long as the trapping of

the impurity atom is determined by the external trap, the chemical potential depends linearly on the interspecies interaction with the background. Once the impurity is self-trapped, the increase in the interaction energy is compensated by a deeper self-buried impurity potential—the chemical potential is nearly independent of the interaction and alike the central background density is independent of the external impurity potential.

Moreover, as indicated by the vertical lines in fig. 4.6 (b) it can be seen, that the kink in the central density of the background component occurs at lower a_{IB} for higher background densities n_{B}. The impurity reaches the strong coupling regime at lower interspecies scattering lengths the larger the background density n_{B} is. Once the impurity is self-trapped, the central density drops to the same value, independent of the initial particle density of the background BEC. This density drop to the same value is what one would have expected, as the interspecies interaction scales as $\propto a_{\mathrm{IB}} n_{\mathrm{B}}$ as can be seen from eq. (3.1).

The fact that at larger densities, the drop in the central density occurs at smaller a_{IB} but larger α is due to the fact that $\alpha = a_{\mathrm{IB}}^2/a_{\mathrm{BB}}\xi \propto \sqrt{n_{\mathrm{B}}}$. The critical α_{crit} for the strong coupling regime has a weak scaling with the background density [59].

4.1.6. Effective Mass Computation

An important quantity that was calculated by Tempere *et al.* is the effective mass of the impurity atom. This quantity can also be measured in experiments in a very direct way by exciting dipole oscillations of the impurity atom and measuring the resulting oscillation frequency of the center of mass motion. Knowing the external trapping frequency allows to attribute a deviating oscillation frequency to a modified particle mass—the effective mass of the impurity.

However, extracting the effective mass from the spherically symmetric calculations is not straight forward. Here the rms-width of the impurity wavefunction is used to determine the mass as already described in the methods section in eq. 3.10.

Fig. 4.7 shows the effective mass m_{eff} (in units of the bare impurity mass m_{Li}) of an impurity atom immersed in a background BEC of sodium atoms of different densities. It shows a strong increase of the effective impurity mass, as soon as the impurity is self-trapped by the interaction. The impurity atom gets localized in the self-buried dimple potential as was already indicated by the chemical potential plot in fig. 4.2 and fig. 4.3 and the drop of the central background density fig. 4.5.

By comparing figs. 4.7 (a) and (b) it can be seen that the interparticle scattering length a_{IB} is not the right parameter to characterize the interaction strength of the impurity atom to the background component. The kink in the effective mass of the impurity atom occurs at different a_{IB} for different atom numbers of the background gas. Those different atom numbers correspond to different peak densities and thereby to different healing lengths of the background gas. If the effective mass is plotted against the coupling parameter α, the position of the kink for different atom numbers coincide. As α is increased further, the impurity gets localized into the background component. At very large α, this localization length is even below the healing length of the background gas. Here the applied mean-field description is no longer valid,

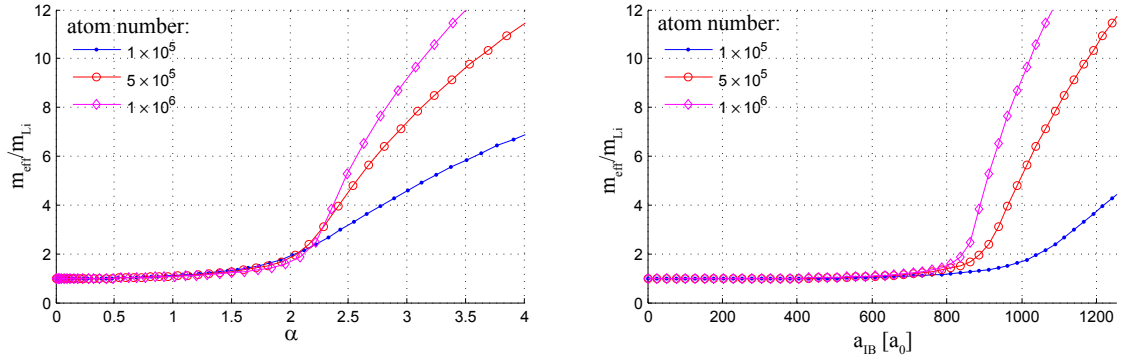

(a) **(b)**

Figure 4.7.: *Effective mass of the impurity atom in units of the bare impurity mass, immersed in a background BEC vs. (a) the coupling parameter α and (b) vs. the interparticle scattering length a_{IB}. The different colors refer to different densities of the background BEC, resulting from different atom numbers used in the calculation as denoted in the inset. $a_{BB} = 63a_0$, $m_{bg} = 23u$, $\omega_{bg} = 2\pi \times 100Hz$, $N_I = 1$, $m_I = 6u$, $\omega_I = 2\pi \times 2000Hz$.*

which explains the deviation of the effective mass plots for different atom numbers at large α.

A similar behavior of the effective mass of the impurity atom was predicted by Tempere *et. al.* (fig. 2.3 in section 2.3.1), but there the strong mass increase was due to a coupling of the impurity to Bogoliubov excitations of the background condensate. There is no requirement that the condensate density needs to be depleted strongly to provide an increase of the effective impurity mass [59]. A coupling to the Bogoliubov modes up to the inverted healing length already sufficed.

In the mean-field picture applied here to the problem, excitations of the condensate (i.e. Bogoliubov excitations) are neglected. A constant background density over the range of the impurity would lead to a constant energy offset of the GPE and therefore no increase of the effective mass is expected. However, the mean-field theory predicts a localization and consequently an increase of the effective mass of the impurity atoms, although the physical reason is different. Within the mean-field picture, the impurity localizes into the background BEC due to a strong interaction. It is energetically favorable for the impurity to deplete the background BEC up to the point where this self-buried dimple potential is deep enough to support a bound state. At this point, the impurity is no longer trapped by its external potential, but rather by the interaction – although repulsive – with the background.

The critical coupling parameter α_{crit} where the impurity is coupled strongly to the background gas differs between both methods, the Feynman path integral approach and the mean-field ansatz used here. Tempere *et al.* estimate $\alpha_{\text{crit}} = 3$, whereas

the mean-field picture suggests $\alpha_{\mathrm{crit}} \approx 2$. Beyond this critical coupling strength, the effective mass of the impurity increases faster. However at very large coupling strengths, the mean-field description is not applicable, since the impurity gets localized on a length scale smaller than the healing length. Here the estimation of the effective mass of the impurity fails.

4.1.7. Which is the Better Impurity: Na or Li?

Here we want to answer the question what happens if we would invert the mass ratio of the impurity and background atoms and use a sodium impurity in the vicinity of a background of bosonic ^{7}Li atoms. How is the transition from a quasi-free impurity atom to a self-trapped impurity influenced by this mass change?

With the use of fermionic ^{6}Li the background would be a degenerate Fermi gas and the mean-field methods applied here to calculate the background-impurity scattering would fail. This scenario of a ^{23}Na impurity immersed in a background BEC of ^{7}Li would be possible to realize in the experiments, although some complications would arise. First, ^{7}Li has a negative s-wave scattering length at zero magnetic field, which limits the number of ^{7}Li atoms that can be brought into quantum degeneracy. A possible cooling scheme would be: load the lithium atoms from the MOT into a magnetic trap with sodium atoms and evaporate the sodium. Lithium would still be cooled sympathetically and the process can be stopped before all the sodium is removed from the trap. After loading the sample into an optical dipole trap the intraspecies scattering length of lithium can be tuned to positive values. In this way sodium could serve as the impurity component. The question is, if the self-trapping of the impurity atoms can be reached at lower interspecies scattering lengths, which would loosen the requirements on the magnetic field stability in order to reach the strong coupling limit.

In fig. 4.8 the situation of a ^{6}Li impurity immersed in a background BEC of ^{23}Na and a ^{23}Na impurity immersed in a background BEC of ^{7}Li atoms are compared to each other. The intraspecies scattering length of the background component is fixed to $63a_0$ and only the interspecies scattering length is varied. In this way the difference between both situations is a pure effect of the inverted mass ratio. The critical value of the interparticle scattering length a_{IB} at which the central density of the background density drops, changes only slightly between both scenarios. However the central density drop is more pronounced when using ^{6}Li as the impurity. This behavior can be explained, since the coupling strength due to the intraspecies interaction scales inversely to the particle mass according to the GPE, eq. (2.13), whereas the interspecies coupling strength scales inversely to the reduced mass that remains unchanged. In the case of a light impurity immersed in a heavier background gas, this scaling favors the interparticle interaction compared to the intraparticle one. Once the interparticle interaction has overcome the trapping by the external potential, the impurtity atom is self-trapped and only the intraparticle interaction in the background gas hinders the background density to drop to zero immediately, favoring a light impurity immersed into a heavy background gas.

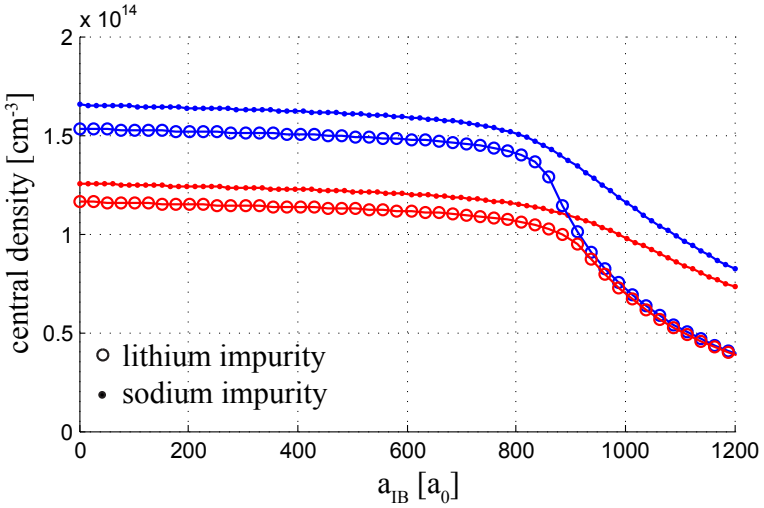

Figure 4.8.: *Comparison of the influence of the impurity mass on the behavior of the background component. As indicated, the circles correspond to a ^{6}Li impurity immersed in a ^{23}Na background and the dots to a ^{23}Na impurity in a ^{7}Li background. The colors indicate different initial densities. The calculation parameters are $a_{BB} = 63a_0$, $\omega_{bg} = 2\pi \times 100Hz$, $N_I = 1$, $\omega_I = 2\pi \times 2000Hz$.*

4.2. Many Impurity Case

Up to here we always discussed a single impurity atom immersed in a background BEC. This situation is in close analogy to the condensed matter polaron. In the cold gases context, one impurity atom interacts with the Bogoliubov modes of the background BEC and thus gets self-trapped in the background. In contrast, if we consider many impurities being trapped in a background gas, these cannot obviously be considered as single particles forming many polarons. A bosonic impurity gas will rather form a BEC and this BEC will interact with the background as a whole.

In order to study the case of many bosonic impurities in the following, we will consider a background BEC of $N_\mathrm{B} = 1 \times 10^6$ ^{23}Na atoms being confined in an external, spherically symmetric trap with $\omega_\mathrm{bg} = 2\pi \times 100\mathrm{Hz}$. A second harmonic trap, exclusively for the impurity atoms is overlapped such that their trap centers merge. $N_\mathrm{I} = 1\times10^3$ ^{7}Li impurity atoms are confined with a trap frequency of $\omega_I = 2\pi\times350\mathrm{Hz}$. Note that the impurity species is changed to bosonic ^{7}Li here in order to apply the mean-field methods, since this mean-field description fails for an impurity gas of many fermionic ^{6}Li atoms.

In fig. 4.9 the central density of the background and the impurity gases are plotted as the interparticle scattering length is increased. The rapid fall off of the central density at $a_\mathrm{IB} \approx 45a_0$ corresponds to the phase separation of impurity and background gases: At lower interparticle scattering length, both components coexist in the same region

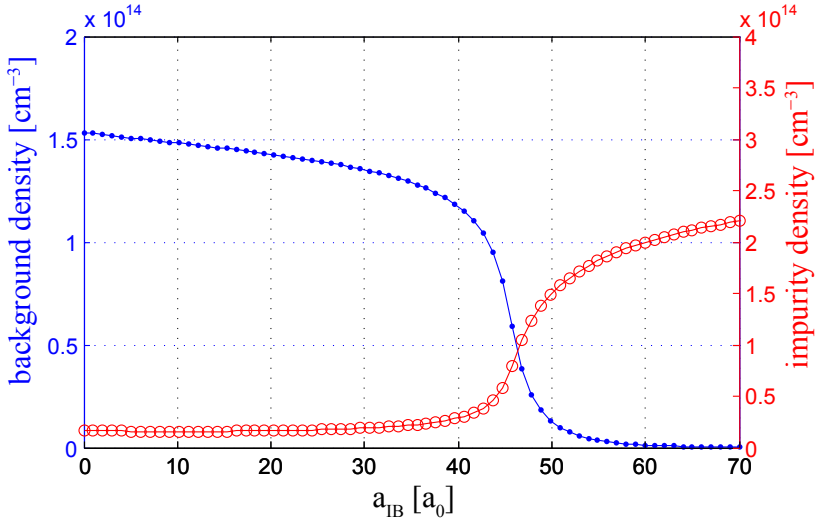

Figure 4.9.: *Central density of the background (blue dots) and impurity (red circles) components vs. interparticle scattering length between impurity and background atoms. The calculation parameters are* $N_{bg} = 1 \times 10^6$, $a_{BB} = 63a_0$, $\omega_{bg} = 2\pi \times 100Hz$, $N_I = 1 \times 10^3$, $a_{II} = 14a_0$, $\omega_I = 2\pi \times 350Hz$.

of space. Above the critical interparticle scattering length, the background is pushed away from the trap center, forming a sphere around the minority atoms. The critical interparticle scattering length for this process to happen, depends on the number of atoms in both components, background and impurities, which has already been studied in detail [53]. As already discussed in subsection 4.1.5 for a single impurity, a tighter external confinement of the impurity gas would smoothen the crossing from the mixed to the phase-separated state.

But what makes the difference between the single impurity on the one hand and the many impurity BEC on the other? In both cases the central background density drops as soon as some critical interparticle interaction strength is reached. At this point the strong interaction between the impurity and the background component pushes the background gas out of the center of the trap, where the impurities are located. In the many impurity limit, this process is referred to as phase-separation. Both components segregate until two pure single component phases coexist in the trap, separated by a small overlap region as described above.

In contrast, as the interparticle interaction is increased in the single impurity limit, the impurity gets self-trapped by its interaction with the background BEC. This process can be viewed as a strong interaction of a single particle with the Bogoliubov modes of the background component. Adding many of these excitations in a coherent manner can explain the dip in the background density. As the interparticle interaction strength is increased, more Bogoliubov modes are excited and the localization

gets more pronounced until the impurity atom is self-trapped within the background. This process is in close analogy to the polaron concept, known from condensed matter. Here a single electron interacts with the lattice excitations and can get localized to a single lattice site, if the electron-phonon interaction is strong enough.

The difficulty is now the correct expansion of the single impurity polaron picture to the case when more than one impurity is considered. If we assume two or three impurity atoms to be confined in the background gas, their intraparticle interaction has to be taken into account correctly. At this point there should be a fundamental difference between bosonic and fermionic impurities. This cannot be done using this simple mean-field ansatz employed in this work. Will those few impurity atoms form single polarons that interact with each other? If they do so, which parameters affect the crossing to a simple phase-separation as in the many impurity case? What is the correct mapping of the few impurity limit to the single impurity and therewith the polaron physics? What determines the interaction properties of those few polarons besides the Bose or Fermi statistics?

Part II.

Bose-Einstein Condensation of Sodium

In this part of the thesis the experimental setup, built to study immersed systems as discussed in the first part, is explained. The experiment started at the beginning of 2007 with an empty lab. Using sodium and lithium as the elements to work with seemed a good idea, since the largest degenerate Fermi gases reported so far was produced in the MIT group of W. Ketterle, working with this combination. Cooling a gas of fermionic ^{6}Li atoms into quantum degeneracy can be done in different ways, however producing large degenerate fermionic samples forbids to evaporate ^{6}Li directly during the evaporation process. The advantage of sodium as a refrigerant in during evaporation is, that large sodium BECs can be produced. ^{6}Li is only cooled sympathetically and we aimed for a large degenerate Fermi gas, too. We started to build the experiment from scratch, using a plugged quadrupole configuration which be explained in more detail in the following chapter. This lead to the Bose-Einstein condensation of sodium in the $|F = 1, m_F = -1\rangle$ state in the end of the year 2008. However, the atom number was not as high as expected. While trying to tackle this problem, a failure of the cooling device of the magnetic coils broke the vacuum and the coil setup.
We started in May 2009 with a complete re-design of the experimental setup, straightening out some of the drawbacks of the old design. The first MOT with the new setup was achieved in January 2010 and the first BEC of sodium in the $|F = 2, m_F = 2\rangle$ state was produced in March 2010.

5. Trapping and Investigation of Cold, Neutral Atoms

In this chapter, the reader will be introduced to the basic techniques used to trap neutral atoms. The potential induced by a laser field will be discussed and the effect of an external magnetic field on neutral atoms will be reviewed. At the final stage of the experiment the atoms will be transferred into an optical dipole potential in order to use the magnetic field to tune the interaction properties via the use of a Feshbach resonance. Also the plugged quadrupole trap configuration uses an optical potential as will be explained in more detail. At the end of the chapter, the two magnetic trap configurations used in the experiment—the plugged quadrupole trap and the cloverleaf trap will be compared to each other.

5.1. Optical Dipole Traps

In general, two types of forces can be distinguished for an atom interacting with a light field.

(i) The dissipative force, occurring if an atom absorbs a photon from the beam and reemits it afterwards spontaneously. Since the direction of the spontaneous emission process is equally distributed among all directions of space, whereas the absorption is directed, this process can be used to cool the atoms [60].

(ii) The dipole force [61], caused by the interaction with a laser field. Due to the polarizability α of the atoms, the electric field $\vec{E}(\vec{r},t)$ of the laser beam induces an electric dipole moment $\vec{p}(\vec{r},t)$, oscillating at the driving laser frequency ω_{L}.

$$\vec{p}(\vec{r},t) = \alpha\vec{E}(\vec{r},t) \tag{5.1}$$

Averaging over the fast oscillating terms of the laser field, the induced dipole potential reads:

$$V_{\mathrm{dip}} = -\frac{1}{2}\left\langle \vec{p}\vec{E} \right\rangle_t = \frac{1}{2\epsilon_0 c}\Re(\alpha)I \tag{5.2}$$

where the intensity of the electric field $I = 2\epsilon_0 c|\vec{E}|^2$ has been introduced. The factor $1/2$ is due to the fact that the dipole moment is an induced one, ϵ_0 denotes the vacuum dielectric constant and c the speed of light. The imaginary part of the polarizability is connected to the off-resonant scattering rate Γ_{sc} as follows:

$$\Gamma_{\mathrm{sc}} = \frac{1}{\hbar\epsilon_0 c}\Im(\alpha)I. \tag{5.3}$$

The polarizability α can be calculated from a classical oscillator model of an electron driven by an external electric field. The frequency of the driving field corresponds to the laser frequency ω_{L} and the eigenfrequency of the electron to the atomic transition frequencies ω_0. The polarizability reads [61]:

$$\alpha = 6\pi\epsilon_0 c^3 \frac{\Gamma/\omega_0^2}{\omega_0^2 - \omega_{\mathrm{L}}^2 - i\Gamma\omega_{\mathrm{L}}^3/\omega_0^2}. \tag{5.4}$$

This classical approximation is in good agreement with the quantum mechanical calculation of an two level atom interacting with a radiation field, as long as saturation effects of the transition can be neglected and the scattering rate Γ_{sc} is small compared to the natural linewidth Γ.

Using the equations introduced above, the dipole potential and the scattering rate read:

$$V_{\mathrm{dip}}(r) = -\frac{3\pi c^2}{2\omega_0^3}\left(\frac{\Gamma}{\omega_0 - \omega_{\mathrm{L}}} + \frac{\Gamma}{\omega_0 + \omega_{\mathrm{L}}}\right) I(r) \tag{5.5}$$

$$\Gamma_{\mathrm{sc}}(r) = \frac{3\pi c^2}{2\omega_0^3}\left(\frac{\omega_{\mathrm{L}}}{\omega_0}\right)^3 \left(\frac{\Gamma}{\omega_0 - \omega_{\mathrm{L}}} + \frac{\Gamma}{\omega_0 + \omega_{\mathrm{L}}}\right)^2 I(r). \tag{5.6}$$

In the case of detunings $\Delta = \omega_{\mathrm{L}} - \omega_0$ fulfilling $|\Delta| \ll \omega_0$, the second term in equations (5.5) and (5.6) can be neglected and the relations hold:

$$V_{\mathrm{dip}}(r) \propto \frac{\Gamma}{\Delta} I(r) \tag{5.7}$$

$$\Gamma_{\mathrm{sc}}(r) \propto \left(\frac{\Gamma}{\Delta}\right)^2 I(r) \propto \frac{\Gamma}{\Delta} V_{\mathrm{dip}}(r). \tag{5.8}$$

If the laser frequency is below the atomic transition frequency (i.e. red-detuned, $\Delta < 0$), the dipole interaction is attractive, such that atoms are attracted to the maxima of the laser field. In the opposite case of blue detuning ($\Delta > 0$), the dipole interaction repels the atoms from the laser field.

Since the scattering of photons leads to heating of the confined atoms cloud, it is favorable to use large detunings and high intensities to obtain a certain trap depth in order to minimize the heating rate.

5.2. Magnetic Trapping

Another way of trapping atoms is to use the response of their permanent magnetic moment μ_{m} to an external magnetic field. The applied external magnetic field modifies

the energy spectrum of the atoms, and depending on the field strength different regimes (Zeeman, Paschen-Back) can be reached [26, 62].

Alkali atoms have a hydrogen like structure with one electron in the outer shell which carries a spin $\vec{S}$. Its movement around the atom can be described by an orbital angular momentum $\vec{L}$, and the nucleus carries a spin momentum $\vec{I}$. All of these quantities give rise to magnetic moments, which can couple to each other and to an external magnetic field.

In our experiment, the external field is not large enough to lift the coupling of the electron spin $\vec{S}$ to the angular momentum $\vec{L}$, such that the total electron angular momentum $\vec{J}$ is always a good quantum number, which gives rise to the atoms finestructure:

$$\vec{J} = \vec{L} + \vec{S}. \tag{5.9}$$

If no external magnetic field is present, the nucleus spin momentum $\vec{I}$ couples to the total electron angular momentum $\vec{J}$. This coupling reveals the hyperfine structure and causes the total angular momentum $\vec{F}$ to be a good quantum number:

$$\vec{F} = \vec{J} + \vec{I}. \tag{5.10}$$

If the energy shift of the atomic levels in an external magnetic field B is small compared to the hyperfine splitting, then $\vec{F}$ is a good quantum number and the energy correction to the undisturbed atomic levels is:

$$\Delta E_{\text{Zeeman}} = \mu_{\text{B}} g_F m_F B_z. \tag{5.11}$$

The magnetic field was chosen to point along the z-direction and μ_{B} is Bohr's magneton. m_F and g_F are the z-component of the total angular momentum and the hyperfine-Landé factor respectively. This splitting is called the anomalous Zeeman effect.

For strong fields, the energy shift due to the external field dominates the hyperfine splitting and $\vec{F}$ is no good quantum number anymore. This regime is called the Paschen-Back effect of the hyperfine structure. The hyperfine interaction is now only a pertubation to the energy levels, which split according to the $\vec{J}$ and $\vec{I}$ quantum numbers separately.

For ^{23}Na, the crossover between those two regimes is in the range of 300G, meaning that $\vec{F}$ is a good quantum number when working with magnetic traps, whereas for ^{6}Li the crossover is already at 27G.

Magnetic Potential

The magnetic potential of an atom in an external magnetic field reads:

$$V_{\text{m}}(r) = -\mu_{\text{m}} B(r) \tag{5.12}$$

where $\mu_\mathrm{m} = m_F g_F \mu_\mathrm{B}$. Depending on the sign of the magnetic moment the atoms will be in a potential minimum (maximum) when being located at the minimum (maximum) of the magnetic field $B(r)$, and are thus called low (high) field seekers. Since the Maxwell equations forbid a maximum of the magnetic field in free space (i.e. without a source at this point), the trappable states of an atom reduce to the low field seeking ones, which are the $|F = 1, m_F = -1\rangle$ and $|F = 2, m_F = 2, 1, 0\rangle$ states for ^{23}Na in the $3^2\mathrm{S}_{1/2}$ ground state.

In the ultracold atom community different trapping geometries are commonly used. A straightforward way to create a magnetic field minimum is to use a set of coils in anti-Helmholtz configuration. The magnetic field created there is linear around the trap center and reads $|B(\rho, z)| = B'\sqrt{\rho^2 + (2z)^2}$ where B' is the field gradient along the weak axis and cylindrical coordinates have been used.

However, at $(\rho, z) = (0, 0)$ the magnetic field vanishes, which is a problem for cold atoms. The reason is the following: In eq. (5.12) it is assumed that the magnetic moment of the atom is always aligned to the direction of the external magnetic field. Only in this case eq. (5.12) is a scalar equation. This requirement is very well fulfilled as long as the Larmor frequency $\omega_\mathrm{L} = \mu_\mathrm{m}|B|/\hbar$ is much larger than the trapping frequency ω of the atom. Close to the trap center the magnetic field is very small resulting in a very small Larmor frequency. As the atom passes the zero crossing of the magnetic field, the magnetic moment cannot realign to the new direction of the magnetic field. The quantization axis can flip with respect to the magnetic moment and the atom is in an untrapped (high field seeking) state, thus getting lost from the trap. This loss mechanism is called Majorana loss. More details can be found in [63, 64].

There are several modifications of the quadrupole trap that avoid this problem. One possibility is to add a fast rotating bias field to the quadrupole trap. The rotation frequency of this field ω_TOP must be large enough to create a time-averaged potential, but smaller than the Larmor frequency ω_L, such that the atoms magnetic moment can follow the rotation of the external magnetic field, i.e. $\omega \ll \omega_\mathrm{TOP} \ll \omega_\mathrm{L}$ with the trapping frequency ω . A time-orbiting potential (TOP) [65] is created where the atom only sees a mean potential of harmonic form with a finite magnetic field offset. The magnetic field zero rotates around the trap center with a frequency ω_TOP. High energetic atoms can still reach this potential surface and get expelled from the trap. The rotating magnetic field forms a ring of zero magnetic field which is called the circle-of-death. In order to reduce the trap depth and cool the atoms by forced evaporation the amplitude of the rotating bias field and therewith the radius of the circle-of-death is reduced.

5.2.1. Plugged Quadrupole Trap

A third possibility to prevent Majorana losses is to overlap a blue detuned (i.e. repulsive) dipole potential with the magnetic field zero, thus forming a hybrid trap. This plugged quadrupole configuration was used in the original design of our apparatus. The resulting potential is the sum of the magnetic quadrupole potential V_m and the

dipole potential V_{dip}.

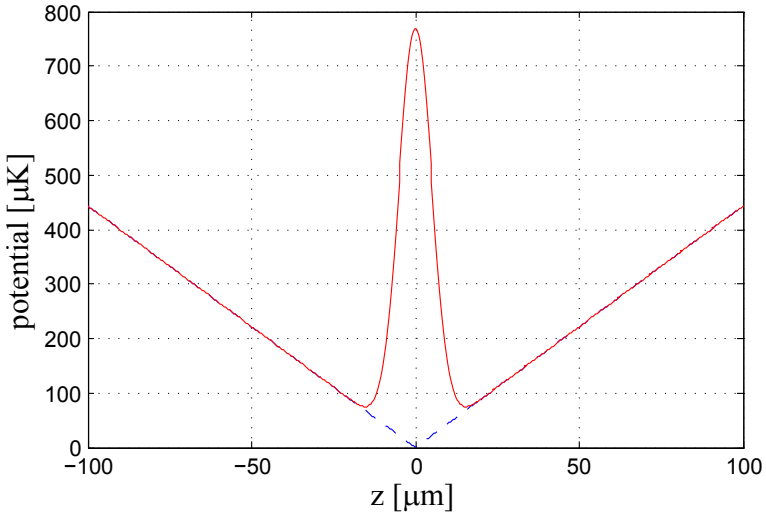

Figure 5.1.: *Combined Plug potential (red) along the strong axis of the quadrupole field, assuming* $B' = 660\mathrm{G/cm}$, $w_0 = 10\mu\mathrm{m}$, $P_0 = 1\mathrm{W}$. *The blue dashed line is the magnetic potential only.*

In our configuration, we used a power of $P_0 = 1\mathrm{W}$ taken from the pumping laser at a wavelength of $\lambda = 515\mathrm{nm}$, coupled into an optical single mode fiber. The beam was focused onto the magnetic field zero with a waist of $w_0 = 10\mu\mathrm{m}$ using a 120mm achromatic lens. The resulting potential along the symmetry axis of the quadrupole trap is plotted in fig. 5.1 assuming a maximum achievable field gradient of $B' = 660\mathrm{G/cm}$. The potential is only modified at the center of the trap, where the plug beam is focused onto. The strong axis of the quadrupole field is directed along the z-axis, and the plug beam is focussed along the y-axis.

Around the bottom of the trap, the potential can be approximated by a harmonic oscillator potential, revealing the trapping frequencies [1]:

$$\omega_x = \omega_y \sqrt{\left(\frac{4x_0^2}{w_0^2}\right) - 1} \tag{5.13a}$$

$$\omega_y = \sqrt{\frac{m_F g_F \mu_{\mathrm{B}} B'}{2 m x_0}} \tag{5.13b}$$

$$\omega_z = \sqrt{3}\omega_y. \tag{5.13c}$$

In this notation, x_0 is the displacement of the potential minimum from the center of the magnetic field minimum. For our trapping geometry, these trapping frequencies are in the range of 1kHz.

In our experiment for sodium atoms in the $|F = 1, m_F = -1\rangle$ hyperfine state, a plug power of $P_0 = 1$W sufficed to suppress Majorana losses. However for lithium atoms the detuning of the plug laser is larger, such that the plug potential for sodium atoms is approximately a factor of 2 higher than for lithium. Also the mass of lithium is smaller, which leads to an increased radius of the area where Majorana losses can occur. A detailed discussion can be found in [64]. In order to trap lithium in the $|F = 3/2, m_F = 3/2\rangle$ stretched state, a plug power of 5W (2.5W to trap the $|F = 1/2, m_F = -1/2\rangle$ state) would be necessary. We cannot afford this high power requirement, since we are limited in the available laser power of the pump beam.

5.2.2. Cloverleaf Trap

Another class of magnetic traps that use only dc-fields to create a harmonic potential with a finite offset are the Ioffe-Pritchard type traps. In the discussion we will focus on the Cloverleaf configuration, a design first reported in [66], since it provides the possibility of spin-cleaning the loaded atomic sample as discussed in section 5.2.3.

A cut through our coil design is shown in fig. 5.2 where in this orientation another coil set would be placed above this picture. It consists of different sets of coils to create a 3D confinement. The first set of coils produces a radial gradient (gradient coils) of 0.44G/cm/A and 0.42G/cm/A in the perpendicular direction accordingly[1].

In the first place a harmonic axial confinement of 0.77G/cm^2/A is created by the curvature coils (red in fig. 5.2). These consist of a set of coils with current flowing in the same direction, creating a magnetic bottle neck potential with an offset field of 3.14G/A. In order to increase the curvature of the radial potential, a Helmholtz field of 3.21G/A (created by the antibias coils in blue) is subtracted to get the trap bottom close to zero. Fluctuations of the magnetic field are reduced by running both coils in series by the same power supply. An additional bias current through the curvature coils is added in order to avoid a zero crossing of the magnetic field along the axial direction. This zero crossing occurs since the field produced by the antibias coils is slightly stronger than the one produced by the curvature coils.

The finetune coils (yellow) are also in Helmholtz configuration and are used to do fast magnetic field sweeps of 0.51G/A or – if only one coil is used – to apply a gradient field for a Stern-Gerlach experiment.

The field gradient for the MOT is generated by using one curvature and one antibias coil in different holders. They produce a gradient of 1G/cm/A. The magnetic properties of our coil design is summarized in table 5.1. For more details about the design of the cloverleaf trap the reader is referred to the appendix B.

Magnetic Potential

The magnetic field produced by the cloverleaf trap reads [21]:

[1] both values differ slightly because every gradient coil set is made of two types—clockwise and counterclockwise ones like the direction of the flowing current—which differ in their winding number by one.

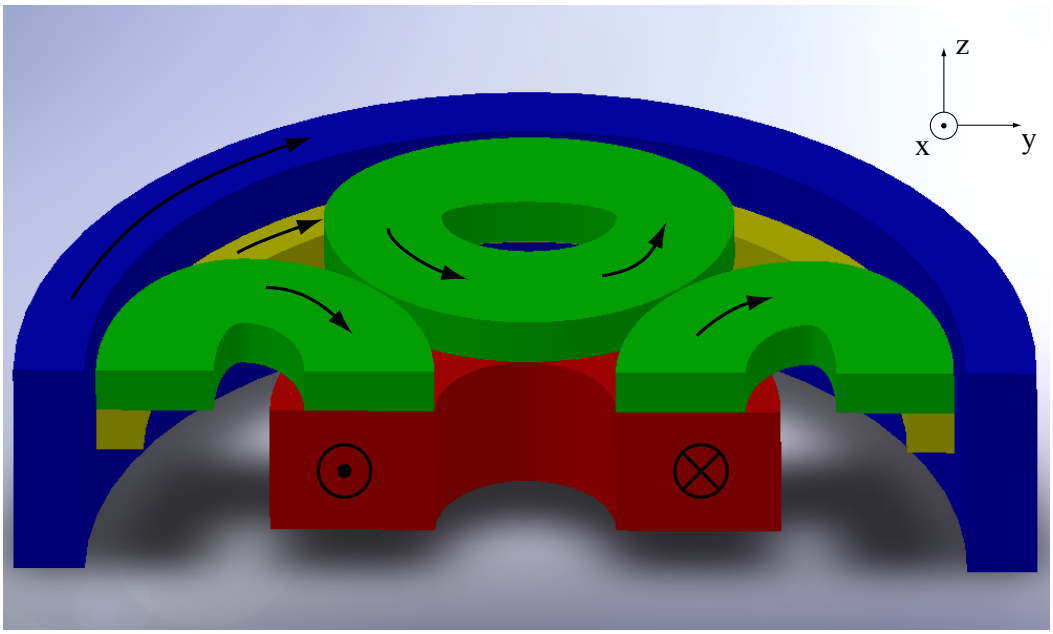

Figure 5.2.: *Cut through our cloverleaf coils: in this depiction the atoms are trapped above the coils. The coils are: antibias (blue), curvature (red), gradient (green) and finetune (yellow). The arrows indicate the current direction in the coils.*

	B_0 [G/A]	B' [G/cm/A]	B''_z [G/cm^2/A]
antibias	3.21 (3.267)		(2×10^{-3})
curvature	3.14 (3.269)		0.77 (0.87)
gradient		0.44 / 0.42 (0.45)	
finetune	0.51 (0.52)		

Table 5.1.: *Measured magnetic properties of the cloverleaf trap, the calculated values are shown in brackets. The finetune coils are designed to be in perfect Helmholtz configuration.*

$$\vec{B} = B_0 \begin{pmatrix} 0 \\ 0 \\ 1 \end{pmatrix} + B' \begin{pmatrix} x \\ -y \\ 0 \end{pmatrix} + \frac{B_z''}{2} \begin{pmatrix} -xz \\ -yz \\ z^2 - \frac{1}{2}(x^2+y^2) \end{pmatrix} \tag{5.14}$$

which is only obtained by the symmetry of the system and Maxwell's equations. In order to calculate the atomic potential the absolute value of the magnetic field needs to be calculated.

$$|\vec{B}|^2 = B_0^2 + B_0 B_z'' z^2 + \frac{B_z''^2}{4} z^4 + \left(B'^2 - \frac{B_0 B_z''}{2} \right) \rho^2 + \frac{B_z''^2}{16} \rho^4 + B' B_z'' z (y^2 - x^2) \tag{5.15}$$

Here cylindrical coordinates have been used with $\rho = \sqrt{x^2+y^2}$. In the low temperature limit (i.e. $k_\mathrm{B} T \ll \mu_\mathrm{m} B$) the atoms will be concentrated at the bottom of the potential, corresponding according to eq. (5.12) to the bottom of the magnetic field. Therefore eq. (5.15) can be expanded to quadratic order around $(\rho, z) = (0, 0)$ and reads:

$$|B| \simeq B_0 + \frac{B_z''}{2} z^2 + \frac{1}{2} \underbrace{\left(\frac{B'^2}{B_0} - \frac{B_z''}{2} \right)}_{B_\rho''} \rho^2 \tag{5.16}$$

where B_ρ'' is the effective radial curvature of the trap. This approximation holds when loading a MOT of $\sim 250\mu$K into the cloverleaf trap as long as $B_0 \gg 4$G for sodium in $|F = 2, m_F = 2\rangle$. After compressing the cloud by ramping down B_0 to $B_0 \approx 1$G, the trap is operated in the linear regime, where the magnetic potential is predominantly linear in the radial direction and harmonic in the axial direction. After evaporatively cooling the atomic samples to lower temperatures, the trap is again predominately harmonic. From equation (5.16) the trapping frequencies of a cooled cloud can be deduced:

$$\omega_{z/\rho} = \sqrt{\frac{\mu_m B_{z/\rho}''}{m}} \tag{5.17}$$

yielding maximal trapping frequencies of $\omega_\rho = 2\pi \times 463$Hz and $\omega_z = 2\pi \times 33$Hz for $B_0 = 1$G in order to suppress Majorana losses. However the radial terms $\sim xz$ in equation (5.14) cause some problems in the radial direction. As depicted in fig. 5.3 these terms give rise to additional minima of the magnetic field and therefore instabilities of the trapping potential. These instabilities need to be at a region far apart from the MOT region and occur at:

$$z_\mathrm{inst} = \pm \left(\frac{B'}{B_z''} - \frac{B_0}{2B'} \right). \tag{5.18}$$

This requires high currents when loading the atoms from the MOT into the cloverleaf trap.

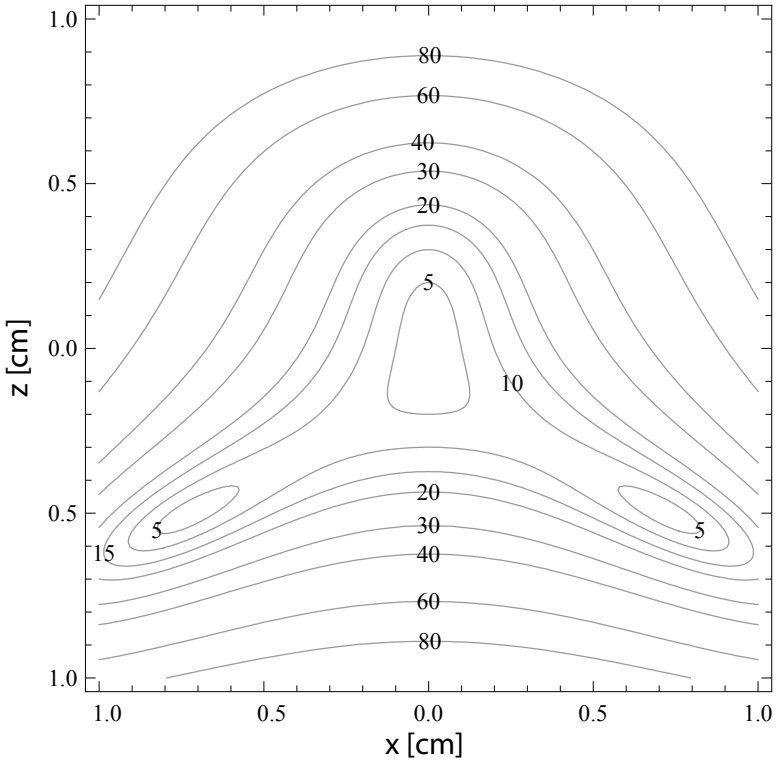

Figure 5.3.: *Instable points of the trap. The contour lines depict the value of the magnetic field in G as indicated. The minima at $z \neq 0$, but at finite x values are the instable point of the trapping geometry. B_0, B' and B'' have to be chosen such, that those points do not overlap with the MOT region. Otherwise the atoms would be expelled from the trap when loading them into the magnetic trap. The calculation parameters are: $B_0 = 1\text{G}$, $B' = 50\text{G/cm}$, $B''_z = 200\text{G/cm}^2$*

After evaporation and loading the optical dipole trap the antibias coils can be used to produce a large homogeneous magnetic field. Fast magnetic field ramps can be done using the finetune coils, since their inductance is much lower. For a detailed connection diagram the reader is referred to the appendix B.

5.2.3. Special Requirements in a Two Species Design

After the water leak in the cooling system lead to a overheating of the quadrupole coils that broke our vacuum setup and the coil setup we decided to do a complete redesign of our experiment. The old design had some weak points and we took it as a chance to improve it. The plugged quadrupole setup was conceptually very easy but there encountered some problems that are not easy to solve:

- As already mentioned, the available power of 1W of the plug laser beam would not have been sufficient to trap lithium in one of the $|F = 1/2, m_F = -1/2\rangle$ or $|F = 3/2, m_F = 3/2\rangle$ hyperfine states. The created repulsive potential would

have been too shallow to reduce the Majorana loss rate to a desirable value. The most promising upgrade to the old setup would have been a two-plug scheme while adding a second plug beam which is only slightly blue detuned to the lithium transition line, thus creating a strong repulsive potential for lithium while degrading the sodium plug potential only a little. Details on this proposed scheme can be found in [64]. An additional plug beam, would have waisted a lot of optical access, since it cannot be send trough the same fiber as the existing one. The reason is the following: The facet of the plug fiber is cut under an angle of 8°[2]. This angle and a wavelength difference of approximately 150nm between the high power plug beam and the proposed second, low power plug would result in a displacement of the focus of the two beams by more than their waist, due to the slightly different refractive index of the fiber.

- ^{6}Li in a magnetic trap is only stable against spin-changing collisions when being spin polarized to one of the trappable stretched states $|F = 3/2, m_F = 3/2\rangle$ or $|F = 1/2, m_F = -1/2\rangle$. The latter one bends from low-field-seeking into high-field-seeking at a magnetic field of $\sim$ 27G which corresponds to $\simeq 300\mu$K. Although the Doppler temperature of lithium is only 140μK, we do not have much hope to see any lithium atoms remaining in the trap, when being loaded together with a rather mK hot sodium MOT. Therefore the $|F = 3/2, m_F = 3/2\rangle$ state has to be used. This favors sodium to better be in the $|F = 2, m_F = 2\rangle$ state since this combination is stable against spin-exchange. A crucial point for this scheme is to get rid of the sodium atoms in the $m_F = 1$ and $m_F = 0$ states [67] which can be easily done in a cloverleaf trap. This is due to the fact that the Zeeman splitting of both states differs according to their different m_F quantum numbers. The trap bottom is now raised high enough such that atoms in those different hyperfine states separate energetically by more than their temperature. Atoms in the undesired states are removed, using resonant microwave photons to transfer them into high-field seeking states that get expelled from the trap. In a plugged quadrupole configuration there is no easy way tho achieve this. The trapping frequencies at the bottom of the trap are in the range of 1kHz, such that a spatial splitting due to the differential gravitational sag is negligible. Far away from the plug the trap is linear such that no shift occurs between the different hyperfine states.

  In a TOP configuration it is fairly hard to raise the bottom of the trap to the desired value of $\sim$ 80G, since this requires a large rotating magnetic field. The same argument holds for a QUIC trap where the magnetic field at the bottom of the trap is also fairly low. Another problem of the QUIC configuration is the huge position shift of the trap center with respect to the symmetry point of the anti-Helmholtz coils. This automatically introduces a less homogeneous field over the sample, once it is loaded into the optical dipole trap. But in order

[2]We use FC/APC connectors in order to prevent multiple reflections between the fiber facet and optical elements placed after the fiber, which would decrease the stability of the beam.

to address a desired value of the scattering length between atoms precisely via a Feshbach resonance, the applied magnetic field must be homogeneous across the whole sample.

For these reasons we decided to use a cloverleaf trap in the new setup although the collision rate—which determines the speed of evaporation—is inferior to the plugged quadrupole trap.

5.3. Imaging

We use an absorption imaging technique to determine the information of our cold atomic samples. A schematic view of the setup is shown in fig. 5.4. The atoms are illuminated by a gaussian laser beam of intensity I_0, having the right frequency and polarization to excite the cycling transition $|F = 2, m_F = 2\rangle \rightarrow |F' = 3, m_{F'} = 3\rangle$ of the sodium D_2 line. The atomic cloud casts a shadow that is imaged onto a CCD camera, using an objective. We use a *Q-Imaging Retiga EXi* camera, having (1392×1040) pixels with a pixelsize of $(6.45 \times 6.45)\mu$m. The objective is a *Zeiss Plan-Achromat S* with a focal length of 100mm. We also installed a rough-imaging setup using a singlet lens with a focal length of 150mm, providing a magnification of $M = 1/2.52$ in order to image the MOT and the uncompressed magnetic trap. This setup is set under an angle of 50° and serves as an excellent monitoring tool. Its magnification was determined, by releasing the trapped atomic cloud from a cooled magnetic trap and monitoring their center of mass during their free fall due to the gravity. Applying a fit to the center of mass motion yields the magnification of the rough imaging setup.

The magnification of the standard imaging setup could not be determined using this method, since the images are taken along the direction of gravity. The magnification was measured by comparing in-situ and time-of-flight images taken under the same conditions with both imaging setups. This comparison yields a magnification of $M = 2.3 \pm 0.2$ for our good imaging setup.

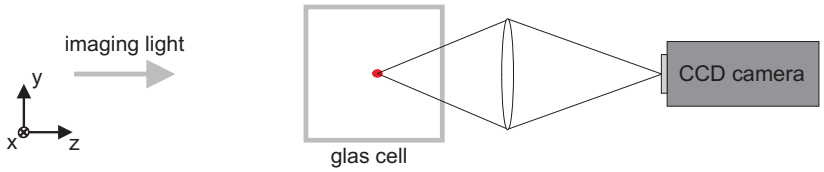

Figure 5.4.: *Schematic view on the absorption imaging setup. The atoms (red) are illuminated by a gaussian beam and imaged by an objective onto a CCD camera.*

Since we use resonant light to image the atoms, a lot of energy is transferred to them during an imaging pulse and the atoms are heated out of the trap. Therefore every picture corresponds to a new experimental cycle. There are also non-destructive methods like phase contrast imaging [21] available, but up to now we do not use these techniques in our experiment.

In order to obtain the atom number from the pictures, the following analysis is done: In total 3 pictures per cycle are taken, which are: (i) a picture with the atoms I_{pic}, (ii) a reference picture I_{ref}, done under the same conditions as I_{pic}, but without the atoms being present. This picture is to remove imperfections of the imaging light distribution due to dust or imperfect optical elements in the imaging light path. (iii) a background picture I_{back}, where everything is switched off in order to remove stray light or the influence of hot pixels. Note that in the following we will not write the position dependence of the intensities explicitly $I(x, y) \equiv I$.

From these pictures the relative transfer function $T(x, y)$ can be derived, where fringes are removed and only the atomic cloud survives.

$$T(x, y) = \frac{I_{\mathrm{pic}} - I_{\mathrm{back}}}{I_{\mathrm{ref}} - I_{\mathrm{back}}} = \frac{I_{\mathrm{out}}}{I_{\mathrm{in}}} \tag{5.19}$$

The imaging light is absorbed by the atomic cloud $\tilde{n}(x, y, z)$ following Lambert-Beer's law as $dI/dz = -\tilde{n}(x, y, z)\sigma(z)I(x, y, z)$ per length element dz, where $\sigma(z)$ is the on resonance scattering cross section given by:

$$\sigma(z) = \frac{\Gamma}{2}\frac{\hbar\omega_0}{I_{\mathrm{sat}}}\frac{1}{1 + I/I_{\mathrm{sat}}} \tag{5.20}$$

where I_{sat} denotes the saturation intensity. The imaging procedure integrates the 3D atomic density profile $\tilde{n}(x, y, z)$ along the imaging direction which is in our case the z-axis, and reveals the 2D column density $n(x, y)$ which is proportional to the relative transfer function. Inserting these equations into the Lamber-Beer's law and integrating over to imaging direction yields:

$$n(x, y) = \int_{-\infty}^{\infty} \tilde{n}(x, y, z)dz \tag{5.21}$$

$$n(x, y) = \frac{2}{\Gamma}\frac{I_{\mathrm{sat}}}{\hbar\omega_0}\left[-\log\frac{I_{\mathrm{out}}}{I_{\mathrm{in}}} + \frac{I_{\mathrm{out}}}{I_{\mathrm{sat}}} - \frac{I_{\mathrm{in}}}{I_{\mathrm{sat}}}\right] \tag{5.22}$$

Taking into account the finite size A of a pixel, corrected by the magnification M of the imaging system, the atom number per pixel reads:

$$N_{\mathrm{pix}} = \frac{2}{\Gamma}\frac{I_{\mathrm{sat}}}{\hbar\omega_0}\frac{A}{M^2}\left(OD + \frac{I_{\mathrm{out}}}{I_{\mathrm{sat}}} - \frac{I_{\mathrm{in}}}{I_{\mathrm{sat}}}\right). \tag{5.23}$$

Here the optical density OD of the atomic cloud has been introduced.

$$OD = -\log\frac{I_{\mathrm{out}}}{I_{\mathrm{in}}} = -T(x, y) \tag{5.24}$$

Since it is hard to measure I_{out} precisely, the second last term of eq. (5.23) is neglected, which leads to a slight underestimation of the atom number.

5.4. Deducing the Temperature

The temperature of an atomic cloud can be extracted from the absorption images. It is deduced from the thermal gas inside a trap, or the thermal background of a BEC. The density profile of a thermal cloud trapped in an external potential V_{ext} is given by the Boltzmann distribution:

$$n(r) = n_0 \exp\left(-\frac{V_{\text{ext}}(r)}{k_{\text{B}}T}\right). \tag{5.25}$$

In a 3D harmonic oscillator potential (e.g. the compressed cloverleaf trap at low temperatures or the optical dipole potential) with $V_{\text{ext}} = \frac{1}{2}m(\omega_x^2 x^2 + \omega_y^2 y^2 + \omega_z^2 z^2)$, the density distribution has a gaussian shape.

$$n(r) = N\left(\frac{m\overline{\omega}^2}{2\pi k_{\text{B}}T}\right)^{3/2} \exp\left(-\frac{x^2}{2\sigma_x^2}\right) \exp\left(-\frac{y^2}{2\sigma_y^2}\right) \exp\left(-\frac{z^2}{2\sigma_z^2}\right) \tag{5.26}$$

The gaussian widths are fixed by $\sigma_i\omega_i = \sqrt{k_{\text{B}}T/m}$ and $\overline{\omega}$ is the geometric mean of the trapping frequencies.

If the external potential is turned off and the atomic cloud can freely expand, the atoms will move a distance $r = pt/m$ according to their initial momentum p. The widths $\sigma_i(t)$ of the cloud will thus evolve as:

$$\sigma_i(t)^2 = \frac{k_{\text{B}}T}{m\omega_i^2} + \frac{k_{\text{B}}T}{m}t^2 \tag{5.27}$$

$$\sigma_i(t)^2 = \frac{k_{\text{B}}T}{m\omega_i^2}\left(1 + \omega_i^2 t^2\right). \tag{5.28}$$

After a sufficiently large expansion time ($\omega t \gg 1$), the density profile will be proportional to the initial momentum distribution. Due to a finite resolution of the imaging system used in the experiment, a precise measurement of the temperature is done by imaging the atomic cloud after different times after switching off the trapping potential (time-of-flight images). Applying a fit to the measured widths of the cloud reveals their initial temperature using eq. (5.28).

Due to the absence of interaction, the expansion of the thermal cloud is always isotropic. In a BEC with non-vanishing interactions the Thomas-Fermi approximation applies and the density profile has an inverted parabola shape in a harmonic confinement. The widths of the BEC is determined by the trap parameters according to eq. (2.17): $R_i^{\text{B}} = \sqrt{2\mu/m\omega_i^2}$. Releasing the BEC from the trap results simply in a rescaling of those parabolic widths. Further details can be found in [68].

When releasing a partial condensed cloud from the trap both components, thermal background and BEC fraction will result in a bimodal density distribution. The thermal background will expand isotropically with a gaussian shape and the BEC will keep its TF profile.

6. Experimental Setup

In this chapter, an overview over the experimental setup is presented. The vacuum and laser setup will be discussed and the main cooling steps needed to reach Bose-Einstein condensation of sodium will be explained. Benchmark measurements at crucial cooling steps will be reported. At the end of this chapter measurements, showing the Bose-Einstein condensation of sodium atoms to two magnetic trap configurations will be presented.

6.1. Vacuum System

Ultracold atom experiments have to be done under ultra high vacuum (UHV) conditions. A sketch of the vacuum system is given in fig. 6.1, where the beam preparation and the differential pumping stages are shown, and in fig. 6.2 where the UHV part of the apparatus, including the Zeeman slower and the glass cell are depicted. A detailed discussion about the design criteria of the vacuum setup can be found in [69].

Slight changes have been made compared to the setup described therein, concerning the iris mounting (I) to ensure a better heat contact. We also welded the oven nozzle (N) and the pumping tube between the sodium and lithium oven, because there encountered some leaks in the old design. The vapor pressures of sodium and lithium differ by 4 orders of magnitude at the same temperature, which requires a differential pumping tube already between the sodium and lithium reservoirs. The operation temperature of the ovens is 350°C for sodium and 380°C for lithium. In this way no sodium is deposited in the lithium reservoir and the sodium flux can be adjusted by the temperature of the sodium oven only. The oven nozzle (N) is heated to ≈ 500°C to prevent sodium and lithium to get stuck there. We deposited 50g of ^{23}Na and about 5g of enriched ^{6}Li in the oven. This amount of sodium typically lasts about 1 year of operation.

The collimation of the atomic beam leaving the oven is done by the oven nozzle (N, diameter of 4mm) and the first differential pumping tube (DP1, conical, smallest diameter of 5mm, length 130mm) in fig. 6.1. Both are separated by 365mm and define a full angle of aperture of 1.4°. The rest of the atoms, leaving the oven under a larger angle, are just a gas load to the background pressure and either stick to the iris (I), to the walls of the chamber or need to be pumped in order to reduce the pressure to 5×10^{-8}mbar.

We installed a cold spot (CS), cooled down by two 120W peltier elements, in order to get as much sodium as possible sticked to the walls of the first 6-way cross after the oven, thus preventing them from degrading the ion getter pump (IP1, *Varian*

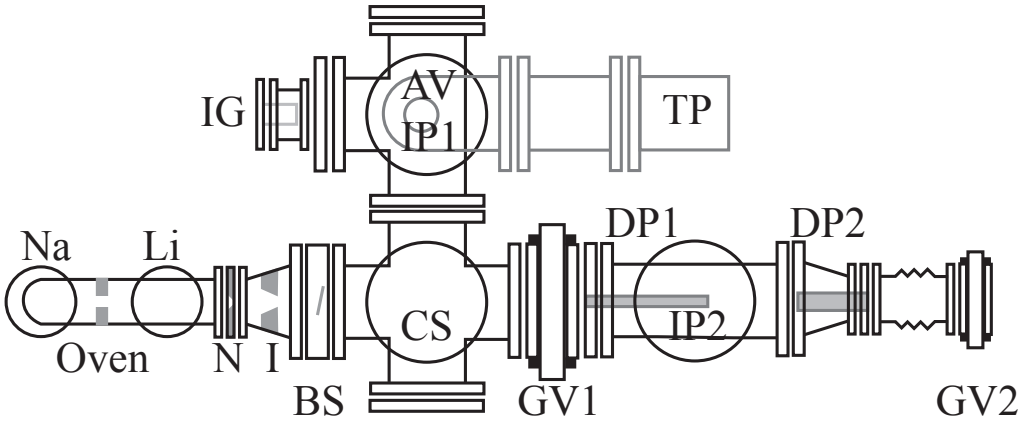

Figure 6.1.: *Schematic top view of the front part of the vacuum setup (not to scale). Only components in the main plane are shown in solid lines. The grey shaded parts of the angle-valve (AV) and the turbopump (TP) are mounted above the main plane. The parts below the plane are the Ion Pumps (IP1,IP2) and the cold spot (CS). The main parts in the plane are the Oven, where the sodium and lithium ovens as well as the oven nozzle (N) and the iris (I) are indicated. The atomic beam shutter (BS) used to hinder atoms from reaching the trapping region after the MOT is loaded, an Ion Gauge (IG), two gate valves (GV1, GV2) and the differential pumping tubes (DP1,DP2).*

Diode 55l/s). There are also windows installed, allowing the sight perpendicular to the Zeeman slower beam which serves as an excellent inspection tool. A shutter is placed directly after the oven, which blocks the atoms after the MOT is loaded, thus allowing long lifetimes of the atoms being trapped by the magnetic or optical dipole trap.

If the sodium oven needs to be refilled, the first part of the vacuum chamber can be vented independently from the glass cell region by closing the gate valve (GV1) and venting the system using the angle valve (AV).

The differential pumping tubes DP1 and DP2 reduce the pressure by a factor of 100 and 10 respectively, thereby permitting a pressure below 10^{-11}mbar in the glass cell region. This is low enough to reduce the background gas collision rate of the trapped atoms sufficiently to afford Bose-Einstein condensation.

The rear part of the vacuum chamber including the glass cell (GC), where all the experiments take place is depicted in fig. 6.2. The cell is made of 4mm thick Quartz glass and has a rectangular shape with outer dimensions of $(40 \times 40 \times 150)$mm. A glass-metal transition with a free inner diameter of 38mm is attached to both face sides, each of them equipped with a bellow to reduce the mechanical stress onto the cell. The input port of the glass cell – in the direction the atoms reach the cell – has a rotatable CF40 Flange. The sleeve of the flange has been demounted by *Hellma*, the manufacturer of the glass cell, and we replaced it by a sectional one (S) that has been attached to the cell after imposing the second part of the Zeeman slower onto the glass-metal transition. This allows a smaller diameter of the second part of the

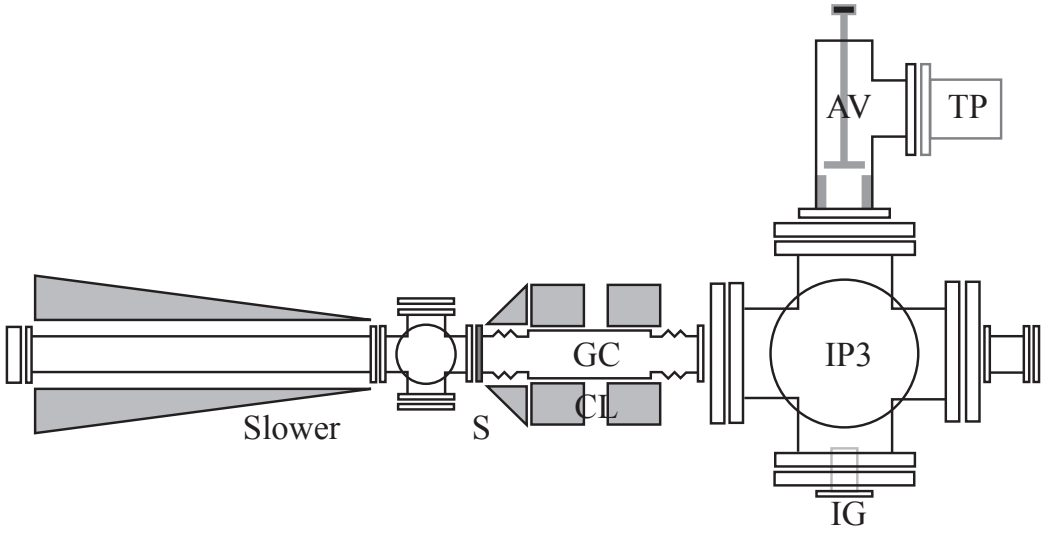

Figure 6.2.: *Schematic top view of the glass cell part of the vacuum setup (not to scale). Only components in the main plane are shown. The spin-flip Zeeman slower is depicted, the glass cell (GC) surrounded by the Cloverleaf coil mount (CL), an ion gauge (IG) to monitor the background pressure, an ion pump (IP3) with attached Ti sublimation pump, and angle valve (AV) where a turbopump (TP) can be mounted. (S) indicates the sectional flange of the glass cell.*

Zeeman slower and therewith a faster decay of its magnetic field.

An ion getter pump (IP3, *Varian VacIonPlus 150*) with an attached Ti-sublimation pump keeps the pressure in this last part of the vacuum chamber well below the detection limit of the attached Ion Gauge (IG), which is 2.7×10^{-11}mbar. A CF40 window at the end of the vacuum chamber serves as the input port for the laser beam of the Zeeman slower. Because of the corrosiveness of the window due to lithium impact, this window is heated to $\approx 200°$ to increase the desorption rate of lithium, thereby keeping the window transparent.

Zeeman Slower

The fist cooling stage of the experiment is a spin-flip Zeeman slower as described in detail in [70]. The changes made, compared to the old design described therein include a new cooling design of the slower tubes and a smaller diameter of the second part of the Zeeman slower. This allows to reduce the distance between the slower and the MOT, since the magnetic field of the slower decays faster compared to the old design. The cooling is made such that the cooling water never gets in contact to any soldered part of the pipes and the water connections are done using the *Swagelok* system.

The basic principle of a Zeeman slower is to apply a spatially varying Zeeman shift on the atomic levels which compensates the changing Doppler-shift as the atoms are slowed down by absorbing resonant photons out of a counter- propagating laser beam.

	AOM frequency [MHz]	Transition	Detuning [MHz]
Spectroscopy	2× +71	crossover $F' = 2, F' = 3$	-71-29
MOT	+82	$F = 2 \rightarrow F' = 3$	-18
Repumper	+1784	$F = 1 \rightarrow F' = 1$	+5
Slower	-200	$F = 2 \rightarrow F' = 3$	-300
Imaging	+100	$F = 2 \rightarrow F' = 3$	0
Umpump	+65	$F = 2 \rightarrow F' = 2$ @ B=0G	+23
Dark Spot	+33	$F = 1 \rightarrow F' = 2$	+4

Table 6.1.: *Transitions and frequencies of the AOMs of the sodium setup, the detunings are defined $\Delta = \omega_L - \omega_0$, such that negative detunings correspond to a red detuning. Note that the spectroscopy-AOM is used in double-pass configuration.*

In order to ensure a constant deceleration, the magnetic field needs to have a square-root profile.

$$B(z) = B_0\sqrt{1 - \frac{z}{z_0}} + B_{\text{offset}} \tag{6.1}$$

z_0 is the length of the atoms path through the slower and B_0 as well as the detuning Δ of the slower light define the maximum capture velocity which is $v_{\text{capt}} \approx 700\text{m/s}$ in the case of sodium. B_{offset} is negative in our case, which introduces a zero-crossing in the magnetic field of the slower, where the atoms have to be repumped into the cycling transition which is done using an EOM in our setup. The height of its sidebands is approximately 30%. The atoms leave the slower with a velocity of $v_{\text{end}} \approx 30\text{m/s}$ which is below the capture velocity of our magneto-optical trap (MOT).

Before explaining the MOT in more detail, the reader is introduced to our laser system, providing light at the right frequencies and intensities to enable the next cooling step.

6.2. Sodium Laser System

The laser setup for the cooling of sodium is based on an actively stabilized, single frequency ring-dye laser by *Radiant Dyes* which provides an output power on a day to day basis of approximately 1W. It is pumped by a *Coherent Verdi V10*, a frequency doubled, diode pumped Nd:YVO_4 laser at $\lambda = 532\text{nm}$.

The dye laser is locked by Doppler free absorption spectroscopy to the $F = 2 \rightarrow F' = 3$ crossover peak. We only shift the frequency of the pump beam to $\omega_0 + 2\Delta\omega$, using an AOM in double pass configuration. The resonance condition for the atoms therfore reads:

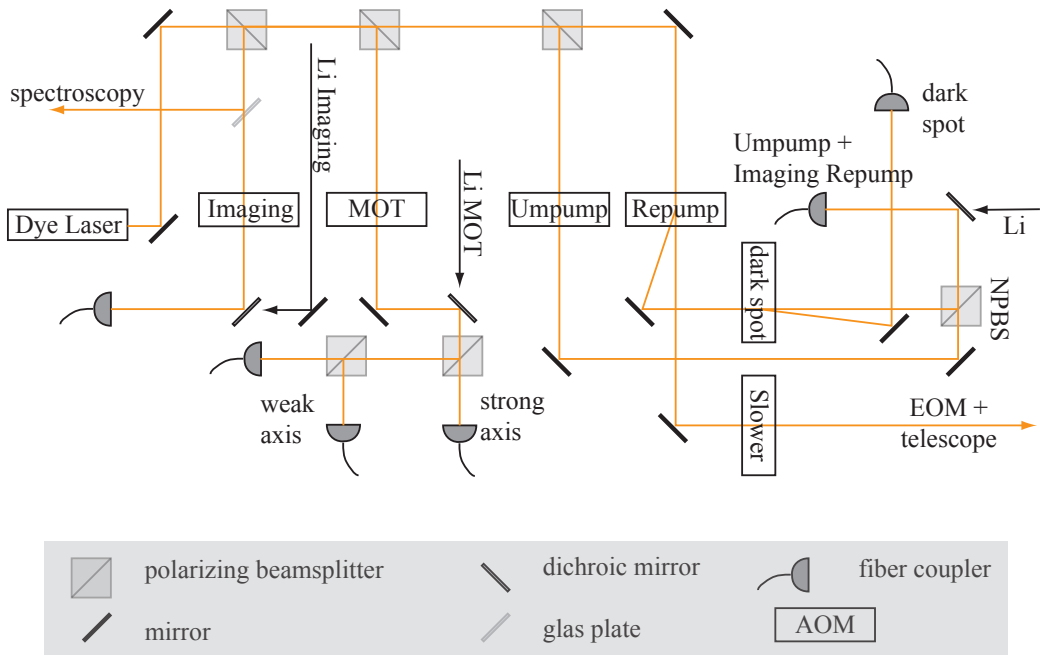

Figure 6.3.: *Scheme of the sodium laser system. The frequencies of the AOMs can be found in table 6.1. NPBS specifies a non-polarizing beamsplitter.*

$$\text{pump beam:} \quad 0 = kv + \omega_0 + 2\Delta\omega \tag{6.2}$$

$$\text{probe beam:} \quad 0 = -kv + \omega_0 \tag{6.3}$$

$$\Rightarrow \quad v = -\frac{\Delta\omega}{k}. \tag{6.4}$$

Thus the atoms are resonant with light shifted by the single AOM frequency of $\Delta\omega$. In order to lock the laser to the top of the crossover peak, we modulate the frequency of the AOM and use the lock-in technique to produce a derivative of the spectroscopy signal.

Since we use separate optical tables for the laser setup and the vacuum setup, all beams – except the slower – are coupled to single mode fibers and send to the other table. This strategy has several advantages: Firstly, the light leaving these fibers has a clean TEM_{00} mode which is advantageous for laser cooling experiments. Secondly, a realignment of the optics setup before the fibers has no influence on the beam positions at the glass cell.

Contrary to the old setup [71], which was designed for high flexibility using double-pass AOM configurations, the new layout is optimized for power efficiency. A scheme of the sodium layout can be found in fig. 6.3 and the corresponding frequencies and transitions are listed in table 6.1.

Since at a later stage of the experiment, laser cooling of ^{6}Li atoms needs to be included, these beam paths need to be thought of when designing the sodium setup.

Our solution is to couple the lithium beams into the same optical fibers as the sodium beams. Overlapping of both is done using dichroic mirrors before the fibers. The lithium imaging, MOT, repump and spin polarizing (umpump) beams can be added to the corresponding sodium beam paths. Thereby one has to take care that both beams – sodium and lithium – need to be polarized along the same axis. For this reason, overlapping both colors cannot be done with a simple polarizing beam splitter cube without waisting 50% of the power. Moreover, since the hyperfine structure of lithium $2^2P_{3/2}$ state cannot be resolved, repumping and MOT light for lithium cannot be separated and are fed into the same beam path [58].

Lithium light is added to the slower beam path after the sodium light has been passed through the EOM, modulating sidebands at 1720MHz for the repumer transition at the zero-crossing of the Zeeman slower. Afterwards the beam is expanded by a telescope to a diameter of $d_{\text{slower}} \approx 35\text{mm}$.

A schematic of the output couplers of the MOT beams are shown in fig. 6.4. The beam leaves the single-mode fibers being collimated by standard outcouplers and is passed through a polarizing beam splitter cube to clean the polarization. After passing a zero order $\lambda/4$ waveplate for $\lambda = 633\text{nm}$, made by *CVI-Melles Griot*, the beam is expanded by a telescope to a final waist of 11mm. An iris in the telescope can be used to shrink the beam size, which is an excellent tool when aligning the MOT beams onto the magnetic field zero.

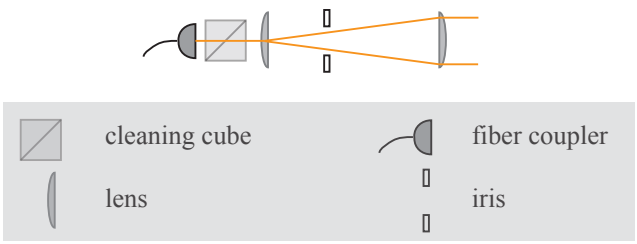

Figure 6.4.: *Scheme of the MOT output couplers used in the new setup.*

6.3. Magneto-Optical Trap

The slow atoms leaving the Zeeman slower and entering the glass cell are captured by a 3D magneto-optical trap (MOT) [72]. Our setup consists of four beams, where two beams in the plane of the weak axis of the MOT's quadrupole field are retro-reflected (x-y plane), and the other two beams are counter-propagating along the strong axis, which is the z-axis. The MOT beams are slightly red-detuned with respect to the cycling transition—see fig. 6.1. A gradient field is produced by 1 antibias and 1 curvature coil of our cloverleaf magnetic trap, providing a gradient of 10G/cm.

The repumper beam, being linearly polarized, is shone in under Brewsters angle. The center of the beam can be blocked by an opaque spot in order to create a dark-spot MOT [73].

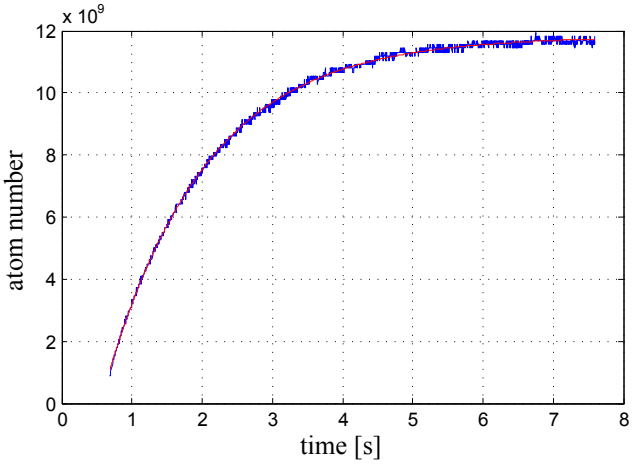

Figure 6.5.: *Loading curve of a bright MOT yielding a loading rate of* $8.2 \times 10^9 atoms/s$ *and a time constant of* $\tau = 1.43s$*. The temperature of the sodium oven was* $350°C$*.*

A loading curve of a bright MOT is shown in fig. 6.5. It is measured using a photodiode to collect the fluorescence signal of the atoms. The loading curve is fitted by

$$N(t) = N_0(1 - e^{-t/\tau}) \tag{6.5}$$

where the initial slope yields a loading rate of 8.2×10^9atoms/s. The fluorescence signal of a dark spot MOT is a factor of 32 lower.

Dark Spot MOT

The achievable densities of a MOT are limited mainly due to two factors: Firstly, reabsorption of scattered light coming from the center of the could (= region of highest densities) balances with the confining force due to the red detuned cooling laser beams. This process is known as radiation trapping. Secondly, light assisted collisions, where an excited state atom collides with a ground state atom thereby releasing part of its energy as kinetic energy to the scattering compounds. Both mechanisms set the maximum achievable MOT density to approximately $1 \times 10^{11}\text{cm}^{-3}$ [73].

The idea of a dark-spot MOT is to overcome these limits is to shield the repumper light from the trapping center by an opaque mask, such that the atoms there are trapped in a dark state ($F = 1$ manifold in our case). This manifold is dark with respect to the cooling light. Whenever an atom leaves the trap center, it is brought back to the cycling transition by the repumper beam and is cooled again until it reaches the trap center.

The atoms at the MOT center will therefore be distributed among the $F = 1$ hyperfine states, whereas the atoms in the outer regions populate the $F = 2$ manifold.

This technique increases the achievable sodium MOT peak density by an order of magnitude in our experiment, measured after loading the magnetic trap.

6.4. Spin Polarizing and Purification

In order to maximize the transfer efficiency to the magnetic trap, the atoms need to be pumped into the $|F = 2, m_F = 2\rangle$ state. But the high optical density of the dark-spot MOT limits the efficiency of a simple spin polarization scheme as for instance applied in ^{87}Rb experiments. Therefore other schemes have to be applied. When loading the magnetic trap and only applying a repumper pulse to the dark-spot MOT, about 1/5 of the atoms are transferred in the desired $|F = 2, m_F = 2\rangle$ state. The $|F = 2, m_F = 1\rangle$ and $|F = 2, m_F = 0\rangle$ states are also trapped but need to be removed to prevent spin-changing collisions between atoms in different states.

The MIT group reported a scheme where they remove the unwanted states using a microwave transition and gave the atoms a second chance to reach the desired state by applying a laser pulse. In this way they achieve a transfer efficiency of 35% [67].

Another method of spin-polarizing was demonstrated by the Utrecht group using atoms in $|F = 1, m_F = -1\rangle$ state [74]. They used the fact that at large magnetic field the distances between the optical transition lines of sodium atoms increase and thus off-resonant scattering as well as reabsorption of spontaneous emitted photons is minimized. In their paper they present a working scheme for the $F = 1$ manifold increasing the transfer efficiency at maximum by a factor of 2.7. The trick is to find a combination of magnetic field strength and optical transitions that are stable against polarization imperfections and magnetic field instabilities while still reducing the off-resonant scattering rate remarkably.

In the following a similar scheme for the $F = 2$ manifold is discussed. A scheme of the applied optical transitions is shown in fig. 6.6. We define the quantization axis for the spin-polarizing scheme using the finetune coils. The light is coupled into the second port of the cleaning cube of one one the MOT beams as shown in fig. 6.4, pointing along the symmetry axis of the finetune coils, thus defining the polarization of the beam as good as possible.

Nevertheless, the role of polarization imperfections onto the spin-polarizing scheme has to be considered, since this degrades the efficiency of the applied scheme. Therefore the transition frequencies for σ^+ and σ^- polarized light have been calculated as a function of the magnetic field B. The aim is to find a magnetic field, a repumper and a umpump detuning at which the σ^+ transitions are clearly favored compared to possible σ^- transitions. As can be seen from fig. 6.7 the situation is not as clear as in the $F = 1$ case of [74]. The circle indicates the chosen magnetic field and detuning with respect to the $F = 1 \rightarrow F' = 0$ transition. The detuning of the beam, depopulating the $F = 1$ manifold is fixed by the repumper setup of our MOT beams. As can be seen from fig. 6.7 (a), this beam is always close to resonance with the σ^+ transition into the $|F' = 1, m_{F'} = 0, 1\rangle$ states. Only at large magnetic fields, those transitions split further apart, which sets an upper bound on the magnetic field. From fig. 6.7

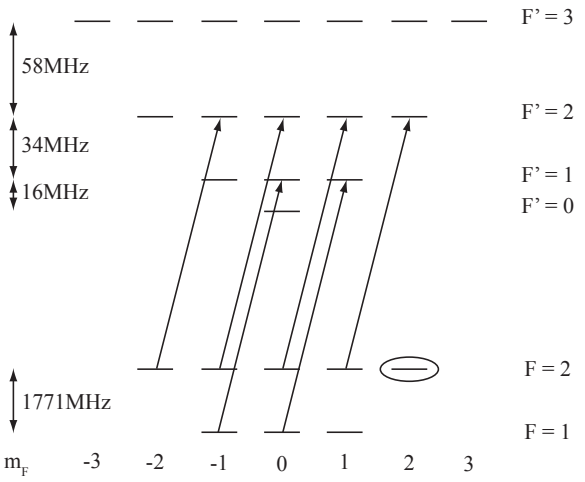

Figure 6.6.: *Scheme of the applied spin-polarizing transitions. Atoms in the unwanted sublevels of the $F = 1$ and $F = 2$ manifold are pumped using σ^+ polarized light to the excited states. They can decay from those levels (not shown in the figure) following the selection rule $\Delta m = 0, \pm 1$ and are optically pumped until they reach the desired $|F = 2, m_F = 2\rangle$ state, marked by an ellipse. The splitting of the hyperfinestates at $B = 0G$ is shown on the left side of the figure.*

(b), it is quite obvious, that the magnetic field should be larger than 18G (the larger, the better), to avoid a resonance of σ^- polarized light, which leads to depolarization effects.

The transitions of σ^- polarized light, pumping the $F = 2$ manifold are shown in fig. 6.7 (d). In order to reduce depolarization effects, the magnetic field should not exceed a value of 20G. The limits for the spin-polarization set by these discussions are consistent with fig. 6.7 (c), showing the σ^+ transitions of the $F = 2$ manifold pumping beam.

These plots suggest the use of a magnetic field of 20G and a frequency of the $F = 2$ pumping beam of 73MHz, which corresponds to a frequency of the umpump AOM of 65MHz. However the stability against polarization imperfections is not as high as for the $F = 1$ scheme. Also since the distance between pumping into the $F' = 2$ and $F' = 3$ manifold does not increase significantly, the optical density of the cloud is not expected to change compared to a zero field pumping scheme. The only advantage is that the σ^+ transition (c) is in resonance while σ^- light of the $F = 2$ pumping beam (d) is not.

After applying this scheme, no atoms in the $|F = 1, m_F = -1\rangle$ state are observed anymore. Also 90% of the atoms being trapped in the magnetic trap are occupying the $|F = 2, m_F = 2\rangle$ state. Only 10% are in the $|F = 2, m_F = 1\rangle$ state and we cannot detect any atoms in $|F = 2, m_F = 0\rangle$.

The $|F = 2, m_F = 1\rangle$ atoms are removed following the purification scheme of [67]. The trap bottom of the cloverleaf is lifted to $B_0 = 130$G, which results in a differential splitting of the $m_F = 2$ atoms with respect to the $m_F = 1$ atoms by 91MHz. This

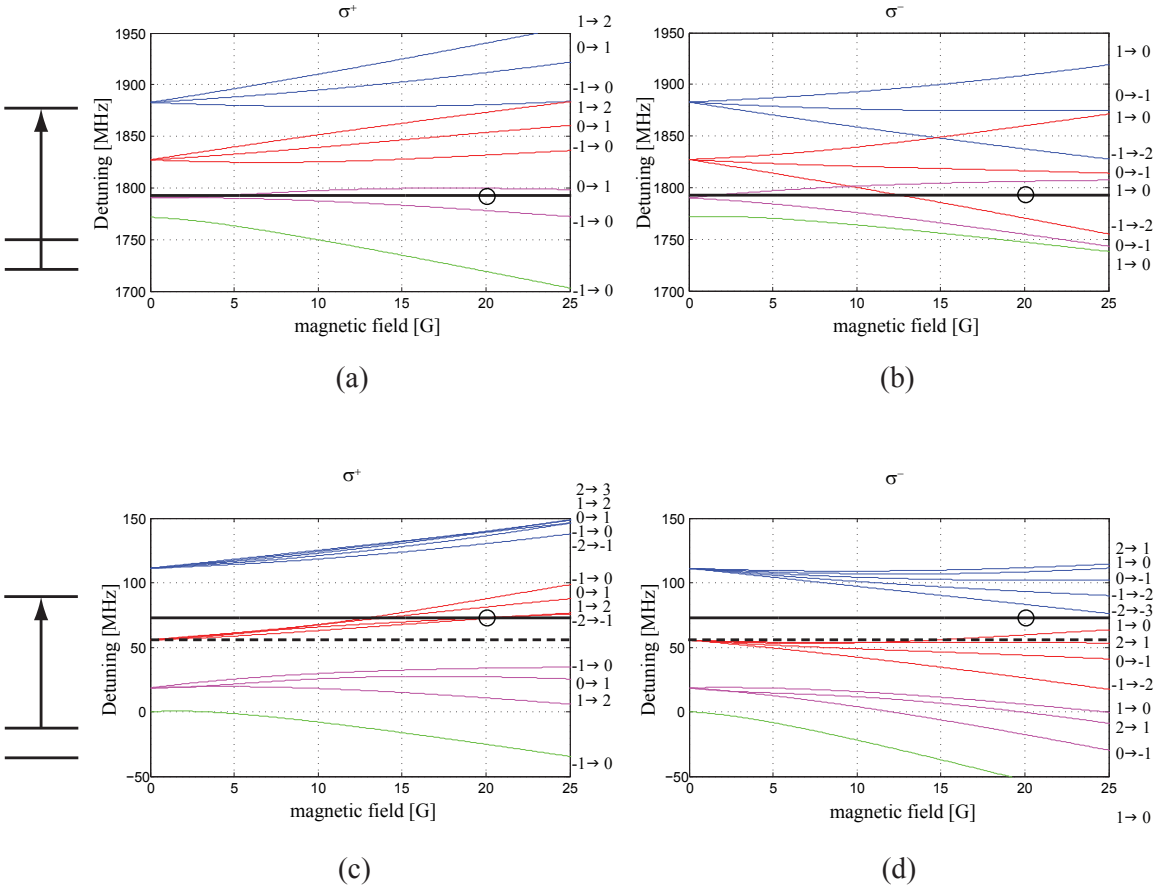

Figure 6.7.: *Spin-polarizing scheme when loading $|F = 2, m_F = 2\rangle$ atoms from the MOT into the magnetic trap. The detunings are given with respect to the $F = 1 \rightarrow F' = 0$ transition. The black line indicates the proposed frequency of the repumper (a&b) and umpump (c&d) light as indicated by the sketch on the left side of the figures. The color code displays the total spin quantum number F' of the atoms excited state. green, magenta, red, blue correspond to $F' = 0, 1, 2, 3$. On the right side of the figure the magnetic quantum numbers of the transitions are given. The quantum numbers labeling the states are given in the total spin quantum number basis at low fields. Fig. (a&c) depict the situation for σ^+ light and fig. (c&d) for σ^- light. The circle marks the magnetic field chosen, as explained in the text. The dashed line indicates the frequency of the umpump light at zero magnetic field, being resonant with both polarisations σ^+ and σ^-.*

splitting is larger than the width of both clouds in the magnetic trap due to their temperature. A microwave sweep is driven across the $m_F = 1$ sample, to transfer them into the untrapped $|F = 1, m_F = 0, 1\rangle$ states. In this way the magnetically trapped sample ends up to be completely in the $|F = 2, m_F = 2\rangle$ state.

Applying this scheme in the experiment results in an atom number increase of 2 and an increase in phase space density of 3 in the compressed magnetic trap after removing the $|F = 2, m_F = 1\rangle$ state, compared to a spin polarization pulse at $B = 0$G.

6.5. BEC in the Plugged Quadrupole Trap

The previous design of the experiment can be found in great detail in the diploma thesis of M. Repp [69], S. Weis [71], J. Krieger [70], A. Piccardo-Selg [63], R. Scelle [64], V. Volchkov [75] and B. Huber [58].

After loading a dark spot MOT, the atoms were transferred into the $F = 1$ manifold and the $|F = 1, m_F = -1\rangle$ state was trapped in a plugged quadrupole trap. The trap was compressed to the maximal gradient of $B' = 660$G/cm and microwave photons, resonant with the edge of the trap were shone in to cool the sample evaporatively. In a first cooling ramp, the trap depth was lowered to about 290μK within 5.6s. After weakening the trap confinement by adiabatically relaxing the gradient to $B' = 520$G/cm, a second cooling ramp of 500ms duration was applied. The final trap depth was 50μK. Lowering the trap confinement have had become necessary, since the high densities resulted in an increased inelastic loss rate which degraded the efficiency of evaporation.

Fig. 6.8 shows the column density of a BEC in the plugged quadrupole trap after an expansion time of 3ms. The red line is a bimodal fit to the experimental data (black). The data corresponds to approximately 4×10^5 atoms at a temperature of 2μK. The critical temperature for the trap is approximately $T_c \approx 3\mu$K. It is hard to determine T_c exactly, since the trapping frequencies eqs. (5.13) assume a plug that is centered onto the magnetic field zero of the quadrupole trap. Already a slight misalignement changes the trapping frequencies and therewith the critical temperature.

6.6. NaLi Unplugged: BEC in Cloverleaf Trap

The new design of the apparatus uses a cloverleaf trap to cool the atoms from the MOT into the BEC phase. A sequence diagram of the cooling cycle in the magnetic trap is shown in fig. 6.9, where the currents through the cloverleaf coils are depicted.

After a dark-spot MOT has been loaded in 5s, we apply a spin-polarizing pulse in order to pump most of the atoms into the desired $|F = 2, m_F = 2\rangle$ state. Therefore the dark spot repumper beam is turned off and we shine in the repumper beam as listed in table 6.1 to transfer the atoms in the dark region of the MOT within the 400μs repump section from the $F = 1$ into the $F = 2$ manifold. During the next 1.5ms, the umpump beam is added to complete the spin-polarizing scheme as described in

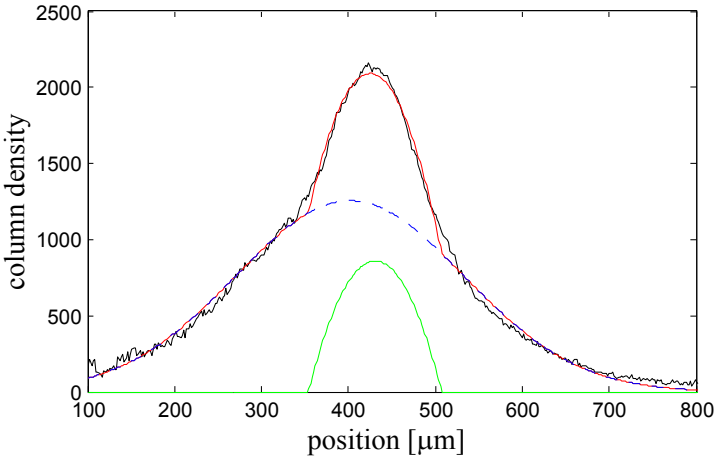

Figure 6.8.: *BEC in the plugged quadrupole trap after 3ms expansion time. The wings of the column density is fitted by a gaussians since it resembles the thermal background and he central BEC is fitted by a Thomas-Fermi profile. The blue dashed line is the fit to the thermal background, the green line the fit to the BEC and the red line the combined fit to the experimental data (black).*

section 6.4.

The magnetic trap is turned on using matched magnetic fields in order to conserve the phase space density $\mathfrak{D}$ of the MOT. During the purification step, the atoms remaining in the $|F = 2, m_F = 1\rangle$ state are removed as described earlier. After compressing the atomic cloud by increasing the confinement of the trap, we end up with a pure sample of $N = 5 \times 10^8$ atoms in the $|F = 2, m_F = 2\rangle$. Note that at this stage the cloverleaf is predominantly linear, since the temperature of the cloud (times k_B) is much larger than the magnetic field offset at the bottom of the trap (times μ_m).

Applying three different microwave ramps, increases the phase space density by 4.5 orders of magnitude, until inelastic collisions diminish the cooling efficiency due to an increased three-body loss. This can be seen in fig. 6.10, where the cooling efficiency bends over at the end of the second microwave ramp (red circles). In the next step, the trap confinement is weakened by opening the cloverleaf in radial direction and a final microwave ramp cools the sample into Bose-Einstein condensation.

The efficiency of the evaporative cooling ramp is determined by the total efficiency parameter γ_tot [76]:

$$\gamma_\mathrm{tot} = -\frac{\log_{10}(\mathfrak{D}_\mathrm{final}/\mathfrak{D}_\mathrm{initial})}{\log_{10}(N_\mathrm{final}/N_\mathrm{initial})}. \tag{6.6}$$

For a harmonic trap configuration as the used cloverleaf trap in our experiment, the evaporative cooling process is in the runaway regime if $\gamma_\mathrm{tot} > 2$. In this context runaway refers to the regime where the collision rate in the sample increases due to

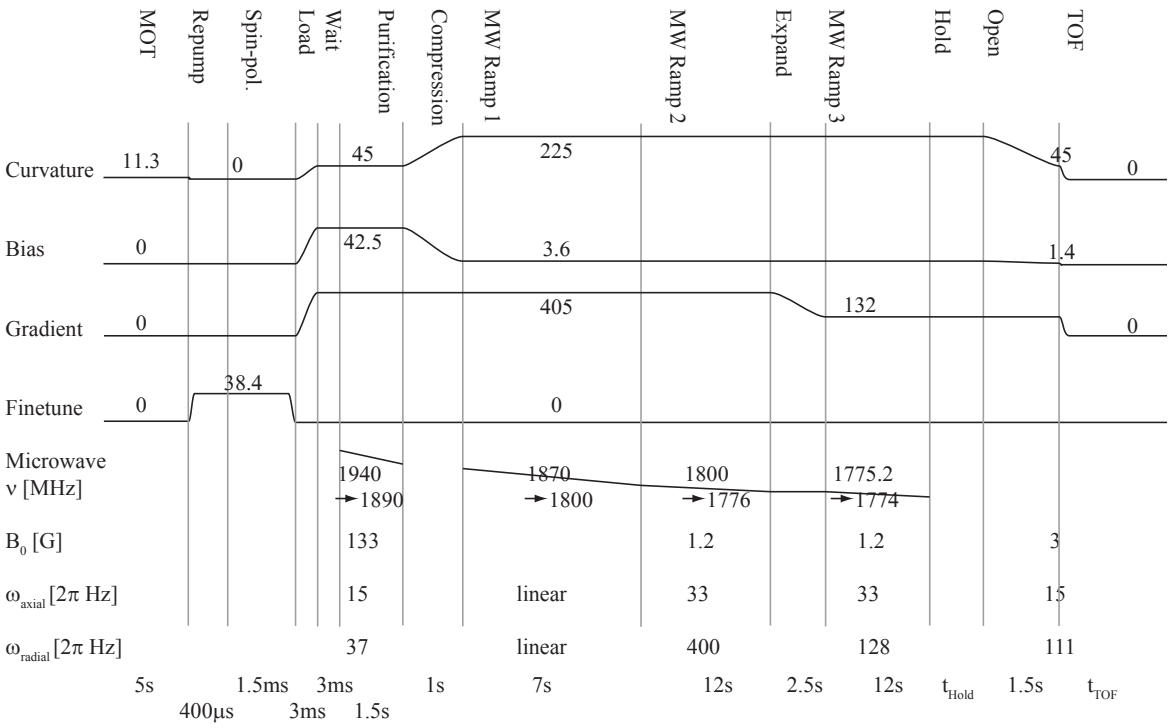

Figure 6.9.: *Sequence diagram of the magnetic trap and the mircowave frequency applied to achieve a BEC in the cloverleaf trap. The values at given at the ramp are the currents trough the cloverleaf trap provided by the different power supplies. The magnetic trap offset B_0 and resulting axial and radial trapping frequencies ω_{axial} and ω_{radial} are given as well as the duration of every step.*

an increasing density, although the total number of atoms is reduced by removing the high energy tail of the Maxwell-Boltzmann distribution. Collisions among the trapped atoms will redistribute the kinetic energy at a lower total energy—the sample cools down.

The total efficiency parameter for our experiment is shown is fig. 6.10, where the increase in phase space density (nominator of eq. (6.6)) is plotted versus the loss in atom number (denominator) during the applied microwave ramp. As the initial phase space density and atom number the values of the compressed magnetic trap are taken. The vertical lines indicate the positions where the microwave ramp changes. A fit to the data points yields a total efficiency parameter for our trap of $\gamma_{\mathrm{tot}} = 2.96$. The last points of the third microwave ramp correspond already to a Bose condensed cloud of sodium atoms.

A BEC of 4.7×10^4 atoms in the cloverleaf trap is shown in fig. 6.11. The number of thermal background atoms is 3.6×10^5 atoms, corresponding to a condensate fraction of 13%.

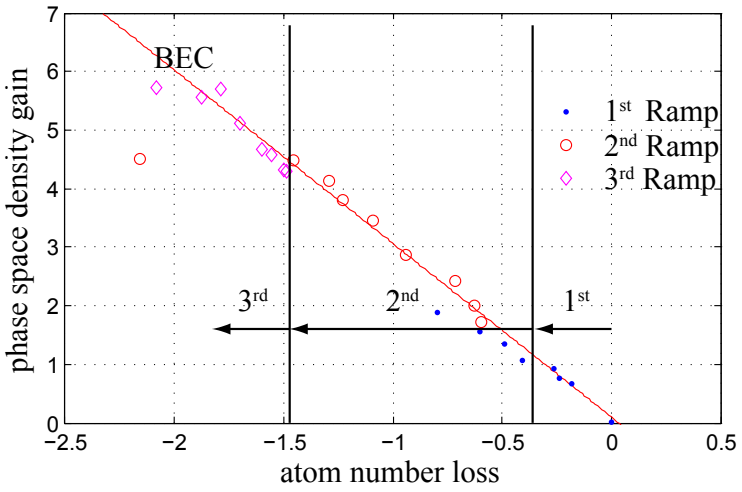

Figure 6.10.: *Phase space density increase (in orders of magnitude) as the atom number decreases (in orders of magnitude) during evaporation in the magnetic trap until the BEC phase is reached. The fit to the data points yields an efficiency factor of $\gamma_{tot} = 2.96$. The colors indicate the different microwave ramps used: First ramp at 10MHz/s (blue dots), second ramp at 2MHz/s (red circles) and the third ramp at 100kHz/s (magenta diamonds) after opening the magnetic trap to reduce three-body collisions.*

6.7. Dipole Trap

The dipole trap configuration consists of two focussed beams, that cross each other under an angle of 90°. One beam is sent trough the symmetry axis of the cloverleaf trap, the other one is in the plane perpendicular to that axis. The intensity profile of a focussed gaussian beam pointing along the z axis reads:

$$I(x,y,z) = I_0 \frac{w_0^2}{w(z)^2} \exp\left(-\frac{2(x^2+y^2)}{w(z)^2}\right) \tag{6.7}$$

where $w(z) = w_0\sqrt{1+z^2/z_\mathrm{R}^2}$ is the radius of the beam at a distance z from the waist $w(z=0) = w_0$ and $z_\mathrm{R} = \pi w_0^2/\lambda$ denotes the Rayleigh range. The intensity profile of the laser beam, leads to a potential where the atoms can be trapped. The trapping frequencies of a single beam trap read:

$$\omega_{x,y} = \sqrt{\frac{4|V_0|}{mw_0^2}} \qquad\qquad \omega_z = \sqrt{\frac{2|V_0|}{mz_\mathrm{R}^2}} \tag{6.8}$$

where $V_0 = V(r=0)$ is the depth of the dipole potential and is given by eq. (5.5):

$$V_0 = \underbrace{-\frac{3\pi c^2}{2\omega_0^3}\left(\frac{\Gamma}{\omega_0-\omega_\mathrm{L}} + \frac{\Gamma}{\omega_0+\omega_\mathrm{L}}\right)}_{\equiv\gamma} I_0 \tag{6.9}$$

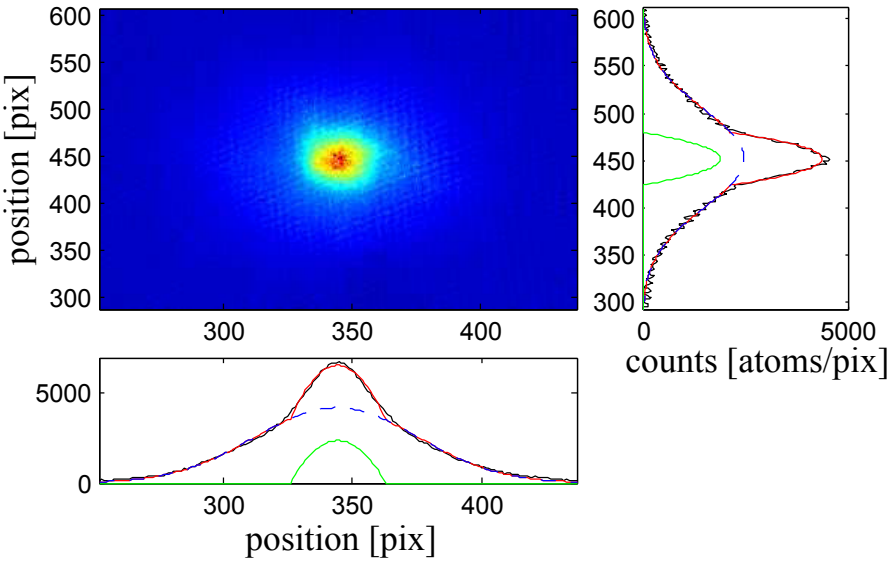

Figure 6.11.: *Bose-Einstein condensate of* 4.7×10^4 *atoms in the cloverleaf trap which corresponds to a condensate fraction of* 13%*. The 2D image is summed over one direction to obtain a 1D density profile in two different directions as indicated. The measured data is shown as a black line. The red line is a fit to the data points including a gaussian fit to the thermal background (blue dashed line) and a Thomas-Fermi profile fit to the condensate fraction (green). The amplitudes of the summed density profile is the atom number per effective pixel (pixelsize corrected by the magnification of* $M = 2.3$ *of the imaging system).*

where we have defined γ being the proportionality constant between the intensity profile and the resulting potential.

If we consider in the following a crossed dipole trap, created by two gaussian beams $I_1(r)$ and $I_2(r)$ with waists $w_{0,1}$ and $w_{0,2}$ and peak intensities $I_{0,1}$ and $I_{0,2}$, intersecting under an angle of 90° as depicted in fig. 6.12, the resulting potential can be approximated by:

$$V_{\text{crossed}}(x,y,z) = \gamma(I_{0,1}+I_{0,2})\left[1-\left(\frac{2I_{0,1}}{w_{0,1}^2}+\frac{2I_{0,2}}{w_{0,2}^2}\right)x^2-\left(\frac{I_{0,1}}{z_{\text{R},1}^2}+\frac{2I_{0,2}}{w_{0,2}^2}\right)y^2 - \left(\frac{2I_{0,1}}{w_{0,1}^2}+\frac{I_{0,2}}{z_{\text{R},2}^2}\right)z^2-\mathcal{O}(x,y,z)^4\right]. \tag{6.10}$$

$z_{\text{R},1}$ and $z_{\text{R},2}$ are the corresponding Rayleigh ranges of the beam. The resulting

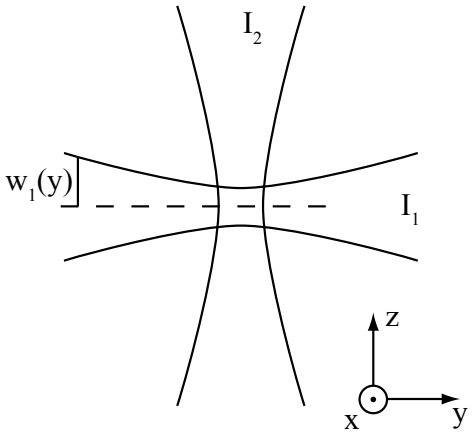

Figure 6.12.: *Sketch of the crossed dipole trap setup with an coordinate system to define the axis.*

trapping frequencies of the potential are:

$$\omega_x^2 = \frac{2\gamma}{m}\left(\frac{2I_{0,1}}{w_{0,1}^2} + \frac{2I_{0,2}}{w_{0,2}^2}\right) \tag{6.11a}$$

$$\omega_y^2 = \frac{2\gamma}{m}\left(\frac{I_{0,1}}{z_{\mathrm{R},1}^2} + \frac{2I_{0,2}}{w_{0,2}^2}\right) \tag{6.11b}$$

$$\omega_z^2 = \frac{2\gamma}{m}\left(\frac{2I_{0,1}}{w_{0,1}^2} + \frac{I_{0,2}}{z_{\mathrm{R},2}^2}\right) \tag{6.11c}$$

If both trapping beams have equal powers and equal waists, the terms proportional to $1/z_{\mathrm{R}}^2$ can be neglected, since $z_{\mathrm{R}} \gg w_0$ besides the beam waist is on the order of the wavelength $w_0 \sim \lambda$.

In order to load the atomic sample efficiently into the optical dipole trap, it needs to match the trapping conditions of the cooled cloverleaf trap. The critical temperature for Bose-Einstein condensation of 1×10^7 atoms in a harmonic trap with $\overline{\omega} = 2\pi \times (300 \times 300 \times 15)^{1/3} = 2\pi \times 110\mathrm{Hz}$, which corresponds approximately to a relaxed cloverleaf trap to reduce the 3-body collisions, is $T_c = 1\mu\mathrm{K}$. If we assume loading the cloud at $T = 2 \times T_c$, the trap depth should be at least $10\mu\mathrm{K}$ to transfer most of the atoms.

A possible scheme for the dipole trap at $\lambda = 1064\mathrm{nm}$ would be: using a modified crossed beam setup with a waist of $w_0 = 60\mu\mathrm{m}$ each. One beam (I_1 in fig. 6.12) is only focussed along the z direction, whereas the second beam is focussed in x and y direction. The resulting trapping frequency and trap depth for equal powers in both beams is plotted in fig. 6.13. Due to the long Rayleigh range of the beams of $z_{\mathrm{R}} = 10.6\mathrm{mm}$, the trapping frequencies of such a trap are equal in all three dimensions. Installing the beams such, that the z axis overlaps with the symmetry axis of the cloverleaf trap, allows a mode-matching just by changing the powers of the beams.

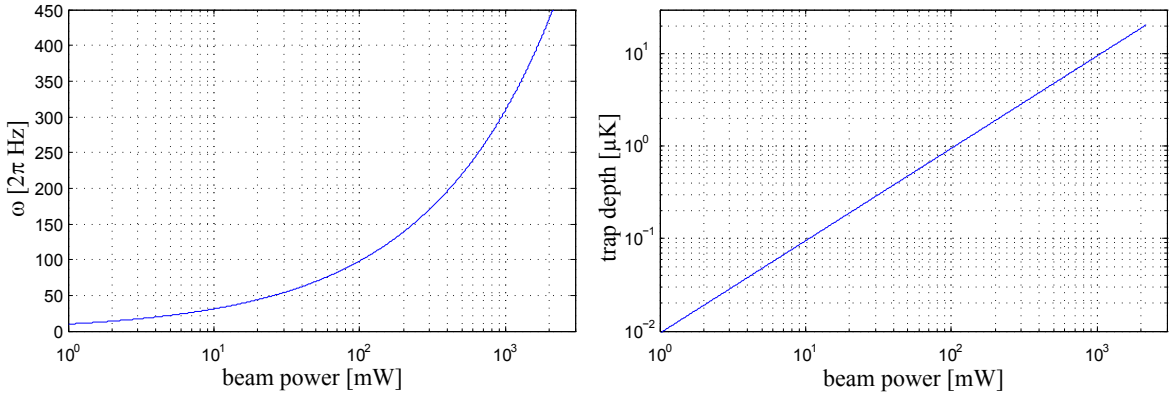

(a) **(b)**

Figure 6.13.: *Trap frequency (a) and trap depth (b) of a crossed beam trap with equal waists of $w_0 = 60\mu m$, where one of the beams is only focused in one dimension (z-axis) but the other is focused in x and y direction. The power in both beams is assumed to be equal.*

Moreover, using equal powers in both beams reveals a spherically symmetric trapping geometry.

We use a Nd:YAG laser (*IBL, DiNY cwQ 100*), emitting a TEM_{00} mode with a center wavelength of $\lambda = 1064$nm and a linewidth of 0.4nm. It provides a maximum output power of 50W. The beam is split into two paths, each of them passing an AOM with frequencies of $\pm$80MHz and then being coupled to a single mode fiber (*Nufern PM980-HP*). The fibers are cleaved, self-cut and hold by micro-positioning stages. Microscope objectives are used to focus the light onto the fiber core. In this way we are not limited by the standard fiber connectors, which degrade the coupling efficiency at high powers. Light being coupled to the cladding would heat up the epoxy, used to glue the fiber end into the connector. At high intensities, this epoxy gets melted and the emerging dust particles settle on the fiber facet and get burned into the tip.

7. Conclusion and Outlook

This thesis deals with understanding the polaron concept in the context of ultracold atomic samples and describes the status of an experimental setup to study immersed quantum systems in the lab. In the first part of the thesis the theoretical framework to understand the behavior of dilute atomic gases at degeneracy is given. The condensed matter concept of a polaron – an electron moving through an ionic crystal lattice thereby interacting with the lattice excitations – is extended to the framework of cold gases. We contrast mean-field calculations giving an intuitive picture of the ongoing physics to the many-body quantum mechanical treatment of Tempere *et al.* [42].

In the case of an impurity atom interacting with a degenerate bosonic background gas, the polaron, can be described as the impurity interacting with the excitation spectrum of the BEC background, namely the Bogoliubov modes. The excitation spectrum of these modes behaves linearly for small momentum[1] $k < \hbar/\xi$ and evolves into a quadratic dispersion relation for $k > \hbar/\xi$. As long as only the low lying excitation modes of the condensate are addressed by the interaction of the impurity atom with the background, the situation is analog to a condensed matter polaron interacting with acoustic phonons of the ionic crystal lattice.

This analog motivated a study of the cold gases polaron using a many-body treatment applied in condensed matter context [42]. In order to understand this many-body treatment more detailed, a mean-field simulation of the cold gases polaron is presented within this work. The results of the simulation allow to draw the following picture of the situation as the interaction between the impurity atom and the background BEC is varied: At low interaction strengths the impurity atom is not influenced by the presence of the background BEC. As the interaction is increased, the presence of the impurity starts to modify the background gas up to the point where the impurity starts to bury a hole in the backgound density. As soon as this hole is deep enough to support a bound state, the impurity is completely trapped in this self-consistent potential—it is self-trapped in the background BEC. This localization is in analogy to the strong coupling regime of the condensed matter polaron, where the electron is located at a single site of the ionic crystal lattice due to the strong interaction with the lattice phonons.

The localization in the background BEC is associated with a strong increase of the effective mass of the impurity atom. This is a quantity that can be measured in an experiment by observing the oscillation modes of the impurity. Using state-selective dipole potentials, the ^{6}Li impurity can be trapped within a background BEC of ^{23}Na

[1] Here ξ is the healing length, a characteristic length scale of the background gas over which disturbances of the BEC can "heal".

and the effective mass of the impurity can be deduced directly.

In the second part of the thesis, the setup of an experiment to cool bosonic ^{23}Na and fermionic ^{6}Li into quantum degeneracy is described. The theoretical framework of trapping neutral atoms is derived and two magnetic trap configurations, the plugged quadrupole trap as well as the cloverleaf trap, are presented. The trap configurations are compared to each other with respect to their possibility to cool two atomic species into quantum degeneracy.

A reference measurement of the loading of a magneto-optical trap is presented and a Bose-Einstein condensate of ^{23}Na is achieved in the plugged quadrupole trap as well as in the cloverleaf trap. The current setup of the experiment uses the cloverleaf configuration. A modified spin-polarization scheme is discussed and the setup of the optical dipole trap is outlined, which will allow the use of magnetically induced Feshbach resonances.

Outlook

The next steps of the experiment will be the setup of the optical dipole trap and the Bose-Einstein condensation of sodium atoms therein. With this configuration, the magnetic tunability of the energy splitting between two magnetic substates of the sodium BEC can be used to determine the magnetic field stability of the Feshbach fields. A possible issue using sodium Feshbach resonances will involve to study d-wave or g-wave resonances, which can be calculated using the Moerdijk model [33]. These should occur at accessible magnetic field values of our experiment. A further possibility will be to study microwave induced Feshbach resonances, where sodium seems to be the ideal candidate [35]. Here a microwave field couples the colliding atoms in the open channel resonantly to a bound state in a closed channel of the scattering potential. These resonances could also be used in later polaron experiments in order to increase the experimentally accessible range of the polaron coupling constant $\alpha = a_{\mathrm{IB}}^2/\xi a_{\mathrm{BB}}$. The interparticle scattering length a_{IB} can be tuned by a magnetic Feshbach resonance and the microwave control can be used to tune a_{BB} at the same time independently. By adding sympathetically cooled lithium to the experiment, the study of polaron physics using single impurities will be of interest. As suggested by the mean-field calculations presented in this thesis, the strong coupling regime of the impurity-background interaction should be in reach. This regime is not accessible in condensed matter systems due to the lack of materials supporting such a strong electron-phonon coupling. Also phase-separation and mixing of two distinct species can be studied.

Another possible issue would be to use the immersed species as a local probe of properties of the background gas. E.g. a dilute sodium gas can serve as a thermometer for a degenerate gas of fermionic lithium [47], or a localized impurity gas immersed in a large background could be used to measure the drag force on the background gas when moving the impurities through the background. Such an experiment would probe the viscosity of the background gas locally and could be used to study the proposed lower

bound on the ratio of the shear viscosity to entropy density [77].

A. Sodium and Lithium Line Data

The following data are taken from [78] in the case of sodium and [79] in the case of lithium. The hyperfine structure splitting in an external magnetic field of the ground states of both elements have been calculated using the Breit-Rabi formula.

^{23}Na

The Breit-Rabi diagram showing the hyperfine states of the ^{23}Na $3^2S_{1/2}$ state is shown in fig. A.1. The states are labeled in the $|F, m_F\rangle$ basis. The state numbering as used for instance in table 4.1 is shown on the right site. The states are labeled in increasing order of energy.

Property		Value
Transition Frequency: $3^2S_{1/2} \rightarrow 3^2P_{3/2}$	ω_0	$2\pi \times 508.848\ 716\ 2(13)$THz
Natural Line Width (FWHM)	Γ	$2\pi \times 9.7946(46)$MHz
Recoil Velocity	v_r	2.9461 cm/s
Recoil Temperature	T_r	2.3998 μK
Doppler Temperature	T_D	235.03 μK
Saturation Intensity: $3^2S_{1/2} \rightarrow 3^2P_{3/2}$, $\lvert F = 2, m_F = 2\rangle \rightarrow \lvert F' = 3, m'_F = 3\rangle$	I_sat	6.2600(21) mW/cm^2

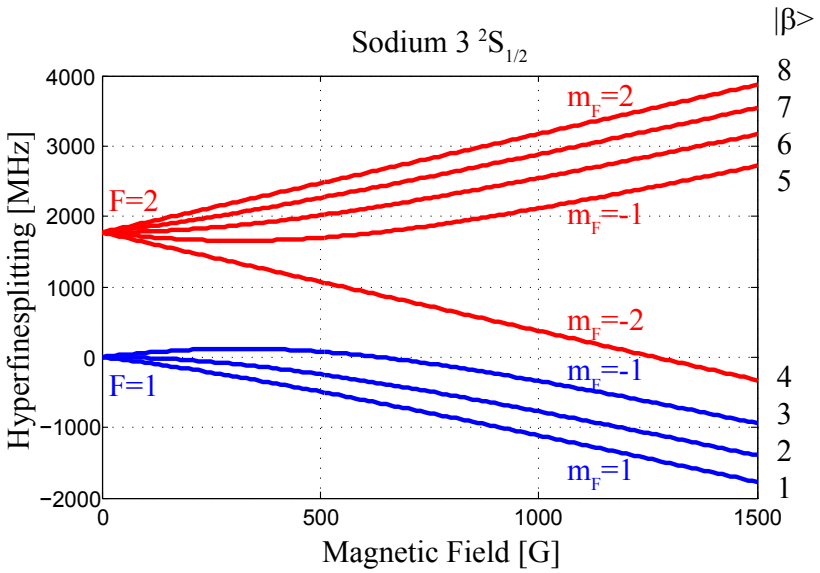

Figure A.1.: *Sodium 3 $^2S_{1/2}$ line data*

^{6}Li

The Breit-Rabi diagram showing the hyperfine states of the ^{6}Li $2^2S_{1/2}$ state is shown in fig. A.2. The states are labeled in the $|F, m_F\rangle$ basis. The state numbering as used for instance in table 4.1 is shown on the right site. The states are labeled in increasing order of energy.

Property		Value
Transition Frequency: $2^2S_{1/2} \rightarrow 2^2P_{3/2}$	ω_0	$2\pi \times 446.799\ 677$THz
Natural Line Width (FWHM)	Γ	$2\pi \times 5.8724$MHz
Recoil Velocity	v_r	9.886 776 cm/s
Recoil Temperature	T_r	3.535 811 52 μK
Doppler Temperature	T_D	140.9 μK
Saturation Intensity:	I_{sat}	2.54 mW/cm^2

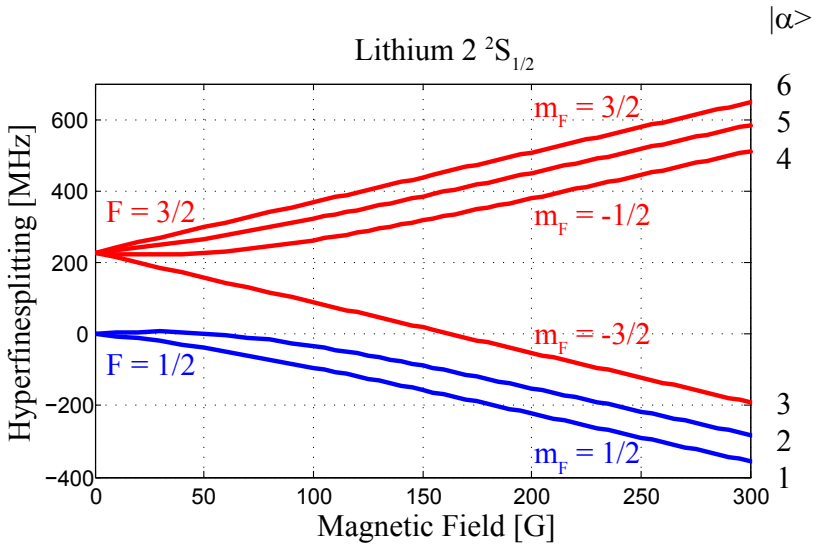

Figure A.2.: *Lithium 2* $^2S_{1/2}$ *line data*

B. Cloverleaf Design

The design goal of the cloverleaf trap is a high collision rate in the compressed trap. Once the trap is operated in the harmonic regime (i.e. $k_{\mathrm{B}}T \ll \mu_{\mathrm{m}}B$), the collision rate scales as the geometric mean of the three curvatures of the trap [21]: $(B''^2_\rho B''_z)^{1/3} \approx B'^{4/3}B''^{1/3}B_0^{-2/3}$, using eq. (5.16). From this consideration it is quite obvious, that a trap design should be optimized on high gradients, rather than strong curvatures. Also the offset field B_0 should be as small as possible, keeping in mind to apply a finite offset to prevent Majorana losses.

The magnetic field calculation was done as described in [80]. The trap setup should be located outside the vacuum setup, requiring high currents to achieve high values of B' and B''. The location of the individual coils is altered compared to other existing cloverleaf traps as operated in the Ketterle group at MIT [66], the Van der Straten group in Utrecht [81] or in the Thomsen group in Copenhagen [82].

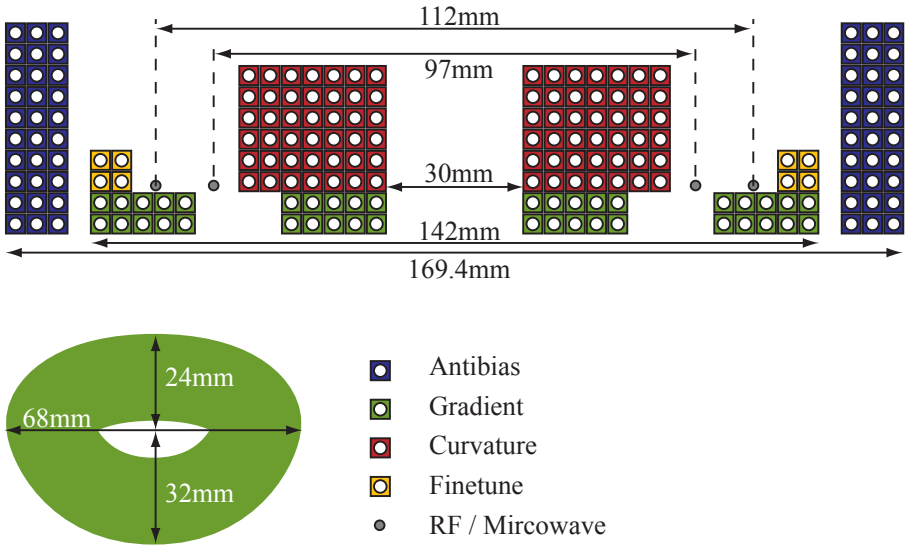

Figure B.1.: *Cut trough the the cloverleaf coils, to visualize the assembly of the individual coils. Also the dimensions of a single gradient coil is shown. We use a hollow core wire (inner diameter of 2.3mm) with outer dimensions of* (3.5×3.5)*mm.*

A schematic view on the coil design is presented in fig. B.1, where a cut through the center of the coils is shown. In this view the trap minimum is located below the sketch. The gradient coils (green) are placed as close to the atoms as possible in order to reduce the power consumption of those coils during operation. The antibias coils (blue) are placed in perfect Helmholtz configuration to achieve a high homogeneity over

the atomic samples to allow a precise tuning of the scattering length using Feshbach resonances, once the cooled cloud is loaded into the optical dipole trap. The curvature coils (red) produce the same offset field as the antibias coils at the trap center and are used to provide the axial harmonic confinement. Antibias and curvature coils are operated such, that their offset field in the center of the trap nearly vanishes. When operating the cloverleaf trap, both coils are run in series in order to increase the magnetic field stability, and thus noise of the power supply is just a common mode noise in the total magnetic field.

The finetune coils (yellow) are used to apply a homogeneous field for the spin-polarizing scheme of the atoms and to apply a magnetic field gradient for a Stern-Gerlach experiment (if only the coil in one holder is used). Also the rf and microwave antennas (grey) are included in the holders, thereby placing them as close as possible to the atomic sample. They consist of three wires each (diameter 1mm) and are connected in Helmholtz configuration. Note that the atoms are located in the near field of these antennas, even when using a microwave transition of 1771MHz which corresponds to a wavelength of $\lambda = 16.9$cm.

The hollow core copper wire used to wind the coils was manufactured by *Eugen Geyer GmbH*[1]. The outer dimensions are (3.5×3.5)mm and the inner core diameter is 2.3mm. These dimensions minimize the power dissipated in the wire per cooling surface, provided by the hollow core design. The coils are mounted into a holder made of PEEK[2] and glued using epoxy (*Rhenatech EP 5430*). This combination reduces the amount of non-metallic materials close to the trap center thereby avoiding eddy currents.

Water Cooling

During full operation of the magnetic trap, approximately 11.2kW of power are dissipated by the coils (antibias + curvature, 225A: 6.5kW, gradient, 440A: 4.7kW). When operating the antibias coils at a maximal current of 390A, which corresponds to a magnetic field of $B = 1250$G, 12.2kW are dissipated.

The cooling water, provided by a *EF Cooling* chiller, is flowing parallel through all the coils. We installed 5 flow meters, monitoring the water flow through: (i) the antibias coils in each holder seperately, (ii) the curvature, finetune and gradient coils in each holder seperately and (iii) the passbank, regulating the current when operating the antibias coils to use the Feshbach resonance.

Circuit Diagram

The circuit diagram of the cloverleaf trap is shown in fig. B.2. The power supplies used are listed in table B.1. We use several IGBTs to switch the coil setup for different stages of operation.

[1] www.geyer-gmbh.de
[2] polyether ether ketone

	Manufacturer	Type	U [V]	I [A]
antibias	Delta Elektronika	SM15-400*	16.5	400
	Agilent	6690A	15	440
curvature	Delta Elektronika	SM30-200*	30	225
gradient	Delta Elektronika	SM15-400*	15	440
finetune	Delta Elektronika	SM7.5-80	7.5	80
bias	Delta Elektronika	SM18-50	18	50

Table B.1.: *Power supplies used to operate the cloverleaf trap. All power supplies by Delta Elektronika are equipped with a high speed option. Both antibias power supplies are operated in series to extend the maximal achievable voltage. Power supplies marked with a * have an extended output range.*

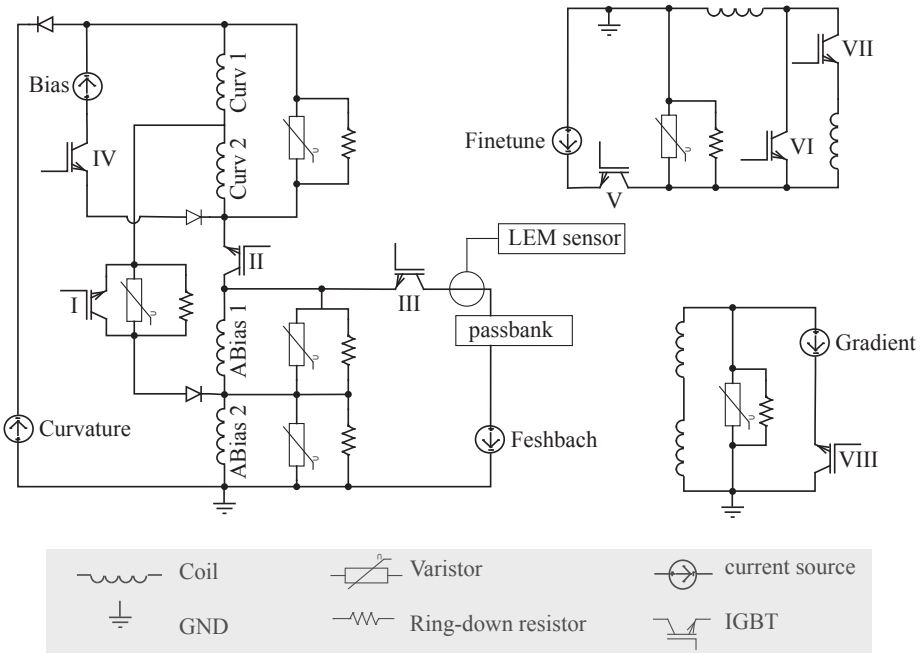

Figure B.2.: *Circuit diagram of the cloverleaf trap. The coils Curv1 and ABias1 are mounted together in one holder, whereas Curv2 and ABias2 are mounted in the second holder facing each other.*

During the MOT, IGBT I is conducting, whereas II, III and IV are not. The current provided by the curvature power supply will flow through the coils ABias2 and Curv1, thus producing the desired gradient field.

When switching to the magnetic trap configuration, IGBTs II and IV are conducting guiding the current through both antibias and curvature coils. The bias power supply can be used to add a current trough the curvature coils, thus lifting the magnetic field offset B_0 of the trap.

When the atoms are loaded into the optical dipole trap, IGBT III is conducting to apply a homogeneous field using the antibias coils. IGBTs I, II, IV and VIII are in the non-conducting state now. The current regulation of the antibias power supplies is done using a current sensor *LEM IT600-S* and a parallel circuit of 32 *IRF250* MOSFETs. This current regulation scheme is described in detail in [63]. The new setup differs only by the use of MOSFETs instead of NPN transistors, since they should provide a lower current noise, and the use of more devices in parallel to handle the increased dissipated power due to the changed coil setup.

The IGBTs VI and VII can be used to circumvent one coil of the finetunes in order to produce a field gradient over the atomic cloud. Varistors and 100Ω ring-down resistors are used to limit the maximum induced voltage when turning off the current and to dissipate the energy deposited in the magnetic field into the resistors. The minimum switching time of the antibias coils is limited by their inductance to $\tau = 3.7$ms. For faster magnetic field ramps the finetune coils can be used, having a inductance limited time constant of $\tau = 0.5$ms.

C. Interlock

The interlock system of the NaLi experiment is divided into two parts according to the water cooling scheme of the experiment—a clean circuit and a service water circuit. Water sensors installed at several places of the lab monitor for water leaks and turn off the water supply if necessary, thereby switching off all high current power supplies—magnetic trap, Feshbach field, Zeemann Slower. Both interlocks are described in the following.

C.1. Service Water Circuit

Devices cooled by the Service Water circuit are:

- decreasing and increasing part of the Zeeman Slower
- current regulation of the offset coils
- Passbank for the current regulation of the Feshbach fields
- heat sink for the clean water circuit
- RF and microwave amplifiers
- IGBT's and power diodes
- dye circulators of the two ring-dye lasers
- cold spot and oven baffle[1]

The temperature of the Zeeman Slower is monitored using 2kΩ thermistors plugged into a micro-controller (*Arduino Diecimila*). If the temperature exceeds a certain threshold, the Slower power supplies are shut down. A low pass filter prevents the interlock from triggering to any induced voltages. The interlock is also triggered if the water supply is cut manually at the labs magnetic valve.

[1]The oven nozzle is heated to $\approx 500°C$ to prevent sodium and lithium to get stuck, but the oven baffle is cooled in order to reduce the background pressure and force sodium and lithium to get stuck there. An additional cold spot cooled with peltier elements is installed to support this effect.

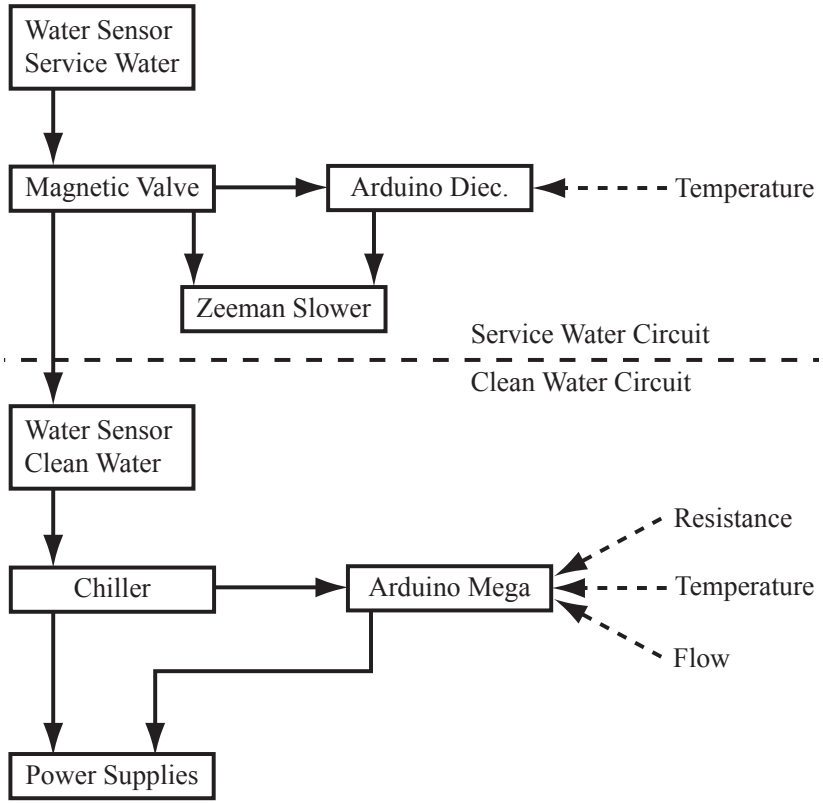

Figure C.1.: *Sketch of the Interlock system: As described in the text, the interlock scheme is divided into a service water circuit and a clean water circuit. The dashed lines depict the input signals to the micro-controller and the solid lines the signal logic at the different elements of the scheme.*

C.2. Clean Water Circuit

The clean water circuit is run by a chiller of *EF-Cooling* and cools all the coils of the cloverleaf trap. It provides a temperature stability of 1 degree and a pressure of 10 bar at a maximal flow of 25 l/min. The cooling capacity is 20kW.

The interlock system of the cloverleaf trap monitors several signals using an *Arduino Mega* micro-controller. The signals are:

- The temperature of the cloverleaf coils at 5 positions over both coils. The temperatures are measured close to the antibias (3 thermistors in total) and the curvature (2 thermistors in total) coils.
- The resistance of the gradient coils and the curvature + antibias coils during the magnetic trap phase is monitored using the analog monitor outputs of the corresponding *Delta Elektronika* power supplies.
- The water flow through the coils is monitored using flow meters.

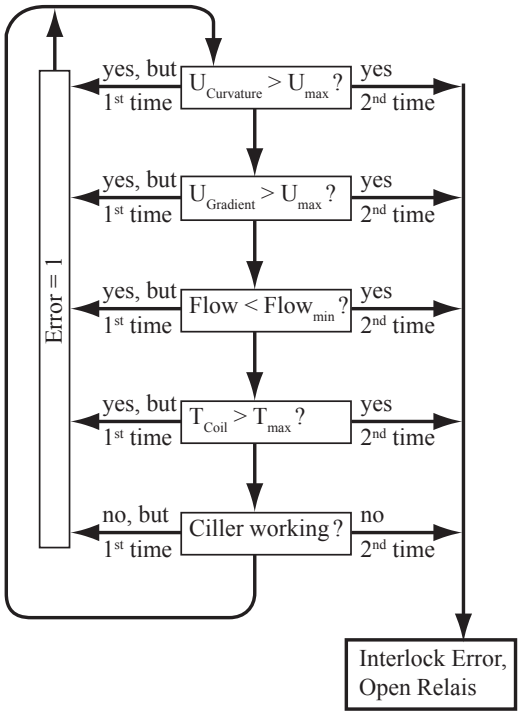

Figure C.2.: *Internal logic of the micro-controller* Arduino Mega *used to monitor the cloverleaf coils. The interlock registers an error if the corresponding signal is dc, such that small spikes are filtered by the logics. A relais is used to shut the power supplies down in case of an error.*

If one of those monitor signals deviates from its specified value or the chiller fails for some reason the power supplies are turned off. The switching logic of the micro-

	Pin	LED
Temperature	Temp. Pin 0	8
	Temp. Pin 1	7
	Temp. Pin 2	10
	Temp. Pin 3	9
	Temp. Pin 4	5
Water flow	Flow Pin 0	2
	Flow Pin 1	1
	Flow Pin 2	4
	Flow Pin 3	3
	Flow Pin 4	6
Resistance	R Pin 0	14
	R Pin 1	13
	R Pin 2	16

Table C.1.: *Assignment of the alart LED's of the* Arduino Mega *micro-controller. The corresponding pins are listed in fig. C.3.*

controller is depicted in fig. C.2. The input ports are low passed and also the micro-controller logic is programmed such, that short spikes in the monitor signal do not lead to an error event. Such spikes can occur when switching the magnetic fields at high speed.

A sketch of the interlock scheme is depicted in fig. C.1 and the pin assignment in fig. C.3. The corresponding LED's that monitor the status of the interlock are listed in table C.1.

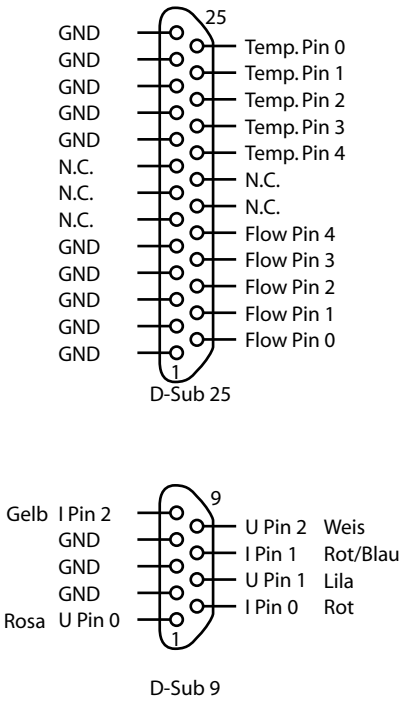

Figure C.3.: *Connection diagramm for the cloverleaf interlock. To monitor the temperature,* KTY 81-210 *thermistors are used as a variable resistor to GND. The Flow pins are the input signals of the flow meters and the monitor signals of the power supplies are connected to the d-sub 9 plug. All signals have a full range of 0V to 5V.*

Bibliography

[1] K. B. Davis, M. O. Mewes, M. R. Andrews, N. J. van Druten, D. S. Durfee, D. M. Kurn, and W. Ketterle. Bose-Einstein Condensation in a Gas of Sodium Atoms. *Phys. Rev. Lett.*, **75**(22):3969–3973, 1995.

[2] M. H. Anderson, J. R. Ensher, M. R. Matthews, C. E. Wieman, and E. A. Cornell. Observation of Bose-Einstein Condensation in a Dilute Atomic Vapor. *Science*, **269**:198, 1995.

[3] M. R. Andrews, C. G. Townsend, H.-J. Miesner, D. S. Durfee, D. M. Kurn, and W. Ketterle. Observation of Interference Between Two Bose Condensates. *Science*, **275**:637, 1997.

[4] M. Albiez, R. Gati, J. Fölling, S. Hunsmann, M. Cristiani, and M. K. Oberthaler. Direct Observation of Tunneling and Nonlinear Self-Trapping in a single Bosonic Josephson Junction. *Phys. Rev. Lett.*, **95**:010402, 2005.

[5] M. Greiner, O. Mandel, T. Esslinger, T. W. Hänsch, and I. Bloch. Quantum phase transition from a superfluid to a Mott insulator in a gas of ultracold atoms. *Nature*, **415**:39, 2002.

[6] Cindy A. Regel, Christopher Ticknor, John L. Bohn, and Deborah S. Jin. Creation of ultracold molecules from a Fermi gas of atoms. *Nature*, **424**:47–50, 2003.

[7] S. Jochim, M. Bartenstein, A. Altmeyer, G. Hendl, S. Riedl, C. Chin, J. Hecker Denschlag, and R. Grimm. Bose-Einstein Condensation of Molecules. *Science*, **302**(5653):2101–2103, 2003.

[8] M. W. Zwierlein, C. A. Stan, C. H. Schunck, S. M. F. Raupach, S. Gupta, Z. Hadzibabic, and W. Ketterle. Observation of Bose-Einstein Condensation of Molecules. *Phys. Rev. Lett.*, **91**(25):250401, Dec 2003.

[9] Markus Greiner, Cindy A. Regal, and Deborah S. Jin. Emergence of a molecular Bose-Einstein condensate from a Fermi gas. *Nature*, **426**:537–540, 2003.

[10] S. Inouye, M. R. Andrews, J. Stenger, H.-J. Miesner, D. M. Stamper-Kurn, and W. Ketterle. Observation of Feshbach resonances in a Bose-Einstein condensate. *Nature*, **392**:151–154, 1998.

[11] C. A. Stan, M. W. Zwierlein, C. H. Schunck, S. M. F. Raupach, and W. Ketterle. Observation of Feshbach Resonances between Two Different Atomic Species. *Phys. Rev. Lett.*, **93**(14):143001, 2004.

[12] S. Inouye, J. Goldwin, M. L. Olsen, C. Ticknor, J. L. Bohn, and D. S. Jin. Observation of Heteronuclear Feshbach Resonances in a Mixture of Bosons and Fermions. *Phys. Rev. Lett.*, **93**(18):183201, 2004.

[13] Kenneth Günter, Thilo Stöferle, Henning Moritz, Michael Köhl, and Tilman Esslinger. Bose-Fermi Mixtures in a Three-Dimensional Optical Lattice. *Phys. Rev. Lett.*, **96**(18):180402, 2006.

[14] S. Ospelkaus, C. Ospelkaus, O. Wille, M. Succo, P. Ernst, K. Sengstock, and K. Bongs. Localization of Bosonic Atoms by Fermionic Impurities in a Three-Dimensional Optical Lattice. *Phys. Rev. Lett.*, **96**(18):180403, 2006.

[15] J. Stenger, S. Inouye, D. M. Stamper-Kurn, H.-J. Miesner, A. P. Chikkatur, and W. Ketterle. Spin domains in ground state spinor Bose-Einstein condensates. *Nature*, **396**:345–348, 1998.

[16] J. Bardeen, L. N. Cooper, and J. R. Schrieffer. Theory of Superconductivity. *Phys. Rev.*, **108**(5):1175–1204, 1957.

[17] A. S. Alexandrov and N. F. Mott. High Temperature Superconductors and other Superfluids. Taylor & Francis, London, 1994. ISBN: 0-7484-0309-4.

[18] H. Fröhlich. Electrons in lattice fields. *Adv. Phys.*, **3**(11):325–361, 1954.

[19] Anthony J. Leggett. Bose-Einstein condensation in the alkali gases: Some fundamental concepts. *Rev. Mod. Phys.*, **73**(2):307–356, 2001.

[20] Franco Dalfovo, Stefano Giorgini, Lev P. Pitaevskii, and Sandro Stringari. Theory of Bose-Einstein condensation in trapped gases. *Rev. Mod. Phys.*, **71**(3):463–512, 1999.

[21] W. Ketterle, D. S. Durfee, and D. M. Stamper-Kurn. Making, probing and understanding Bose-Einstein condensates. In *Bose-Einstein condensation in atomic gases*, Proceedings of the International School of Physics "Enrico Fermi", Course CXL, pages 67–176, 1999.

[22] Stefano Giorgini, Lev P. Pitaevskii, and Sandro Stringari. Theory of ultracold atomic Fermi gases. *Rev. Mod. Phys.*, **80**(4):1215–1274, 2008.

[23] W. Ketterle and M. W. Zwierlein. Making, probing and understanding ultracold Fermi gases. *Rivista del Nuovo Cimento*, **81**:247–442, 2008.

[24] Franz Schwabl. Statistische Mechanik. Springer-Verlag Berlin Heidelberg, 3 2000. ISBN-13: 9783540671589.

[25] Torsten Fließbach. Statistische Physik: Lehrbuch zur Theoretischen Physik IV. Spektrum Akademischer Verlag, 2006. ISBN-13: 9783827416841.

[26] Franz Schwabl. Quantenmechanik. Springer, 2004. ISBN-13: 9783540431060.

[27] Cheng Chin, Rudolph Grimm, Paul Julienne, and Eite Tiesinga. Feshbach Resonances in Ultracold Gases. *e-print cond.mat/0812.1496v2*, 2009.

[28] Ph. Courteille, R. S. Freeland, D. J. Heinzen, F. A. van Abeelen, and B. J. Verhaar. Observation of a Feshbach Resonance in Cold Atom Scattering. *Phys. Rev. Lett.*, **81**(1):69–72, 1998.

[29] J. Cubizolles, T. Bourdel, S. J. J. M. F. Kokkelmans, G. V. Shlyapnikov, and C. Salomon. Production of Long-Lived Ultracold Li_2 Molecules from a Fermi Gas. *Phys. Rev. Lett.*, **91**(24):240401, 2003.

[30] S. Jochim, M. Bartenstein, A. Altmeyer, G. Hendl, C. Chin, J. Hecker Denschlag, and R. Grimm. Pure Gas of Optically Trapped Molecules Created from Fermionic Atoms. *Phys. Rev. Lett.*, **91**(24):240402, 2003.

[31] Kevin E. Strecker, Guthrie B. Partridge, and Randall G. Hulet. Conversion of an Atomic Fermi Gas to a Long-Lived Molecular Bose Gas. *Phys. Rev. Lett.*, **91**(8):080406, 2003.

[32] K. Xu, T. Mukaiyama, J. R. Abo-Shaeer, J. K. Chin, D. E. Miller, and W. Ketterle. Formation of Quantum-Degenerate Sodium Molecules. *Phys. Rev. Lett.*, **91**(21):210402, 2003.

[33] A. J. Moerdijk, B. J. Verhaar, and A. Axelsson. Resonances in ultracold collisions of ^{6}Li, ^{7}Li, and ^{23}Na. *Phys. Rev. A*, **51**(6):4852–4861, 1995.

[34] M. Theis, G. Thalhammer, K. Winkler, M. Hellwig, G. Ruff, R. Grimm, and J. Hecker Denschlag. Tuning the Scattering Length with an Optically Induced Feshbach Resonance. *Phys. Rev. Lett.*, **93**(12):123001, 2004.

[35] D. J. Papoular, G. V. Shlyapnikov, and J. Dalibard. Microwave-induced Fano-Feshbach resonances. *Phys. Rev. A*, **81**(4):041603, 2010.

[36] Dominik M. Bauer, Matthias Lettner, Christoph Vo, Gerhard Rempe, and Stephan Dürr. Control of a magnetic Feshbach resonance with laser light. *Nat. Phys.*, **5**:339–342, 2009.

[37] A. M. Kaufman, R. P. Anderson, Thomas M. Hanna, E. Tiesinga, P. S. Julienne, and D. S. Hall. Radio-frequency dressing of multiple Feshbach resonances. *Phys. Rev. A*, **80**(5):050701, 2009.

[38] E. P. Gross. Structure of a Quantized Vortex in Boson Systems. *Nuovo Cimento*, **20**:45, 1961.

[39] L. P. Pitaevskii. Vortex Lines in an Imperfect Bose Gas. *Sov. Phys. JETP*, **13**:451, 1961.

[40] N. N. Bogoliubov. On the Theory of Superfluidity. *Journal of Physics*, **11**:23–32, 1947.

[41] Jozef T. Devreese and Alexandre S. Alexandrov. Fröhlich polaron and bipolaron: recent developments. *Rep. Prog. Phys.*, **72**(6):066501 (52pp), 2009.

[42] J. Tempere, W. Casteels, M. K. Oberthaler, S. Knoop, E. Timmermans, and J. T. Devreese. Feynman path-integral treatment of the BEC-impurity polaron. *Phys. Rev. B*, **80**(18):184504, 2009.

[43] F. M. Peeters and J. T. Devreese. Acoustical polaron in three dimensions: The ground-state energy and the self-trapping transition. *Phys. Rev. B*, **32**(6):3515–3521, 1985.

[44] André Schirotzek, Cheng-Hsun Wu, Ariel Sommer, and Martin W. Zwierlein. Observation of Fermi Polarons in a Tunable Fermi Liquid of Ultracold Atoms. *Phys. Rev. Lett.*, **102**(23):230402, 2009.

[45] S. Nascimbène, N. Navon, K. J. Jiang, L. Tarruell, M. Teichmann, J. McKeever, F. Chevy, and C. Salomon. Collective Oscillations of an Imbalanced Fermi Gas: Axial Compression Modes and Polaron Effective Mass. *Phys. Rev. Lett.*, **103**(17):170402, 2009.

[46] Tin-Lun Ho. Universal Thermodynamics of Degenerate Quantum Gases in the Unitarity Limit. *Phys. Rev. Lett.*, **92**(9):090402, 2004.

[47] S. Nascimbène, N. Navon, K. J. Jiang, F. Chevy, and C. Salomon. Exploring the thermodynamics of a universal Fermi gas. *Nature*, **463**:1057–1060, 2010.

[48] Frédéric Chevy. Swimming in the Fermi sea. *Physics*, **2**:48, 2009.

[49] Christophe Mora and Frédéric Chevy. Ground state of a tightly bound composite dimer immersed in a Fermi sea. *Phys. Rev. A*, **80**(3):033607, 2009.

[50] M. Punk, P. T. Dumitrescu, and W. Zwerger. Polaron-to-molecule transition in a strongly imbalanced Fermi gas. *Phys. Rev. A*, **80**(5):053605, 2009.

[51] R. Combescot and S. Giraud. Normal State of Highly Polarized Fermi Gases: Full Many-Body Treatment. *Phys. Rev. Lett.*, **101**(5):050404, 2008.

[52] Paul L. DeVries. Application of the Split Operator Fourier Transform method to the solution of the nonlinear Schrödinger equation. *AIP Conf. Proc.*, **160**(1):269–271, 1987.

[53] H. Pu and N. P. Bigelow. Properties of Two-Species Bose Condensates. *Phys. Rev. Lett.*, **80**(6):1130–1133, 1998.

[54] Ryan M. Kalas and D. Blume. Interaction-induced localization of an impurity in a trapped Bose-Einstein condensate. *Phys. Rev. A*, **73**(4):043608, 2006.

[55] Marko Gacesa, Philippe Pellegrini, and Robin Côté. Feshbach resonances in ultracold ^{6,7}Li+^{23}Na atomic mixtures. *Phys. Rev. A*, **78**(1):010701R, 2008.

[56] C. Samuelis, E. Tiesinga, T. Laue, M. Elbs, H. Knöckel, and E. Tiemann. Cold atomic collisions studied by molecular spectroscopy. *Phys. Rev. A*, **63**(1):012710, 2000.

[57] J. Stenger, S. Inouye, M. R. Andrews, H.-J. Miesner, D. M. Stamper-Kurn, and W. Ketterle. Strongly Enhanced Inelastic Collisions in a Bose-Einstein Condensate near Feshbach Resonances. *Phys. Rev. Lett.*, **82**(12):2422–2425, 1999.

[58] Bernhard M. Huber. Towards Realization of a Polaron Experiment. Diploma thesis, University of Heidelberg, 2009.

[59] Jacques Tempere and Wim Casteels. private communication. 2010.

[60] Harold J. Metcalf and Peter van der Straten. Laser Cooling and Trapping. Springer, New York, 1999. ISBN: 0-387-98728-2.

[61] Rudolf Grimm, Matthias Weidemüller, and Yurii B. Ovchinnikov. Optical Dipole Traps for Neutral Atoms. *Advances In Atomic, Molecular, and Optical Physics*, **42**:95 – 170, 2000.

[62] Wolfgang Demtröder. Experimentalphysik 3: Atome, Moleküle und Festkörper. Springer, 2004. ISBN-13: 9783540667902.

[63] Anton Pccardo-Selg. Degenerate Quantum Gases: Towards Bose-Einstein Condensation of Sodium. Diploma thesis, University of Heidelberg, 2008.

[64] Raphael Scelle. Cooling, Plugging, Trapping: Exploiting Optical Dipole Potentials for Polaron Experiments. Diploma thesis, University of Heidelberg, 2009.

[65] Wolfgang Petrich, Michael H. Anderson, Jason R. Ensher, and Eric A. Cornell. Stable, Tightly Confining Magnetic Trap for Evaporative Cooling of Neutral Atoms. *Phys. Rev. Lett.*, **74**(17):3352–3355, 1995.

[66] M.-O. Mewes, M. R. Andrews, N. J. van Druten, D. M. Kurn, D. S. Durfee, and W. Ketterle. Bose-Einstein Condensation in a Tightly Confining dc Magnetic Trap. *Phys. Rev. Lett.*, **77**(3):416–419, 1996.

[67] Z. Hadzibabic, S. Gupta, C. A. Stan, C. H. Schunck, M. W. Zwierlein, K. Dieckmann, and W. Ketterle. Fiftyfold Improvement in the Number of Quantum Degenerate Fermionic Atoms. *Phys. Rev. Lett.*, **91**(16):160401, 2003.

[68] Lev Pitaevskii and Sandro Stringari. Bose-Einstein Condensation. Oxford Science Publications, Oxford, 2003. ISBN: 0-19-850719-4.

[69] Marc Repp. Aufbau einer Vakuumapparatur für Experimente mit ultrakalten fermionischen und bosonischen Quantengasen. Diploma thesis, University of Heidelberg, 2007.

[70] Jan Krieger. Zeeman-Slower und Experimentsteuerung für das NaLi-Experiment. Diploma thesis, University of Heidelberg, 2008.

[71] Stefan Weis. Setup of a Laser System for Ultracold Sodium—Towards a Degenerate Gas of Ultracold Fermions. Diploma thesis, University of Heidelberg, 2007.

[72] E. L. Raab, M. Prentiss, Alex Cable, Steven Chu, and D. E. Pritchard. Trapping of Neutral Sodium Atoms with Radiation Pressure. *Phys. Rev. Lett.*, **59**:2631, 1987.

[73] Wolfgang Ketterle, Kendall B. Davis, Michael A. Joffe, Alex Martin, and David E. Pritchard. High densities of cold atoms in a dark spontaneous-force optical trap. *Phys. Rev. Lett.*, **70**(15):2253–2256, 1993.

[74] K. M. R. van der Stam, A. Kuijk, R. Meppelink, J. M. Vogels, and P. van der Straten. Spin-polarizing cold sodium atoms in a strong magnetic field. *Phys. Rev. A*, **73**(6):063412, 2006.

[75] Valentin V. Volchkov. Cold Lithium Atoms For Future Polaron Experiments. Diploma thesis, University of Heidelberg, 2009.

[76] W. Ketterle and N. J. van Druten. Evaporative cooling of trapped atoms. *Advances in Atomic, Molecular and Optical Physics*, **87**:181–236, 1996.

[77] Thomas Schäfer and Derek Teaney. Nearly perfect fluidity: from cold atomic gases to hot quark gluon plasmas. *Rep. Prog. Phys.*, **72**(12):126001, 2009.

[78] Daniel A. Steck. Sodium D Line Data. University of Oregon, 2009. available online at `http://steck.us/alkalidata/sodiumnumbers.pdf`.

[79] Michael E. Gehm. Properties of ^{6}Li. Duke University, 2003. available online at `http://www.phy.duke.edu/research/photon/qoptics/techdocs/pdf/PropertiesOfLi.pdf`.

[80] Christian H. Schunk. Study of an Ultracold Cloud of Fermionic ^{6}Li Atoms Near a Feshbach Resonance. Diploma thesis, University of Heidelberg, 2002.

[81] Erik van Ooijen. Realization and Illumination of Bose-condensed Sodium Atoms. PHD thesis, Universiteit Utrecht, 2005.

[82] C. V. Nielsen, J. K. Lyngsø, A. Thorseth, M. Galouzis, K. T. Therkildsen, E. D. van Ooijen, and J. W. Thomsen. Characterization of a magnetic trap by polarization dependent Zeeman spectroscopy. *Eur. Phys. J. D*, **48**:111–119, 2008.

Danksagung

An dieser Stelle möchte ich mich bei allen bedanken, die mich während der letzten Jahre unterstützt haben und ohne deren Hilfe dieses Projekt so nicht möglich gewesen wäre. Die Zeit im Labor verging wie im Flug, dank einer hervorragenden Arbeits- und Diskussionsathmosphäre, aber auch dank vieler schöner Poker-, Pizza- und Grillabende. Vielen Dank für diese schöne Zeit!

- Mein besonderer Dank gilt meinem Betreuer Prof. Dr. Markus K. Oberthaler, der mir dieses Projekt zugetragen und meine Begeisterung dafür geweckt hat. Er hatte immer ein offenes Ohr für meine Belange und stand mit stets mit Rat und Tat zur Seite. Seine offene Art und sein unermüdlicher Einsatz für die Gruppe haben entscheidend zum Gelingen dieser Arbeit beigetragen.

- Bei Prof. Dr. Selim Jochim bedanke ich mich für die Begutachtung meiner Arbeit und für seine offene Art die eine gute Zusammenarbeit mit seiner Gruppe erst ermöglicht hat. Wir haben speziell am Anfang beider Projekte sehr voneinander profitieren können und die gemeinsamen Grillabende waren stets ein Erfolg.

- Dem gesamten NaLi Team gilt mein besonderer Dank für die gute Zusammenarbeit, die vielen Diskussionen und die gute Atmosphäre im und außerhalb des Labors. Auch wenn es manchmal Schwierigkeiten zu überwinden gab, so haben wir diese Hürden doch stets genommen und sind erstarkt daraus hervor gegangen. Das bisher Erreichte und die gesammelte Erfahrung, sowohl fachlich als auch zwischenmenschlich, wurde nur durch euch ermöglicht und ich bin sehr dankbar dass ich diesen Weg gemeinsam mit euch gehen durfte. Bleibt nur noch zu sagen: es war mir eine Ehre mit euch anzustoßen und die Grillzange zu teilen!
  - Peter Krüger, Stefan Weis, Marc Repp und Jan Krieger, dem NaLi Team der ersten Stunde danke ich besonders für deren Enthusiasmus mit dem dieses Projekt gestartet wurde.
  - Anton Piccardo-Selg danke ich für die Unterstützung in schwierigen Zeiten. Wir haben zusammen eine sehr ereignisreiche Zeit im Labor erlebt, die ich nicht missen möchte.
  - Valentin Volchkov, Fabienne Haupert und Bernhard Huber gilt mein besonderer Dank für ihren unbeirrbaren Einsatz im Labor und ihren Optimismus.
  - Raphael Scelle, Tobias Schuster und Steven Knoop gilt mein besonderer Dank für die Übersicht mit dem der Wiederaufbau des Experiments nach der wohl schlimmsten Stunde vonstatten ging. Für diese Herausforderung

hätte ich mir kein besseres Team wünschen können. Ich wünsche euch auch mal einen Sonntag auf der Couch, nur unterbrochen durch ein latentes Staubsaugergeräusch.

  - Den neuen NaLi's um Andrea Bergschneider, Mathias Neidig und Arno Trautmann danke ich für die gute Atmosphäre und den Spaß während meiner letzten Zeit im Team.

- Den Mitgliedern des BEC Labors danke ich für die gute Nachbarschaft und besonders dafür, dass sie mir die Schönheit und die Einfachheit der Bloch-Kugel näher gebracht haben.

- Den Mitgliedern des ATTA, Argon, AEgIS und KRb Labors danke ich für die gute Atmosphäre, die Hilfsbereitschaft und den Zusammenhalt innerhalb der Gruppe.

- Jürgen Schölles und Alexander Leonhard gilt mein besonderer Dank für ihre unendliche Geduld und die vielen grauen Haare die ich bei ihnen während der Diskussion über Elektronik und deren Tücken verursacht habe. Ohne ihren Beitrag zum hohen Entwicklungs- und Reparaturaufwand der Elektronik des Experiments wäre diese Arbeit nicht möglich gewesen.

- Den Mitarbeitern der feinmechanischen Werkstatt, insbesondere Siegfried Spiegel, Morris Weißer und Werner Lamade danke ich für die exzellente Unterstützung beim Auf- und Wiederaufbau des Experiments. Der Erfolg der gewickelten Kleeblattspulen sind der beste Beweis für das hohe Niveau ihrer Arbeit.

- Meinen Eltern und Freunden danke ich für die Geduld und die Unterstützung in den letzten Jahren.

- Mein besonderer Dank gilt meiner Lebensgefährtin Donata Danzmann, die mich immer unterstützt hat. Ohne ihren Glauben an meine Fähigkeiten, ihren Optimismus und ihren ordnenden Blick in mein Chaos wäre diese Arbeit nicht entstanden. Du bist mein bester Freund, mein größter Fan und mein härtester Kritiker. Ich liebe dich.